2020 Doctor's degree dissertation

Microscopy study of correlation between residual elastic strain and defects in He^+ ion irradiated 4H-SiC

Subing Yang

Supervisor: Professor Tamaki Shibayama

Graduate School of Engineering,

Hokkaido University, Sapporo, Hokkaido, Japan

July 2020

Table of Contents

List of Publications

1. **Subing Yang**, Zhanbing Yang, Hui Wang, Seiichi Watanabe, Tamaki Shibayam, Effect of laser and/or electron beam irradiation on void swelling in SUS316L austenitic stainless steel, Journal of Nuclear Materials, 488, 215-221 (2017).

2. **S. Yang**, S. Tokunaga, M. Kondo, Y. Nakagawa, T. Shibayama, Non-destructive evaluation of the strain distribution in selected-area He+ ion irradiated 4H-SiC, Appl. Surf. Sci. 500 (2020).

3. **Subing Yang**, Yuki Nakagawa, Minako Kondo, Tamaki Shibayama, Electron energy-loss spectroscopic evaluation of depth-dependent swelling of He+ ion-irradiated 4H-SiC correlated with defect type, J. Appl. Phys. 127, 175106 (2020).

4. YANG Zhan-Bing, **YANG Su-Bing**, QU Xiao-Jian, SHIBAYAMA Tamakic, WATANABE Seiichi, Development of Laser-HVEM and Its Application on In-situ Observation on Lattice Defects Behavior, Chinese J. Struct. Chem. Vol. 39, No. 4 (2020).

List of figures

List of Tables

Abstract

Silicon carbide (SiC) has drawn great attention for electronic and optical applications owing to its excellent mechanical, optical and electronic properties, which has also been proposed as structure and cladding materials in nuclear or aerospace environment. However, for its extensive applications, there are still lots of problems to overcome, especially for the irradiation-induced strain in SiC. An accurate non-destructive evaluation of the residual strain in SiC devices has become increasingly important, in particular with the development of the advanced micro/nano SiC-based devices. Besides, clarifying the contribution to the strain/swelling of each defect type is important to accurately evaluate the strain or swelling. In this study, selected-area He^+ ion irradiation was performed on n-type 4H-SiC (0001) single-crystal substrates with an energy of 100 keV at room temperature. The irradiation-induced swelling/strain and defects were investigated in the He^+ ion irradiated 4H-SiC using various characterization techniques, including confocal Raman microscopy (CRM), electron backscattered diffraction (EBSD) and transmission electron microscopy (TEM).

A detailed normal strain distribution in the ion-irradiated 4H-SiC was first provided using the non-destructive techniques of EBSD and CRM, whose results showed good agreement. This result validated the application of EBSD and CRM to evaluate the detailed strain distribution in selected-area ion-implanted SiC. In addition to the strain introduced in the irradiated area, excessive strain also extended into the surrounding substrate owing to irradiation-induced swelling. Furthermore, a higher compressive strain is concentrated around the interface between the irradiated and unirradiated areas. An anisotropic strain distribution in the irradiated area is also detected using EBSD, which indicates a correlation of strain degree and crystallographic orientation.

Using TEM techniques, a great anisotropy of defect distribution was first deduced in the selected-area He^+ ion irradiated 4H-SiC, that interstitial type defects preferentially redistribute into the surface normal direction ([0004] direction) with more negative volume defects locating in the lateral direction ($[10\bar{1}0]$ and $[11\bar{2}0]$ direction), which might account for the detected anisotropic strain using EBSD. This anisotropy decreased upon annealing at 600 °C, and it was quite lower in the non-selected-area He^+ ion irradiated 4H-SiC. It was found that great compressive stress was introduced in the lateral direction in the selected-area He^+ ion irradiated 4H-SiC due to the constraint against lateral expansion, and these compressive stresses were introduced at the beginning of ion irradiation. These findings provided a direct evidence that compressive stress was supposed to inhibit the interstitial type defect formation, enhancing the anisotropic defect distribution.

Using TEM and scanning transmission electron microscopy electron energy-loss spectroscopy (STEM-EELS), the correlation of the swelling with various defects, including point defects or tiny clusters, defect clusters, amorphous transition and helium atoms, was separately analyzed. These results provided the volume swelling range for the different defect regions, which is helpful for the prediction of SiC swelling in actual application. Helium atoms in the form of helium bubbles increase the volume swelling at relatively high irradiation fluences. However, decreasing effect of He^+ ion irradiation on volume swelling also seems to be possible as below a certain irradiation fluence.

Chapter 1 Introduction

1.1 Background

Nowadays, shortage of energy has become one of the main challenges, which human will face in the years to satisfy the ever-increasing energy demand, due to limited non-renewable fuel resources and an increased awareness regarding climate change. Although some renewable or environmentally friendly energy generation solutions such as wind and photovoltaic, are hurry developing, it is still hard to meet the energy demand for the increased urbanization and electrification. It is foreseen that more electrical systems will continue and accelerate over the next years. Especially, more attention has been given to development in power electronics which will eventually result in a much more efficient generation as well as management of electrical energy. Currently, the power semiconductor industry is majorly served by silicon (Si) semiconductor materials. Even though state-of-the-art Si device technologies are always improving, the material itself possess performance limitations due to its intrinsic physical properties, making it hard to meet trend towards higher voltage, higher current, and higher switching frequency. Silicon carbide (SiC) is a promising wide bandgap semiconductor material with high breakdown electric field strength, high saturated drift velocity of electrons and a high thermal conductivity as compared to many other semiconductors, such as Si and GaAs. Hence, SiC has been proposed to use in high power, high frequency and high temperature applications[1,2], and has been actually used to

fabricate SiC-based devices, such as SiC power metal-oxide-semiconductor field-effect transistor (SiC power MOSFETs) as shown in Fig. 1.1.

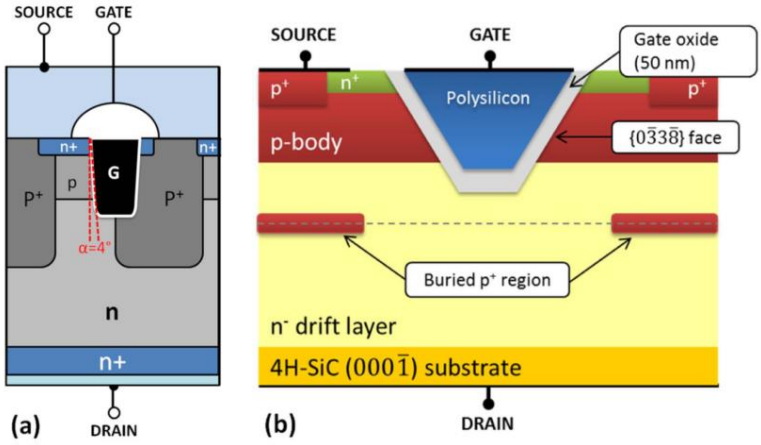

Fig.1.1. Sketch of novel trench/groove MOSFET (a) the CoolSiC™ Trench MOSFET cell [3] and (b) the V-groove MOSFET from Sumitomo [4].

Besides, to overcome the energy shortage, more efficient and reliable energy generation solutions are also required. Renewable energy sources together with future fusion and Generation IV fission nuclear power plants are potential candidates [5,6]. However, the components applied in reactor are in the most extreme environment as they are exposed to various high energy particle irradiation, severe mechanical loadings and/or corrosive environments. For instance, neutron exposure displaces numerous atoms from their lattice sites inducing material degradation. This requires that materials used in irradiation environment should maintain not only good mechanical properties but also good irradiation tolerance. Due to its unique mechanical and physico-chemical properties, including high strength, high thermal conductivity and relatively good corrosion resistance, SiC and SiC-

based composites are considered as structure or cladding materials in future nuclear or aerospace environment [7-10]. Hence, SiC is a promising material both for electronic devices fabrication and structure application in nuclear environment. However, for its extensive applications, there are still lots of problems to overcome, especially for the irradiation-induced defects, strain and swelling in SiC.

1.2 SiC crystal structure

Silicon carbide is a compound of silicon and carbon, which have an easy chemical formula SiC, which has been widely used both as a semiconductor materials or structural materials. Up to now, over 250 crystalline forms has been reported for SiC [5], depending on their crystal lattices and stacking sequences along the c-axis, such as, rhombohedral types (15R-, 21R-, 27R- etc.), hexagonal types (2H-, 4H-, 6H- etc.) and the single cubic-type (3C-) [11]. The fundamental structural unit in all SiC crystal is a covalently bonded primary co-ordination tetrahedron (either SiC4 or CSi4). A carbon atom is at the centroid of four silicon atoms (or vice versa). One of the four Si–C bonds is parallel to, and taken to coincide with, the c-axis of the crystal.

Among the more than 250 crystal type of SiC, the most common types are 3C, 4H, 6H and 15R, where the leading number shows the repetition of the Si–C pair with C, H and R representing cubic, hexagonal and rhombohedral crystals, respectively [12]. The crystal structures of 3C-, 4H-, 6H- and 15R-SiC are schematically illustrated in Fig. 1.2 [13]. The 3C-SiC crystal, known as β-SiC, has the only sequence out of the infinite number of variations that

shows cubic symmetry. All the other polytypes, which show non-cubic symmetry, are classified as α-SiC [14].

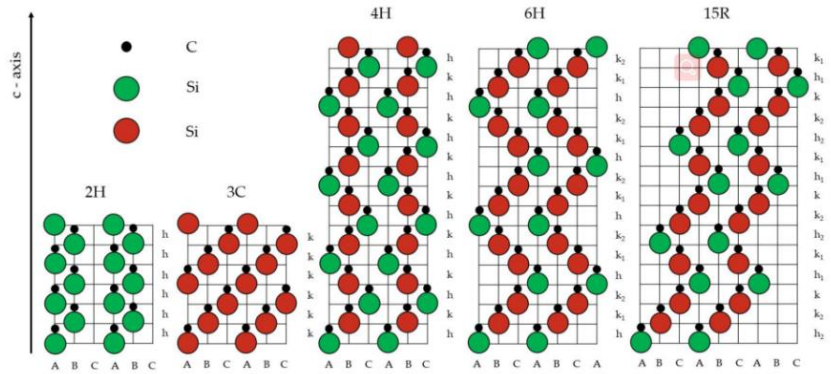

Fig. 1.2. Diagram of the primitive cells of important polytypes of silicon carbide [15].

1.3 Properties of SiC

1.3.1 Electrical properties

Functionally, SiC is an indirect wide bandgap semiconductor material. As compared to the transition metal carbides, the covalent carbides are generally considered electrical insulators since they have no metallic bonding and their electrons are strongly bonded to the nucleus. However, the SiC exhibits semiconductor properties through ion-implantation doping, depending primarily on the concentration and type of the doping element. For example, p- and n-type semiconductor properties would be acquired as doping the aluminum and nitrogen elements, respectively.

The bandgap of SiC is approximately three times that of Si with its bandgap varying from 2.36 to 3.26 eV depend on the polytype, as shown in Table 1.1. The wide bandgap means that electron is not easily thermally excited from the valence band to the conduction band. Besides, SiC has a very low intrinsic carrier concentration through the doping of impurities at

higher temperature. Its larger bandgap and low intrinsic carrier concentration make it an appropriate material for high temperature devices, including the devices operating in harsh environment (such as automotive and aerospace application) as well as high power devices that generate large amount of heat. SiC can withstand thermal temperature about 1000 °C, however, Si might deteriorate at about 250 °C. At the same time, SiC has a very high dielectric breakdown field strength that is ten times that of Si. Hence, compared to the conventional semiconductor materials such as Ge, Si and GaAs, SiC is great suitable for operating at high-voltage, frequency and temperature [2].

Table 1.1. Properties of common SiC polytypes and conventional semiconductors [16].

	E_g (eV)	n_i (cm^{-3})	E_b ($MVcm^{-1}$)	μ_e ($cm^2V^{-1}s^{-1}$)	v_s (cms^{-1})	κ ($Wcm^{-1}K^{-1}$)
6H-SiC	3.26	10^{-7}	2.0-3.0	720	2×10^7	3-5
4H-SiC	3.02	10^{-5}	2.5	370	2×10^7	3-5
3C-SiC	2.36	10	>1.5	900	2×10^7	3-5
Si	1.12	10^{10}	0.6	1350	2×10^7	1.5
GaAs	1.42	2×10^6	0.6	8500	2×10^7	0.5
GaN	3.40	10^{-10}	2-3	1000	2.5×10^7	1.3

Note: Energy bandgap, E_g; intrinsic carrier concentration, n_i; breakdown voltage, E_b; electronic mobility, μ_e; saturation electron velocity, v_s; and thermal conductivity, κ.

1.3.2 Thermal conductivity

SiC owns a good thermal conductivity, which makes SiC-based devices quite suitable for application at high temperature. For the structure

component applied in nuclear reactor, such as the flow-channel-insert wall in nuclear fusion reactor, different thermal expansion might be induced by the through-thickness temperature gradient [17], which would introduce a significant internal shear stress in the structure and limit the operation temperature of the nuclear reactors. Hence, the good thermal conductivity also makes SiC a promising structure material used in reactor.

Various studies have been performed to investigate the thermal conductivity of SiC over a wide range of temperature [18]. At temperatures below 200K, the thermal conductivity of SiC exhibits a rapidly increases with increasing temperature because of the large variation of the specific heat (*Cp*) [9]. Beyond the peak at 200 K, the its thermal conductivity sharply decreases with increasing temperature owing primarily to the phonon-phonon scattering [9]. Besides, the thermal conductivity of SiC also correlated with grain size and the nature of grain boundary [19]. Below 300 K, the thermal conductivity monotonically increases with increasing its grain size, and the correlation between thermal conductivity and grain size becomes decreasing important with increasing temperature. It is reported that the impurities and/or micro pores preferentially reside at grain boundaries. The presence of these defects at the grain boundaries as well as the grain boundaries themselves, lead to a significant reduction of thermal conductivity [20]. It has been reported that the single crystal form of SiC, as compared to the other varietals, owns the highest thermal conductivity. However, high-purity and dense polycrystalline CVD SiC exhibits practically the same conductivity as single-crystal SiC in the orientation of

its crystal growth axis.

1.3.3 Thermal expansion

In term of the shear stress induced by the differential expansion due to the through-thickness temperature gradient, the thermal expansion properties of SiC is also an important aspect that should be considered for application in nuclear reactor. The interatomic spacing between the atoms of the SiC is a function of temperature. At 0K, these atoms have their lowest energy position, i.e., they are in the ground state. The increased stored energy resulting from increasing temperature causes the atoms to vibrate and move further apart. In short, the mean interatomic spacing increases, resulting in thermal expansion. In strongly bonded solids such as the SiC, the amplitude of the vibrations is small, and the dimensional changes remain small [9]. This is one of the advantages that SiC as a candidate structure material in reactor. Beside the temperature, the thermal expansivity of SiC is also correlated with its crystal structure. For instance, the hexagonal SiC crystal shows an anisotropic thermal expansion between a- and c- axis [21].

1.3.4 Mechanical properties of SiC

1.3.4.1. Hardness

As a covalent material, SiC possess high hardness, which has been confirmed by various studies and various techniques [22]. Hardness is a complex property which involves both elastic and plastic deformation, crack initiation and propagation, and the development of new surfaces. Generally, hardness is dependent on the fabrication process, composition, and the presence of impurities. Moreover, it can be defined in terms of bonding

energy, covalence level, atomic spacing and by the parameters of fracture and deformation. It is reported that the hardness of SiC significantly depends on the crystal structure. For example, single-crystal α-SiC exhibits an anisotropic hardness due to the presence of its preferred slip system [23], which suggests that the hardness of SiC should be different for different polytype.

1.3.4.2. Elastic constants

Generally, a dense and high-purity SiC material, e.g., CVD SiC, exhibits the highest elastic modulus, however, its elastic modulus decreases with increasing porosity or impurity concentration. In contrast, neither grain size nor polytype was recognized as having a significant effect on the elastic modulus of SiC [7-9]. In addition, the elastic modulus of SiC shows a slight decrease at elevated temperatures [24]. The elastic moduli for α- and β-polycrystalline SiC is reported to be similar. However, Elastic tensors of popular single-crystals SiC (3C-, 4H- and 6H-SiC) are varied. The elastic tensor data of C11=511, C12=128 and C44=191 GPa are now recommended for 3C-SiC [9].

1.3.4.3 Fracture toughness

The fracture toughness of SiC has also been widely studied using various techniques, such as micro- and nano-indentation [25], surface crack in flexure (SCF) [26], and double torsion (DT) [27]. As considering the scattering, the mean fracture toughness measured by above techniques is similar around 3 MPa $m^{0.5}$.

The fracture toughness is found to be correlated with the grain size and

peaked at a grain size of about 1-5 μm, which is same as the fracture energy. A likely mechanism was reported that the microcrack formation may be attributed to the combined effects of the local micro-stresses and the applied stress, and this internal residual stress may be induced during SiC fabrication [28]. Besides, the fracture toughness of SiC remains nearly constant with temperature for sintered and reaction-bonded SiC materials, while it increases at elevated temperatures for CVD SiC.

1.4 Irradiation effect on SiC

Although SiC obtains excellent properties mentioned above, irradiation or implantation would lead to deterioration of some or all of the above properties. This is due to the various damage or defects introduced during irradiation.

1.4.1 Defect type

Before describing the irradiation-induced defects in SiC, it is necessary to recall the process that produce the displacement of the target lattice atoms. As an energetic incident particle elastically interacts with a lattice atom, there will be a kinetic energy exchange between them. If this transmitted energy exceeds the threshold displacement energy of the knocked lattice atom, E_d, it will be ejected from its equilibrium site resulting in a Frenkel pair formation: a vacancy and an interstitial atom. Also, if the kinetic energy transfer is high enough, the displaced atom may have enough kinetic energy to displace not only one but many atoms of the lattice, which, in turn, will cause other displacement processes, as shown in Fig. 1.3. Displacement

cascades depend on the energy given to the primary knock-on atom (PKA) by the incident particle [29], and the displacement cascade process will continue until the kinetic energies of the displaced atoms are below the E_d. As a result of the displacement cascade, a wide variety of stable lattice defects, ranging from isolated Frenkel pairs to large defect clusters, could form with diffusion and combination of the displaced lattice atoms.

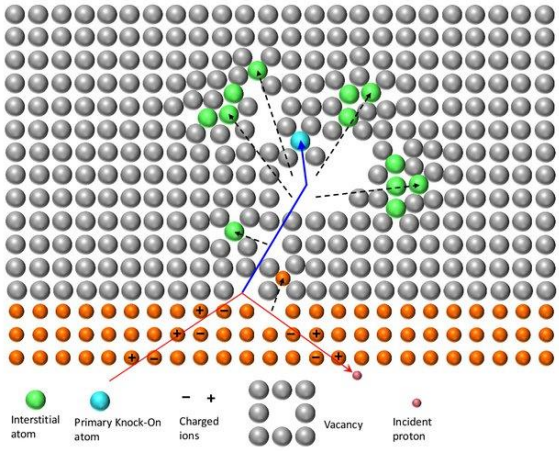

Fig. 1.3. Two-dimensional illustrations of different types of point defects generated by a displacement cascade due to protons incident on a crystal. These defects include point vacancies, interstitial atoms and their clusters [30].

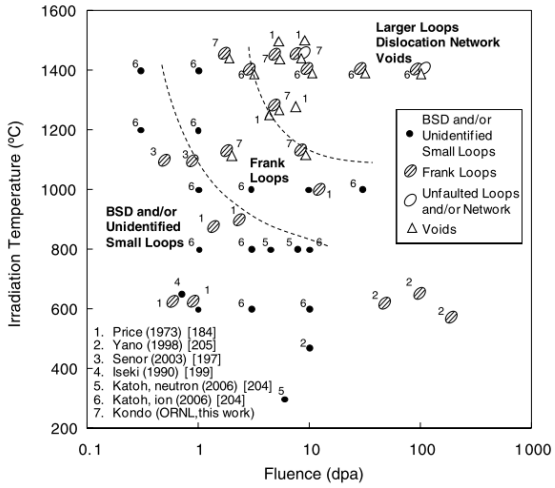

Fig. 1.4. Summary of the microstructural development in cubic SiC during neutron and

self-ion irradiation [31].

The stable defects formed in SiC depend on the irradiation fluence or does (displacement per atom, dpa) and temperature. The irradiation-induced various defects have been reviewed by Katoh et al. as shown in Fig. 1.4 [31]. Beside the isolated stable point defects, such as vacancy and interstitial atom, below several hundred Kelvin, the observable defects in irradiated SiC is called as black spots defects (BSDs), which are most likely tiny clusters of self-interstitial atoms in various indeterminate configurations [32]. With the temperature increase, the mobility of interstitial defects is enhanced that more interstitial defects may combine together and form small loops. At higher temperatures such as 1173–1673 K [33, 34], interstitial type Frank faulted loops would become the dominant defects observed by transmission electron microscopy. At temperatures where vacancies are sufficiently mobile, vacancy clusters can be formed. Three dimensional cavities (or voids) are the only vacancy clusters known to commonly develop in irradiated SiC. The lowest temperature at which void formation was previously reported is 1273K and 1523 K for silicon ion irradiation and neutron irradiation [9], respectively. Besides, the void dominates the swelling at irradiation conditions of 1673 K and >10 dpa [35]. Positron annihilation and electron paramagnetic resonance studies have shown that the silicon vacancy in cubic SiC becomes mobile at 1073–1173 K [36].

1.4.2 Amorphization of SiC

For irradiation temperatures lower than a critical temperature, the crystal

of SiC would become amorphous, if the accumulation of strain due to the irradiation-produced defects exceeds a critical level. This has been shown for both under self-ion irradiation and fast neutron irradiation [37, 38]. The critical temperature was widely reported, which ranged about 423-498 K [39]. The irradiation does, above which the crystal will reach amorphous, increases with the irradiation temperature.

Amorphization often gives rise to significant volume changes and concomitant microcracking, leading to a great change of properties of SiC. For instance, the swelling of neutron- and ion-amorphized SiC has been reported to be 10.8% for 343K irradiation [40]. Besides, amorphous semiconductor alloys are of technological importance for electronic and optoelectronic device applications. In particular, amorphous silicon carbide (a-SiC) has attracted great attention because of its outstanding physical properties.

1.4.3 Irradiation-induced swelling

These defects or damage introduced during irradiation will induce great strain and swelling in the materials, which largely degrades the properties of SiC. As mentioned above, irradiation-induced damage or defect depends on the irradiation temperature and/or dose. Hence, the swelling is also correlated with the temperature and dose.

The neutron-induced swelling of SiC has been well studied for low and intermediate temperatures (293–1273K) [41]. It is well known that swelling mainly depended on the type of irradiation-induced defects or damage, that is, different type defect will result in different value of swelling. In the

temperature range where SiC is applied, the main type of defect or damage includes point defects, BSDs, defects loop, void and amorphization [42, 43]. For temperatures below the critical amorphization temperature (423K), the volume of crystalline SiC increases with damage accumulation up to amorphization [9]. At higher temperature, the swelling increases logarithmically with dose until it approaches saturation, with a steady decrease in the saturation swelling level with increasing irradiation temperature. The dose exponents of swelling during the logarithmical period are in many cases close to 2/3, as predicted by a kinetic model assuming planar geometry for interstitial clusters [44]. This temperature regime is generally referred to as the point-defect swelling regime and can be roughly set between 423 and 1273 K [9]. At temperature higher than 1273 K, the swelling may major result from the voids.

Many studies have been dedicated to understanding irradiation-induced defects and their contributions to swelling and creep. However, the contribution of the defects themselves to the swelling in SiC is less understood. For instance, transmission electron microscopy (TEM) is useful to measure the distribution of defect clusters in irradiated SiC [43]. However, only 10 - 45% of the macroscopically measured swelling was accounted for by the clusters and loops that were visible in TEM. For the amorphization, the magnitude of swelling reported so far is highly scattered from 8 to 20% [38]. It is reported that, this scattering volume swelling may be attributed to the different amount of Si-Si and C-C bonds depending on the irradiation temperature. Further investigations are still needed to clarify the contribution

of different type defect to swelling in SiC.

1.5 Strain measurement methods

Now, there are many methods to measure the lattice strain or swelling in crystalline materials, such as the X-ray diffraction, transmission electron microscopy (TEM) and atomic force microscope (AFM). These methods have their own advantages and disadvantages in strain measurement.

1.5.1 XRD

Various studies have used XRD to measure the strain or swelling in the materials induced by different reasons [42, 45, 46]. Based on diffraction theory, the lattice spacing, d, for a certain lattice plane can be precisely determined from the corresponding diffraction angle, θ, using the Bragg equation:

$$n\lambda = 2d\sin\theta \tag{1-1}$$

When strain, usually caused by defects, thermal treatment or mechanical processing, exist in materials, the lattice spacing, d, will change from d_0 to $d_0 + \Delta d$. Under the condition of a continuous monochromatic X-ray beam of constant wavelength, the change in the lattice spacing will result in the diffraction angle, θ, changing from θ_0 to $\theta_0 + \Delta\theta$. From the above equations, the strain, ε, along the direction perpendicular to the lattice plane can be calculated using the diffraction angle.

The XRD analyses method is very sensitive to the lattice strain that it can provide a relative high strain resolution with a space resolution of a few microns [46-48]. So, XRD method is quite appropriate to measure a

homogeneous strain in the materials, such as the materials irradiated by neutron. However, XRD is hard to provide an accurate strain distribution in the ion irradiated materials in which the damage varies in depth. To overcome this limitation, researchers invented a web-based program GID_SL [49] to provide a strain profiles as a function of depth by manually fitting from the experimental varying interference fringe period. However, XRD is still hard to measure the local strain distribution in some small devices, such as the advanced micro/nano SIC-based devices, due to its limitation in spatial resolution. In addition, based on the diffraction theory, XRD method might be not suitable to measure the strain in the heavy damaged even amorphous SiC.

1.5.2 Raman microscopy

Raman scattering has been widely used for characterization of semiconductors materials [46]. Using the confocal Raman microscopy (CRM) technique, Raman scattering has also been proposed as a method to measure the residual strain in Si and SiC [50].

The Raman scattering is an inelastic scattering phenomenon of photons by phonons or electrons in materials. The unit of 3C-SiC contains one formula unit and there are a longitudinal optical (LO) mode and a doubly degenerate transversal optical (TO) mode in optical branches. The phonon bands Raman scattering in crystals shift with stress, because the atomic distance, in other words, the bonding forces are changed by the stress. The behavior of the Raman bands in the 3C-SiC under hydrostatic pressure has been studied by Olego et al. [51]. The frequencies of the TO and LO modes against the

relative lattice compression are given (in unit of cm^{-1}) by

$$\omega(\mathrm{TO}) = 796.5 + 3734(-\Delta a/a_0) \quad (1\text{-}2)$$

$$\omega(\mathrm{LO}) = 973 + 4532(-\Delta a/a_0) \quad (1\text{-}3)$$

Where a_0 is the lattice constant.

Amounts of studies tried to evaluate the strain or stress using these equations and have got reasonable results [50]. For an accurate and quantitative determination of biaxial strain as in the case of strained epitaxial layers, however, the hydrostatic pressure coefficients cannot be used because they lead to serious errors. By comparing the results of two micromachined 3C-SiC membranes with different mechanical properties, a more consistent relationship between biaxial in-plane strain and Raman line shift was reported by S. Rohmfeld [52] as follows, which were demonstrated to agree well with experimental results.

$$\omega(\mathrm{TO}) = (795.9 \pm 0.1) - (1125 \pm 20) \cdot (\Delta \mathrm{a}/a_0) \quad (1\text{-}4)$$

$$\omega(\mathrm{LO}) = (974.1 \pm 0.1) - (1585 \pm 32) \cdot (\Delta \mathrm{a}/a_0) \quad (1\text{-}5)$$

1.5.3 Electron backscattered diffraction

As mentioned above, the residual stress states around these deformation zones can be studied by X-ray diffraction or Raman spectroscopy in the scale of micron meters. Recently, electron backscattered diffraction (EBSD) has drawn considerable attention as a non-destructive technique for measuring the residual strain on the surface of crystalline materials with a higher spatial resolution [50, 53, 54]. Using cross-correlation analysis of the EBSD pattern, strain sensitivity on the level of about 10^{-4} has also been obtained [55].

The crystal lattice would be distorted by elastic strains. If this strain is

uniaxial and along one of the principal directions of the unit cell, then the strain produces a change in one of the cell parameters as shown schematically in Fig. 1.5 [54]. This distortion manifests itself in the patterns as a shift in some of the zone axes along with changes in the width of some of the diffraction bands. If there is elastic strain in the sample crystal, the features in the EBSD patterns would change, and this change depends on the variations of elastic strain and small lattice rotations. which can be used to correlate the EBSD pattern shift with the size and nature of the strain [54,56]. Within each grain, once the reference pattern is set, strain in the EBSD scanned area can be determined.

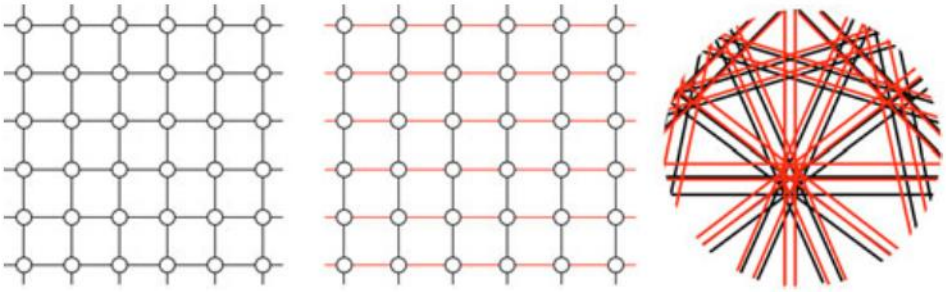

Fig. 1.5. A crystal lattice “strained” 11% uniaxially in the horizontal direction and a schematic overlay of the patterns with (red) and without strain (black) [54].

Absolute strains can be obtained only in situations where the strain in reference pattern is known. When the reference pattern comes from a region with unknown strain, the map shows only the relative variation in strain from the unknown reference state. However, we can still obtain important information such as lattice curvatures and elastic strain gradients. With the larger datasets that are now studied methods for automatically selecting the

reference points have been developed [57].

Absolutely, high resolution EBSD provides a useful bridge between X-ray or neutron techniques and much localized transmission electron microscope (TEM). The main strengths of this technique are (i) that all components of the 3D strain and rotation tensors are obtained in parallel, (ii) the use of an electron beam allows very small volumes of material to be probed, and (iii) the equipment required is rather widely available. A disadvantage is that the depth probing capabilities of X-ray, in particular synchrotron methods, are clearly not available.

1.5.4 Some other methods

There are also some other possible methods that can be used to measure the strain or swelling, such as atomic force microscopy (AFM), neutron diffraction and some TEM methods.

The AFM usually measures the swelling by comparing the dimensional change before and after ion irradiation [58], and it also have a relatively high spatial resolution to a ~nm level. Besides, AFM is also useful to determine the surface profiles. Like XRD, neutron diffraction also obeys the Bragg equation. The penetration depth of neutrons in materials is on the order of ~cm [28], which makes neutron diffraction a powerful probe for characterizing the strain in bulk materials. Currently, the neutron diffraction method is widely applied to rails, steels and alloys to analyze the distribution of residual stresses and evaluate their service life. The TEM methods, including HR-TEM, HR-STEM and EELS, are powerful to measure the local strain [59, 60], which is helpful to clarify the effect of a special defect to the

local stain or swelling.

1.6 Motivation and objectives

As introduced above, SiC owns excellent mechanical and electronic properties. However, no matter as a semiconductor or as structure material in nuclear and aerospace environment, SiC would suffer from high energy particles irradiation. For instance, ion implantation will be performed to introduce carriers into SiC material for these SiC-based electronic device fabrication [2]. These irradiations or implantations would inevitably introduce various damage in SiC material, degrading its mechanical properties and changing its electronic properties [45, 61, 62]. A fundamental understanding of irradiation effects in SiC is required to effectively utilize ion-implantation techniques in device fabrication and to predict its performance in nuclear environments.

Among the irradiation-induced degradation, one of the most concerned damages is the dimensional instability, including radiation swelling [32, 37], which would induce great strain and stress. SiC is brittle, therefore, SiC-based components might be cracked or failure by fracture due to the strain or stress developed in the material. For example, radiation-induced swelling in SiC can be as high as 10% [42], which is significantly higher than the cracking strain of 0.1% in SiC. Hence, it is necessary to evaluate the irradiation-induced strain or swelling in SiC for actual application. Especially with the development of advanced micro/nano SiC-based electronic devices, an accurate and non-destructive evaluation measurement

technique has become increasingly important to stabilize the properties of SiC-based devices. However, the common strain measurement techniques like X-ray diffraction (XRD) seem not qualified for this work due to their limitation in spatial resolution, and an appropriate non-destructive technique with a high spatial and strain resolution should be proposed. Besides, a fundamental understanding of the mechanism for the irradiation-induced strain or swelling is need. Although considerable investigations have been performed to explore the irradiation-induced swelling and have confirmed that swelling is driven by formation of defects or damage under irradiation, existing investigation results are limited by the lack of understanding of specific defect contribution to swelling. For example, defects that can be detected with traditional transmission electron microscopy (TEM) techniques account only for 10-45% of the swelling measured in irradiated SiC [43]. Knowledge of the stable defect structures and their contribution to swelling is essential for accurately predict the swelling in actual application.

To overcome the problems mentioned above, this research is trying to explore an appropriate non-destructive strain measurement technique that can be used to accurately evaluate the strain in ion-irradiated SiC. Also, I am intended to clarify the effect of irradiation-induced defects on the strain/swelling accumulation in SiC, including defect type and defect distribution. After an integrated experimental investigation, two promising strain measurement methods were validated that can evaluate the strain or swelling distribution in SiC with a relatively high spatial resolution. Besides, I also clarify the contribution of different type defects to radiation swelling.

This research is important to predict the strain/swelling of SiC during irradiation, which would be helpful to estimate the lifetime of SiC component in nuclear environment or the implantation fluence for processing the SiC devices.

1.7 Brief introduction of the achievement in master period

In master period, I performed the investigation of irradiation effects on austenitic stainless steel using multi-quantum beam high voltage electron microscope (multi-quantum beam HVEM), and the results has been published in the Journal of nuclear materials. Here, the results were shortly introduced.

Effect of Laser and/or Electron Beam Irradiation on Void Swelling in SUS316L Austenitic Stainless Steel

1. Introduction

The application of austenitic stainless steels is still limited by large amounts of void swelling still in nuclear reactors [1-7]. Up to now, significant effort has been performed to inhibiting or reducing irradiation-induced void swelling, and some methods have been investigated in recent decades to increase the swelling resistance by designing self-healing microstructures, such as doping with trace elements [8,9], cold working [10,11] and the precipitation of dispersed phases [3, 12, 13]. However, these promising methods is still undeveloped in some ways [14-23]. Therefore, it is important to keep investigating the austenitic stainless steels and find new ways to inhibit void swelling in these alloys.

Compared with the methods mentioned above, which reduce void swelling by increasing the void resistance of austenitic stainless steels before

irradiation. We proposed a new method, i.e. simultaneous laser-electron dual-beam irradiation, that could directly inhibit void swelling during irradiation and requires no change to the properties of the austenitic stainless steels before irradiation [24]. This method is convenient and provides a new sight to the inhibition of void swelling. In my master period, the effect of temperature on void swelling for laser-electron dual-beam irradiation and the underlying mechanism were mainly investigated.

2. Experimental procedures

Commercial SUS316L austenitic stainless steel was used in this study, and its chemical composition was listed in Table 1. After mechanical polishing to 0.15 mm thick, disk specimens were punched from sheets with a size of 3 mm in diameter. Foil samples for transmission electron microscopy were prepared by twin jet electropolishing.

Table 1 Chemical composition of SUS316L steel (mass%) [25]

C	Cr	Ni	P	S	Mn	Si	Mo	V	Al	N	Fe
0.013	17.24	13.32	0.024	0.0010	1.28	0.20	2.04	0.04	0.014	0.0396	Bal.

To identify the effect of laser and/or electron beam irradiation on void swelling, the results under laser-electron dual-beam irradiation and sequential laser-electron irradiation were compared with the results got from electron beam irradiation, which is treated as a standard in this study because of the thorough investigation of void swelling behavior under electron-beam irradiation. Therefore, three series of irradiation (electron irradiation (e^- irr.),

sequential laser-electron irradiation (L→e^- irr.) and laser-electron dual-beam irradiation (L+e^- irr.)) were performed with multi-quantum beam HVEM (Laser: Nd:YAG (Continuum, Inlite II-20); HVEM: JEOL, JEM-ARM1300) at temperatures from 573 K to 773 K at 50 K intervals. During electron beam irradiation, the voltage was at 1250 kV, and the mean damage rate was 2×10^{-3} dap/s with a dose of 3.6 dpa for 30 min. For pulsed laser beam irradiation, the laser parameters were 532 nm, 2 Hz and 24 mJ/cm^2 for the central wavelength, repetition rate and energy density, respectively. The details for the three irradiation procedures are shown in Table 2.

Table 2 Details of three types of irradiation [25]

Types	Temperatures (K)	Procedures
e^- irr.	573-773	Single electron beam irradiation for 30 min
L→e^- irr.	573-773	Single laser beam irradiation for 30 min followed by electron irradiation for 30 min.
L+e^- irr.	573-773	Simultaneous laser-electron dual-beam irradiation for 30 min

Void microstructure observation was conducted using transmission electron microscope (Tecnai G^2 F20). The measured thickness at the irradiated area was about 300 nm. For each irradiation condition, void swelling parameter, including the void size, number density and swelling, were counted and calculated in five fields.

3. Results

The void microstructures in austenitic stainless steels under different

irradiation conditions are displayed in Fig. 1. It is clear that the voids formed at different temperatures or under different irradiation styles show great differences in size and number density.

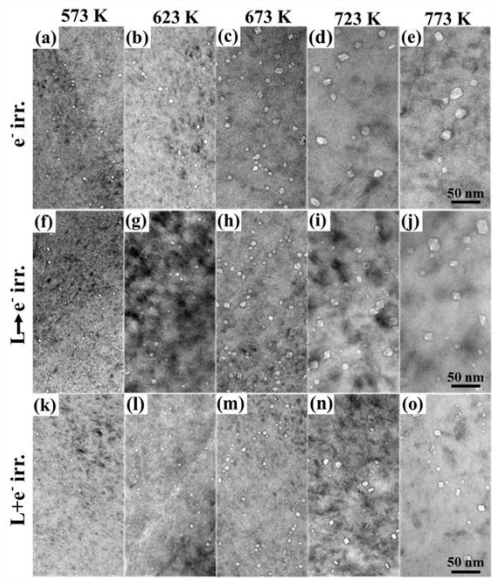

Figure 1 Void microstructures under different irradiation conditions. (a-e) e^- irr.; (f-j) L→e^- irr.; (k-o) L+e^- irr [25].

The dependence of temperature on void number density, mean size and swelling with the three irradiation series are shown in Fig. 2(a), (b) and (c), respectively. With the irradiation temperature increasing, the void number density first increases followed by a marked decrease after reaching a maximum at 673 K. The maximum values are about 13.4×10^{20} m^{-3}, 15.8×10^{20} m^{-3}, and 18.6×10^{20} m^{-3} for e^- irr., L+e^- irr. and L→e^- irr., respectively. Furthermore, in this temperature range, the void number densities under e^- irr. are lower than under both L→e^- irr. and L+e^- irr., which agrees well with our previous work at 723 K [24].

In Fig. 2(b), the mean sizes of void under e^- irr., L+e^- irr. and L→e^- irr.

increase with increasing irradiation temperature, from 3.7 nm, 3.2 nm and 2.8 nm at 573 K to 14.5 nm, 12.1 nm and 8.6 nm at 773 K, respectively. Although the temperature dependence of void under L→e^- irr. and L+e^- irr. is similar to that under e^- irr., there are still some significant differences in their values. It is clear that the void sizes under L→e^- irr. and L+e^- irr. are notably smaller than that under e^- irr.

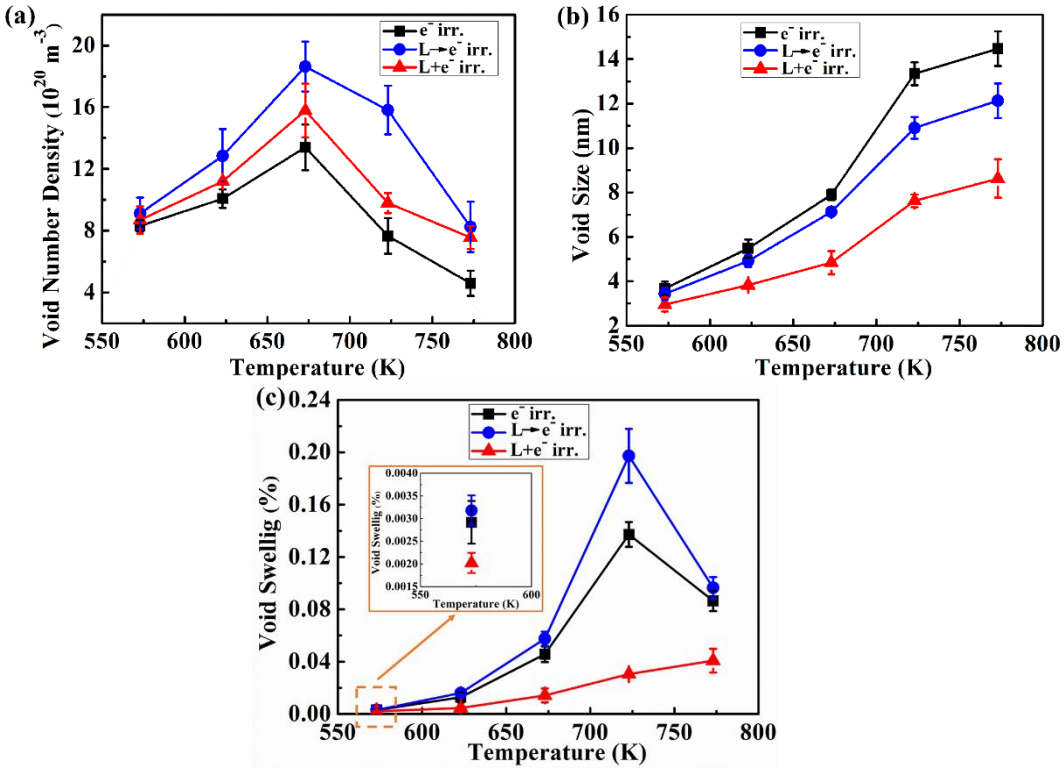

Figure 2 Temperature dependence of void swelling under three irradiation series (a) Void number density. (b) Void size. (c) Void swelling. The error bar indicates the standard deviation [25].

The void swelling, corresponding to the comprehensive results for void mean size and number density, are displayed in Fig. 2(c). For the temperature dependence of void swelling, e^- irr. and L→e^- irr. show a similar curve, with

a peak swelling, 0.137% for e^- irr. and 0.197% for L→e^- irr. at 723 K. Although the void swelling under L+e^- irr. continues increasing from 573 K to 773 K, its value is quite small, only 0.041% at 773 K. Furthermore, when the swelling was compared at the same temperature for these three irradiation series, the tendency in the temperature range of 573-773 K is always L+e^- irr. < e^- irr. < L→e^- irr.. This result demonstrates the suppressing effect of L+e^- irr. over the entire temperature range of 573-773 K.

4. Discussion

4.1 Void number density under three irradiation series

The void formation, in term of the void nucleation and growth, is driven by irradiation-induced point defects [26]. For void nucleation, a definite critical vacancy concentration is necessary to reach, which is depended on the temperature [27]. It should be pointed out that at 573 K, due to low diffusivity of vacancy, void formed at this temperature is quite small under each irradiation, resulting in the small number of visible voids. This may account for the relatively small difference of void number density under each irradiation, as shown in Fig. 2(a). Below 673 K, the void nucleation is obviously enhanced with the increasing temperature, which should be attributed to the increasing mobility of vacancy. However, void number densities show a sharp decreasing as the irradiation temperature higher than 673 K, which may be correlated with the decrease of supersaturated vacancy concentration as the result of preferential vacancies flow towards point defect sinks, such as dislocation and grain boundary [17,28].

4.2 Void growth under three irradiation series

The void growth is determined by the net rate of vacancies flowing into the void [29]. With temperature increasing, an expedited void growth rate was observed as shown in Fig. 2(b), resulting from the increase of the vacancy diffusivity and flux into voids. Compared with electron irradiation, the void formed under L→e^- irr. is smaller. This might be ascribed the relatively higher number density of void under L→e^- irr., which decreases the number of vacancies into per void.

Not only at 723 K but also in the whole temperature range of 573-773 K, the void under L+e^- irr. is always the smaller than that under the e^- irr. and L→e^- irr.. This indicates that, as at 723 K [24], at other temperatures, the recombination of vacancies and interstitials is also enhanced under L+e^- irr., which decreases the number of vacancies into per void. and delays the void growth. Moreover, as shown in Fig. 2(b), the difference of the void size between L+e^- irr. and e^- irr increases with the increasing temperature, indicating that enhancing effect of L+e^- irr. on point defects recombination seem stronger at higher temperature.

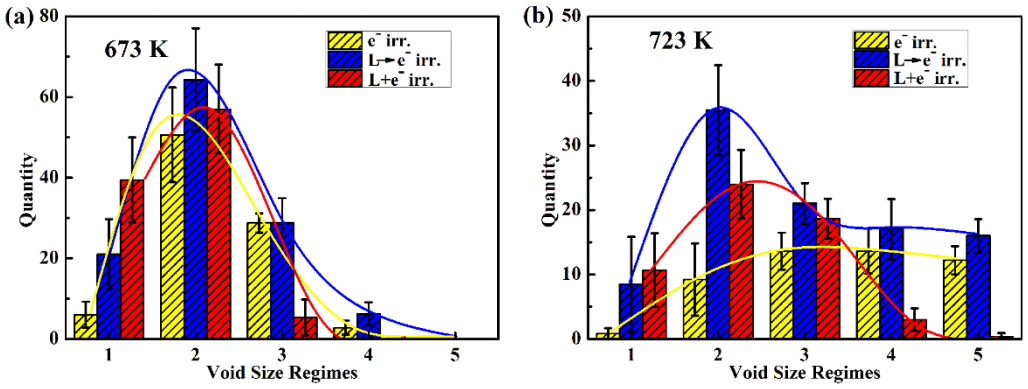

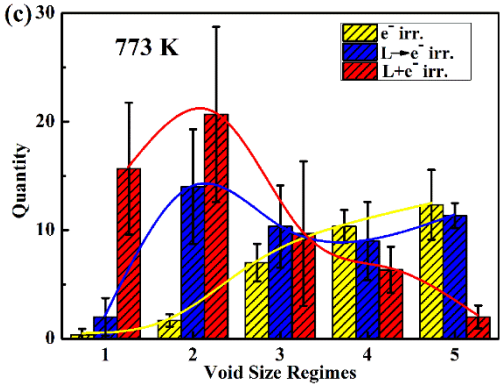

Figure 3 Size distribution of void at different temperatures. (a) 673 K, (b) 723 K, and (c) 773 K. In (a-c), 1: 0-4 nm; 2: 4-8 nm; 3: 8-12 nm; 4: 12-16 nm; and 5: ≥16 nm. The error bar indicates the standard deviation [25].

As shown above, the voids formed at 673 K, 723 K and 773 K were relatively large. To easily distinguish the difference among the three irradiation series in term of void size distribution, the voids were classified with regard to the void size, as shown in Fig. 3. It is clear that more voids belonging to regimes 4 and 5 formed with the increasing temperature, which agree well with the dependence of temperature on the void mean size (shown in Fig. 2(b)).

For L→e^- irr., a larger number of voids belonging to regimes 1 and 2 is observed than that under e^- irr. as shown in Fig. 3, which indicates the enhanced nucleation of void under L→e^- irr.. The number of relatively large void (regimes 4 and 5) is quite close to that under e^- irr.. For L→e^- irr., the voids nucleated under pre pulse-laser irradiation may preferentially grow up during the sequential e^- irr., subsequently, some large voids regimes 4 and 5) form. For L+e^- irr., rare large voids were observed, which reconfirms the prominent effect of L+e^- irr. on delaying the void growth. Moreover,

although not shown in Fig. 3, the void size distributions at 573 K and 623 K exhibit the same trends mentioned above.

4.3 Void swelling under three irradiation series

As a comprehensive result, void swelling is determined by both void mean size and void number density. With increasing irradiation temperature, the void number density and void size exhibit a decreasing and increasing tendency, respectively, resulting in a curvy profile of the temperature dependence of void swelling under both e^- irr. and L→e^- irr.. Their swelling showed a maximum at 723 K (shown in Fig. 2). Although void number density and mean size under L+e^- irr. exhibits a similar tendency to that of e^- irr. and L→e^- irr., void swelling under L+e^- irr. does not show a decreasing tendency even at 773 K. This may be attributed that the decrease of void number density under L+e^- irr. at high temperature is not as sharp as that under e^- irr. or L→e^- irr. due to the lower sink strength under L+e^- irr. [24] for the point defects to annihilate.

In Fig. 2(a) and Fig. 3, it is easy to find that the number of relatively large void (regime > 8 nm) under L→e^- irr. is close to that under e^- irr. However, the smaller voids that belong to the regime of 0-8 nm under L→e^- irr. is much more than that under e^- irr. This may explain the relatively higher void swelling under L→e^- irr. than that under e^- irr., which is found to be consistent throughout the whole temperature range of 573-773 K.

For L+e^- irr., it showed a higher number density than that under e^- irr., however, voids belonging to the large void regime (> 8 nm) are rare, resulting

in the lowest swelling compared with the other two series of irradiation. Hence, during L+e^- irr., while the void nucleation is enhanced due to its high vacancy concentration, the void growth is greatly delayed because of the enhanced recombination between interstitials and vacancies; as a result, the void swelling is remarkably suppressed under L+e^- irr. This suppressing effect and mechanism are shown to be tenable throughout the temperature range of 573-773 K.

4. Conclusions

For the temperature dependence of void swelling, e^- irr. and L→e^- irr. exhibited a peak swelling at 723 K, however, the void swelling under L+e^- irr. showed a durative increase with the increasing irradiation temperature.It was found that, void nucleation and swelling was enhanced under L→e^- irr., which should be attributed to formation of vacancy clusters and void nuclei during pre-laser irradiation owing to the laser-irradiation-introduced excess vacancies. However, compared with single electron irradiation, L+e^- irr. performed an obvious suppressing effect on void swelling at temperatures from 573 K to 773 K, which is ascribed to the enhanced recombination between interstitial atom and vacancy.

5. References

[1] K.L. Murty, I. Charit, J. Nucl. Mater. 383(2008) 189-195.

[2] P. Yvon, F. Carré, J. Nucl. Mater. 385(2009) 217-222.

[3] C.R.F. Azevedo, Eng. Fall. Anal. 18(2011) 1943-1962.

[4] S.J. Zinkle, G.S. Was, Acta Mater. 61(2013) 735-758.

[5] V.S. Neustroev, F.A. Garner, J. Nucl. Mater. 386-388(2009) 157-160.

[6] S.I. Porollo, A.N. Vorobjev, Y.V. Konobeev, A.M. Dvoriashin, V.M. Krigan, N.I. Budylkin, E.G. Mironova, F.A. Garner, J. Nucl. Mater. 258-263(1998) 1613-1617.

[7] F.A. Garner, M.B. Toloczko, J. Nucl. Mater. 251(1997) 252-261.

[8] T. Kato, H. Takahashi, M. Izumiya, Mater. Trans. 32(10) (1991) 921-930.

[9] T. Okita, W. G. Wolfer, F. A. Garner, N. Sekimura, Philos. Mag. 85(18) (2005) 2033-2048.

[10] Y. Murase, J. Nagakawa, N. Yamamoto, H. Shiraishi, J. Nucl. Mater. 258(1) (1998) 1639-1643.

[11] F.A. Garner, C.A. Black, D.J. Edwards, J. Nucl. Mater. 245(1997) 124-130.

[12] E. Wakai, N. Hashimoto, J.P. Robertson, T. Sawai, A. Hishinuma, J. Nucl. Mater. 307-311(2002) 352-356.

[13] S. J. Zinkle, J. T. Busby. Mater. Today 12(11) (2009) 12-19.

[14] E.R. Gilbert, F.A. Garner, J. Nucl. Mater. 367-370(2007) 954-959.

[15] V.D. Vijayanand, P. Parameswaran, M. Nandagopal, S. Panneer Selvi, K. Laha, M.D. Mathew, J. Nucl. Mater. 438(2013) 51-57.

[16] Y. Sekio, S. Yamashita, N. Sakaguchi, H. Takahashi, J. Nucl. Mater. 458(2015) 355-360.

[17] N. Akasaka, K. Hattori, S. Onose, S. Ukai, J. Nucl. Mater. 271&272 (1999) 370-375.

[18] F.A. Garner, M.B. Toloczko, B.H. Sencer, J. Nucl. Mater. 276(2000) 123-142.

[19] R.L. Klueh, Inter. Mater. Rev. 50(5) (2005) 287-310.

[20] T. Chen, E. Aydogan, J.G. Gigax, D. Chen, J. Wang, X. Wang, S. Ukai, F.A. Garner, L. Shao, J. Nucl. Mater. 467(2015) 42-49.

[21] M.K. Miller, D.T. Hoelzer, E.A. Kenik, K.F. Russell, Intermetallics 13(2005) 387-392.

[22] T. Yamashiro, S. Ukai, N. Oono, S. Ohtsuka, T. Kaito, J. Nucl. Mater. 472(2016) 247-251.

[23] T. Yamashiro, S. Ukai, N. Oono, S. Ohtsuka, T. Kaito, J. Nucl. Mater. 472(2016) 247-251.

[24] Z. Yang, S. Watanabe, T. Kato, Sci. Rep. 3(2013).

[25] S. Yang, Z. Yang, H. Wang, S. Watanabe, T. Shibayam, J. Nucl. Mater. 488(2017).

[26] Y. Sekio, S. Yamashita, N. Sakaguchi, H. Takahashi, Mater. Trans. 55(3) (2014) 438-442.

[27] T. Yoshiie, X.Z. Cao, K. Sato, K. Miyawaki, Q. Xu, J. Nucl. Mater. 417(2011) 968-971.

[28] H Takahashi, N Hashimoto. Materials Transactions, 1993, 34(11):1027-1030.

[29] A.V. Kozlov, I.A. Portnykh, L.A. Skryabin, E.A. Kinev, J. Nucl. Mater. 307-311 (2002) 956-960.

Chapter 2 Non-destructive evaluation of the strain distribution in selected-area He^+ ion irradiated 4H-SiC

2.1 Introduction

Due to its superior mechanical, optical and electronic properties, SiC has drawn great attention in electronic and optical applications, [1-3]. For the fabrication of SiC-based devices, ion implantation has been widely used for selected-area doping owing to the low diffusivity of dopant impurities in SiC [2]. However, high residual strain would be introduced into the SiC devices during ion implantation [4-6], which greatly changes its mechanical, optical [7] and electronic properties [8-10]. Hence, non-destructive evaluation of the residual strain state in SiC devices is great important for their fabrication and application. Especially for the development of advanced micro/nano SiC-based devices, it is necessary to fully understand the strain distribution in the whole selected-area ion-implanted SiC. However, detailed strain distribution evolution in the selected-area ion-implanted SiC devices is hard for X-ray diffraction (XRD) due to its limitation in spatial resolution (micros) [4,11-14]. Hence, a technique with a high spatial resolution is needed.

Recently, EBSD has become an increasingly important as a non-destructive strain measurement technique for the surface of crystalline materials with high spatial resolution (<50 nm) [15-17]. Up to now, the EBSD technique has been used to measure the residual strain in various semiconductors [15, 18,19]. However, few studies about the selected-area ion-implanted SiC devices have been reported. Due to its excellent

advantages, such as non-destructive measurements, high sensitivity and ease in sample preparation, Raman scattering has been widely used to characterize the semiconductors [4,20]. Based on the confocal Raman microscopy (CRM) technique, Raman scattering is also used to evaluate the stress distribution in Si around the indentation at the sub-micrometer scale [19]. Hence, the CRM technique may also be appropriate to evaluate the residual strain in selected-area ion-implanted SiC.

In this chapter, the strain distribution in the whole selected-area ion-implanted 4H-SiC was first evaluate using these two promising techniques of EBSD and CRM.

2.2 Experimental procedure

Herein, a commercial n-type 4H-SiC (0001) single-crystal substrate was used with size of $10 \times 10 \times 0.33$ mm^3. This substrate was irradiated with 100 keV He^+ ions to a fluence of 5.0×10^{16} cm^{-2} at room temperature. During irradiation, a mask was used to cover the sample with a hole 8 mm in diameter in order to clearly distinguish the irradiated and unirradiated areas, as shown in Fig. 2.1(a).

After irradiation, atomic force microscopy (AFM; KEYENCE VN–8000) was used to measure the swelling of the irradiated area through comparing the difference between the irradiated and unirradiated areas in height. The EBSD patterns was acquired using a field emission scanning electron microscope (SEM; JEOL JSM–7001FA) equipped with an EBSD detecto. During scanning, the sample were tilted to 70°, and the acceleration voltage

is 20 kV, with a scan area of 20×20 μm^2 and scan step of 0.1 μm. The patterns of EBSD were stored as 12-bit gray scale in TIFF format, uncompressed and 1392×1040 pixels. To clearly exhibit the strain distribution, two orthogonal regions were scanned, and both an unirradiated and an irradiated area are contained in each region as shown in Fig. 2.1(b). During EBSD scanning, the boundary between the irradiated and unirradiated areas was set almost vertical (region 1) or horizontal (region 2) to the scanning direction, which was convenient for the sequent statistics analysis whereby the strain values of each column were averaged. Using the CrossCourt 3 software, the strain distribution in scanning area was achieved by analyzing the EBSD patterns. Regions of interest (ROIs) 256 × 256 pixels were described, and 20 ROIs were automatically selected. The irradiated/unirradiated interface location in the EBSD strain image was determined by comparing with SEM image,

The Raman backscattering experiment was performed beside the EBSD scanning regions as shown in Fig. 2.1(b) at room temperature using Raman microscope (HORIBA XploRA), and a laser wavelength of 532 nm, a 2400 groove/nm grating and 100–2000 cm^{-1} scanning range were selected. A spot of about 2 μm in diameter was focused for the laser beam, and the CRM technique with a confocal aperture of 100 μm was used to collect the Raman spectra data. The detection was carried out by the point-to-point method along the direction from the irradiated area to the unirradiated area to measure the strain. A schematic image of the measurement procedure is shown in Fig. 2.1(c), illustrating Position 3 (P3) in the irradiated area, Position 2 (P2) in the unirradiated area close to the irradiated/unirradiated

interface, and Position 1 (P1) in the unirradiated area relatively far from the interface. Using the Voigt function (i.e., a weighted sum of a Gaussian and Lorentzian distribution) [4], the peak positions were obtained by fitting the peak.

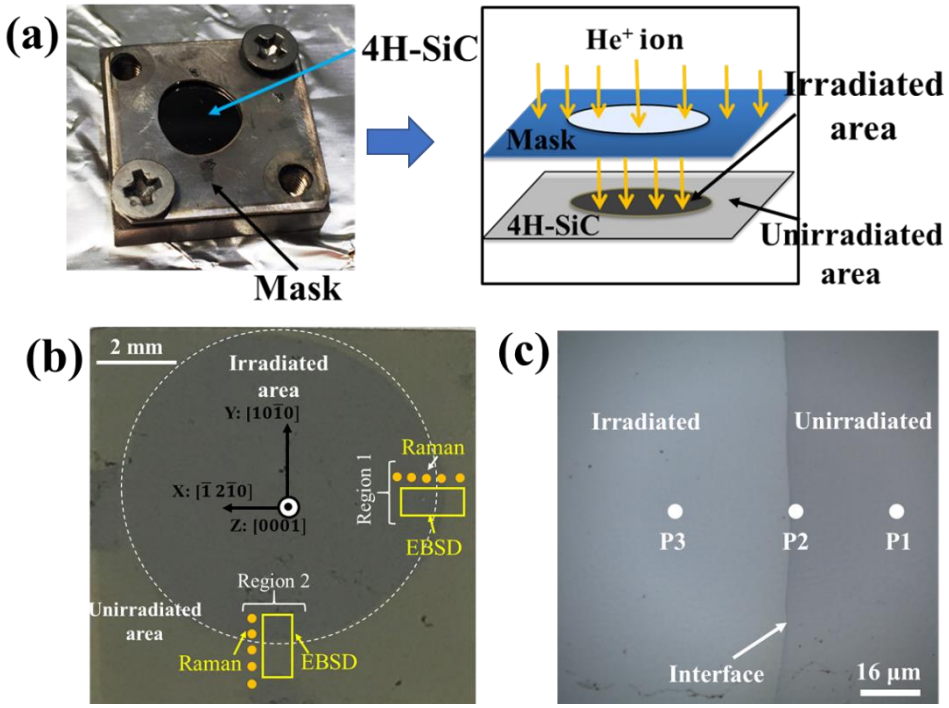

Fig. 2.1. Schematic images of experiment configuration. (a) Sample arrangement during ion implantation (b) EBSD and Raman scanning regions. (c) the P1, P2 and P3 locations mentioned in Fig. 2.4(a) of manuscript.

2.3 Results and discussion

2.3.1 Strain distribution evaluated by EBSD

After irradiation, swelling of the irradiated area was confirmed by AFM, where the surface of the irradiated area was higher than that of substrate with a value of 25.7 ±4.5 nm (Fig. 2.2). The residual elastic strain measured by EBSD was mapping in Fig. 2.3. It is clear that the residual strain in the

irradiated area exhibits an anisotropic distribution of positive and negative classification along the different directions. In contrast to the ε_{xx} and ε_{yy} components exhibiting compressive strain, the positive classification of ε_{zz} indicates a tensile strain and expansion of the lattice spacing, which agrees with the swelling measured by AFM, as shown in Fig. 2.2. In homogeneously-irradiated SiC, tensile strain is typically resulted from a positive volume change of the crystal via the distortion field of the defects [4]. However, for selected-area ion-implanted SiC, the compressive strain was introduced into the horizontal (*X*) and vertical (*Y*) directions with tensile strain in the *Z* direction. This should be attributed to the confined volume expansion in the *X* and *Y* directions in the irradiated area.

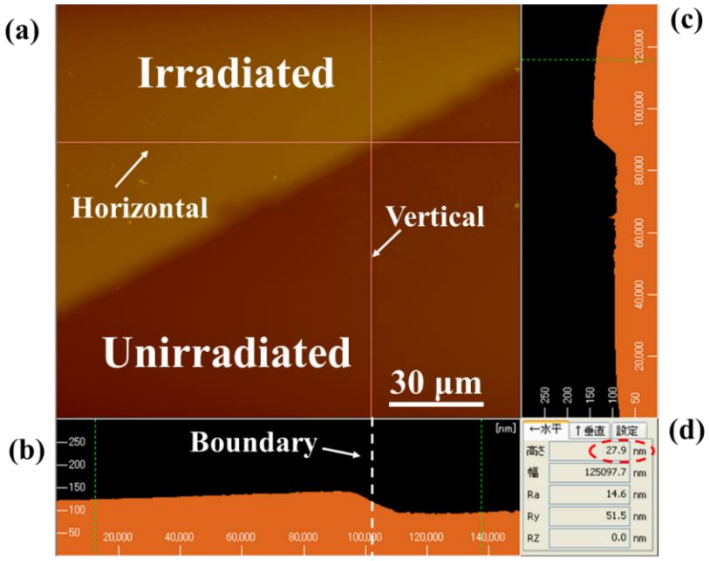

Fig. 2.2. AFM image of 4H-SiC surface. (a) AFM surface image. (b) Height distribution in horizontal direction. (c) Height distribution in vertical direction. (d) Height difference for the two positions pointed out in (b).

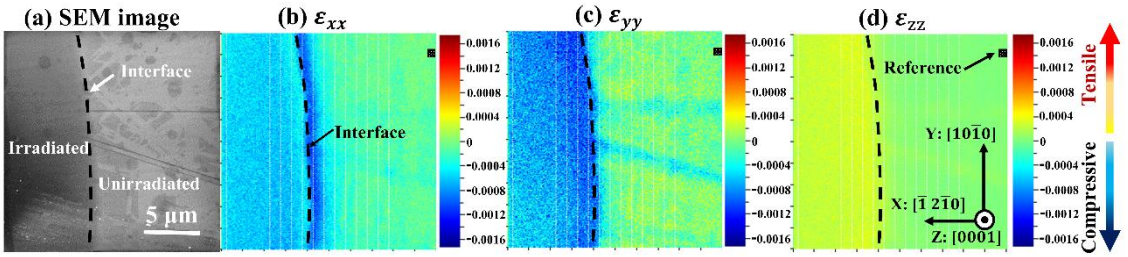

Fig. 2.3. Strain maps in selected-area He^+ ion irradiated 4H-SiC. (a) SEM image, (b–d) residual elastic strains with (b) ε_{xx}, (c) ε_{yy}, and (d) ε_{zz} representing the strain horizontal (*X*), vertical (*Y*) and normal to the sample surface (*Z*), respectively. A reference was selected for the strain analysis at unirradiated area as shown in (d). Strain formed at some positions of unirradiated area is owing to the scratch on the sample surface [21].

Further, for the strain distribution in the area around the irradiated/unirradiated interface, it is also non-homogeneous with a strain concentration in this area. For the ε_{xx} component, it is interesting to find that the strain is concentrated in both the irradiated and unirradiated areas. However, for the component ε_{yy} and ε_{zz}, they typically only appear in the irradiated area. The distribution of ε_{xx} indicates that strain is introduced not only into the irradiated area but also the unirradiated surrounding substrate, which should be ascribed to the expansion of the irradiated area.

2.3.2 Raman spectra variation

Using CRM technique, the microstructural variation and strain distribution in the selected-area ion-irradiated sample were detected. The 4H-SiC exhibits Raman active modes of A_1, E_1 and E_2, where the A_1 and E_1 modes are split into longitudinal (LO) and transverse (TO) optical modes [20, 22]. In order to clearly clarify the variation of Raman spectrum, Figure 2.4(a)

displayed the spectra excited from three different regions, that is unirradiated area (P1), unirradiated area close to the unirr./irr. interface (P2), and irradiated area (P3) (P1, P2 and P3 corresponding to the positions in Fig. 2.1(c)). In the unirradiated area (P1), the major modes ascribed to the Si–C vibration are labelled. The sharp peaks located at 775.5 and 796.4 cm^{-1} represent the E_2(TO) and E_1(TO) modes, respectively [22]. The broad peak detected around 982 cm^{-1} is ascribed to A_1(longitudinal optical phonon–plasmon coupled (LOPC)) modes [18, 20], whose line shape correlated with the carrier density [23, 24]. The broad and weak peak of the A_1(LOPC) peak herein suggests a relatively high carrier density in our sample. The peaks detected at 200, 263 and 609 cm^{-1} are attributed to the E_2(transverse acoustic (TA)), E_1(TA) and A_1(longitudinal acoustic (LA)) modes, which belong to the second-order Raman peaks of 4H-SiC [20, 22].

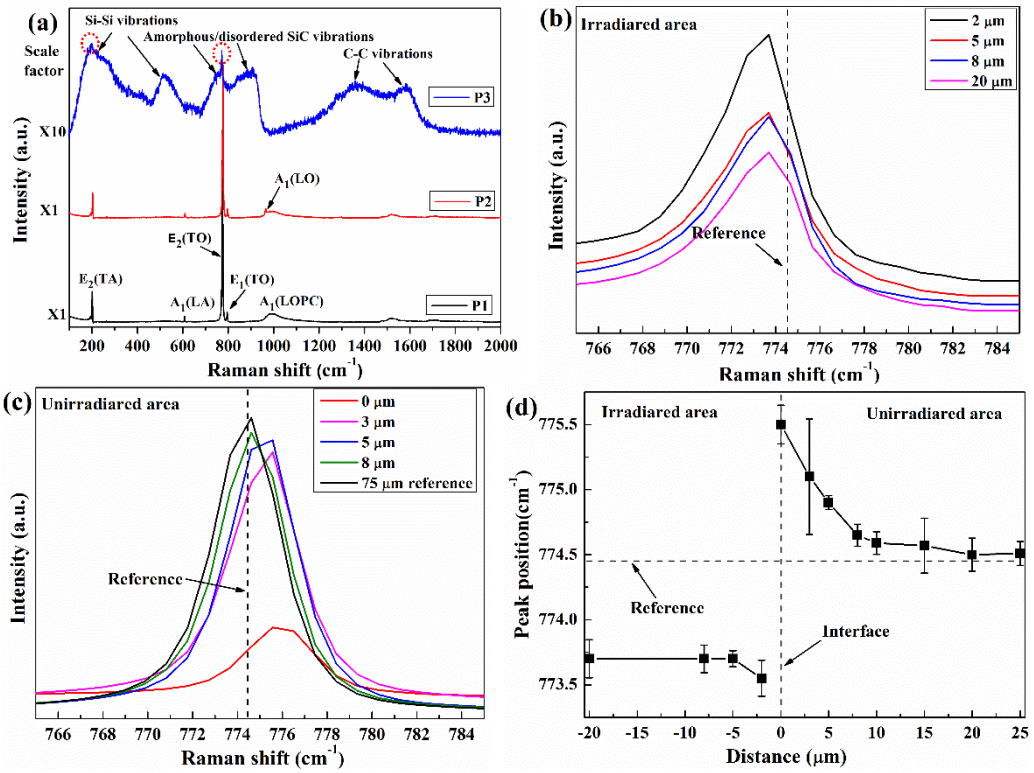

Fig. 2.4. Raman spectra obtained from different positions of the He^+ ions irradiated 4H-SiC. (a) Raman spectra obtained from different positions, corresponding to the unirradiated position (P1), unirradiated position close to the interface (P2), and irradiated position (P3). (P1, P2 and P3 corresponding to the positions in Fig. 2.1(c)) (b, c) Peak shift of E_2(TO) in the (b) irradiated and (c) unirradiated areas. The insert numbers correspond to the distance from the interface. (d) Peak position of E_2(TO) as a function of the distance from the interface [21].

After He^+ ion irradiation, some new broad peaks appear (P3 in Fig. 2.4(a)) with the disappearing of the Raman peaks of the crystal Si–C vibrations discussed above. These new peaks are ascribed to the vibration of the Si–Si bands (100–600 cm^{-1}), Si–C bands (700–1000 cm^{-1}) and C–C bands (1100–1800 cm^{-1}) [22]. The appearance of the Si–Si and C–C bonds and their relatively high intensity demonstrate a high degree of disorder of SiC in the irradiated area, even for an amorphous state [22]. Some short-range order should be still maintained in the irradiated area deduced from the remaining E_2(TA) and E_2(TO) peaks, which marked by red circle in Fig. 2.4(a). For the region in the unirradiated area but close to the interface, such as the P2 position, its Raman spectrum is similar to that of P1, suggesting a good crystallinity in this region. However, a sharp new peak appears at 963 cm^{-1} beside the broad peak A_1(LOPC), which is identified as A_1(LO) [20], The appearance of this new peak implies a change of microstructure and carrier density in this area that will be discussed in section 2.3.3.

In addition to the above Raman mode variations, irradiation would also

lead to the shifts in the peak positions for some Raman modes, such as the A_1(LA) and E_2(TO) modes, which should be attributed to the irradiation-induced strain. Hence, peak shift of Raman modes can be used for strain evaluation [20, 25]. Herein, the Raman mode we used to evaluate the strain is the E_2(TO) mode due to its relatively high intensity, and its peak still maintain even after irradiation as shown in Fig. 2.4(a). A reference of Raman spectrum, which is regarded as the strain-free state, was acquired at a distance of about 75 μm in the unirradiated area, as we assume that the effect of ion implantation is negligible in this area. The peak position of the E_2(TO) mode in the reference spectrum is about 774.4 cm^{-1} as shown in Figs. 2.4(b) and 2.4(c). In term of the strain-free state reference spectrum, the peak position of E_2(TO) mode shifts to lower frequencies in the irradiated area and to higher frequencies in the unirradiated area close to the interface, representing tensile and compressive strain states [20, 25, 26], respectively. Further, it is confirmed that compressive strain would be introduced into the surrounding substrate in the selected-area ion irradiated SiC. The peak shift of E_2(TO) correlates with the distance from the interface, suggesting a heterogeneous strain distribution in this region (Fig. 2.4(d)). The largest peak shift appears at the interface, implying a concentrated strain at this position that agree well with the EBSD results. In addition, owing to strain or defects, the full width at half maximum (FWHM) of E_2(TO) also increases with distance to the interface, which is shown in Fig. 2.5.

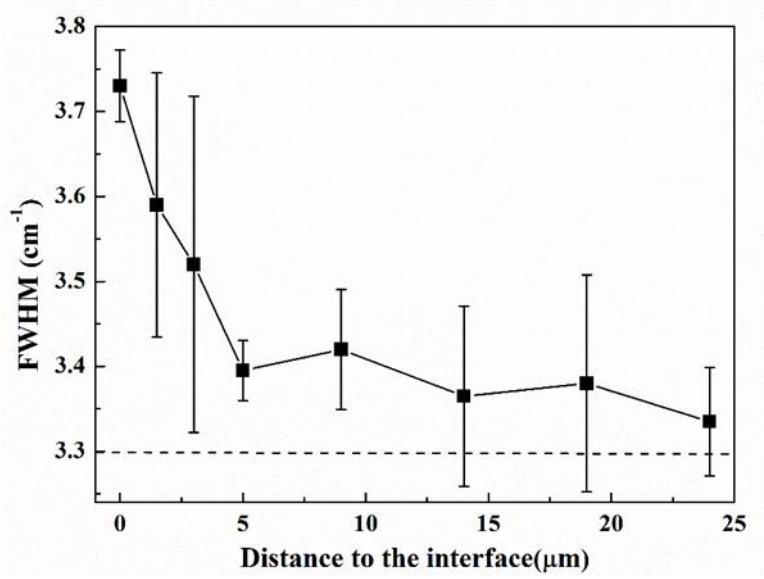

Fig. 2.5. FWHM of E_2(TO) with the distance to the interface.

2.3.3 Comparison of strain distribution evaluated by EBSD and CRM

The strain distribution evaluated by both CRM and EBSD are displayed in Fig. 2.6. For EBSD, the statistical result was achieved by averaging the measured strain values obtained from a narrow surface area (i.e., column) parallel to the interface. In Raman measurements, Rohmfeld et al. have reported the correlation between the TO mode shift and with the strain in 3C-SiC [26], which we have assumed to also be approximate for the 4H-SiC herein.

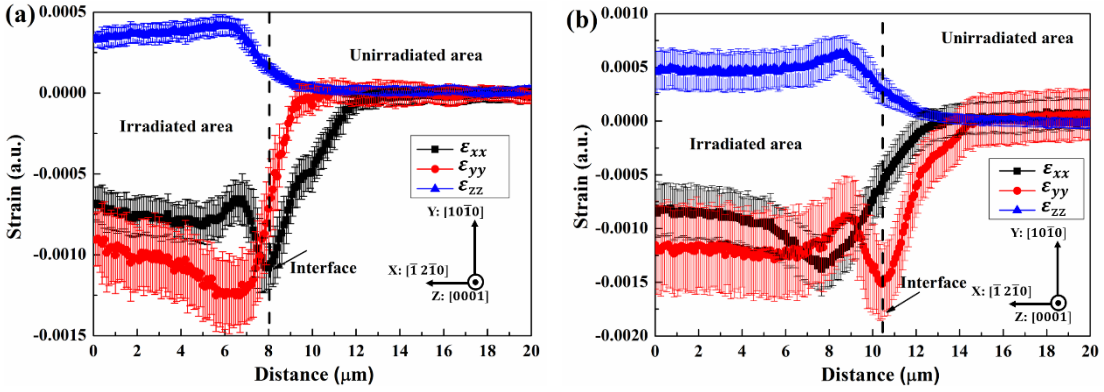

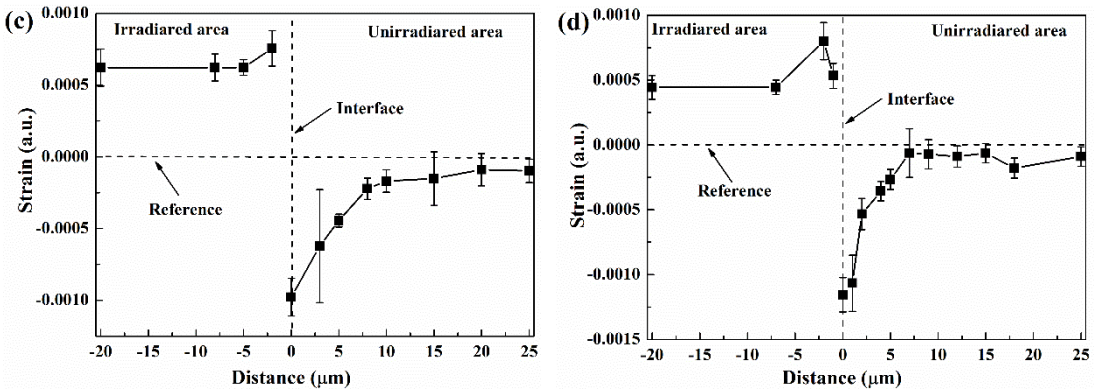

Fig. 2.6. Residual strain evaluated by (a, b) EBSD and (c, d) CRM. (a) and (c) are obtained from the region1 of Fig. 2.1(b), representing the EBSD and CRM results in Fig. 2.3 and Fig. 2.4, respectively. (b) and (d) are acquired from region2 of Fig. 2.1(b), and their original EBSD strain maps and peak shift of Raman spectra are displayed in Fig. 2.7 and Fig. 2.8, respectively [21].

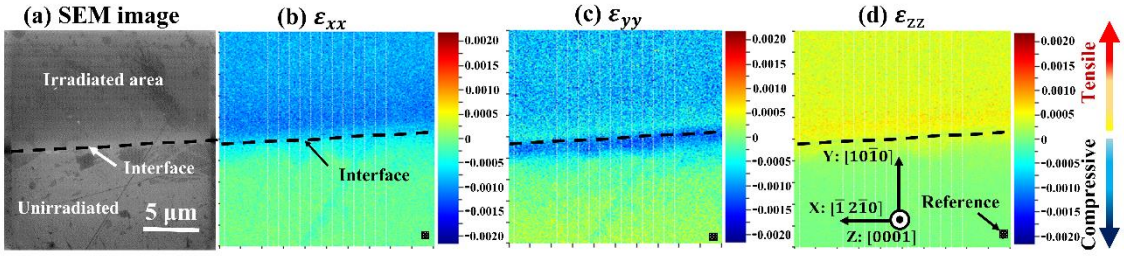

Fig. 2.7. Strain maps around the irradiated/unirradiated interface. The scanning area corresponds to region2 of Fig. 2.1(b), where the interface is vertical to the Y axis. (a) SEM image, (b–d) residual elastic strains (b) ε_{xx}, (c) ε_{yy}, and (d) ε_{zz}, respectively corresponding to the strain horizontal (X), vertical (Y) and normal to the sample surface (Z). These images correspond to the Fig. 2.6(b).

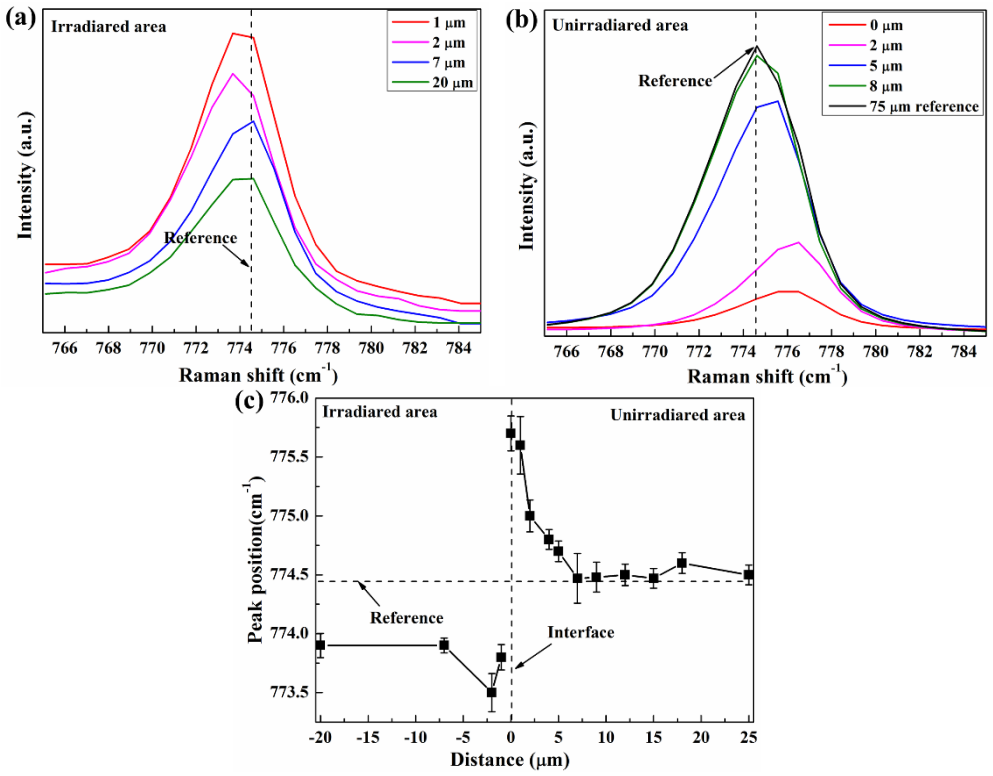

Fig. 2.8. Peak shift of E_2(TO) in the (a) irradiated and (b) unirradiated areas. The insert numbers represent the distance from the interface. (c) Peak position of E_2(TO) as a function of the distance to the interface. These results correspond to the Fig. 2.6(d).

The EBSD results display the residual strain along three orientations in Fig. 2.6 (a). The strain appears relatively homogeneous adjacent to the left edge of the EBSD scanning area, which might correspond to the strain condition in the center of the irradiated area with a mean value of −0.00075, −0.00099 and +0.00036 for ε_{xx}, ε_{yy} and ε_{zz}, respectively. As close to the interface, a concentrated strain is clearly exhibited around the interface with a value of -0.0011, -0.0013 and +0.00043 in *X*, *Y* and *Z* directions, respectively.

As shown in Fig. 2.3 that strain concentration region seems different for

ε_{xx}, ε_{yy}, which is clearly confirmed in Fig. 2.6(a). Moreover, it is interesting to find that actually only the strain in X direction extended into the substrate, while the strain in Y and Z direction sharply decreased and almost disappeared in the unirradiated area. Herein, the ε_{xx}, ε_{yy} and ε_{zz} represent the strain in the $[\bar{1}2\bar{1}0]$, $[10\bar{1}0]$ and [0001] directions, respectively. To reveal the correlation between the strain distribution and the crystallographic orientation in ion-irradiated 4H-SiC, the strain distribution in another region where the interface is vertical to the Y axis was also evaluated by EBSD, and the obtained results were displayed in Fig. 2.6(b). Close to the left edge, the strain distribution shown in Fig. 2.6(b) is similar to that in Fig. 2.6(a). However, around the interface it is ε_{yy} rather than ε_{xx} that concentrated around the interface and dominantly extended into the substrate, when the interface is vertical to the Y axis. This implies that around the interface, the distribution of ε_{xx} and ε_{yy} might be not ascribed to the crystallographic orientation but to the correlation between strain direction and interface direction, and that strain might easier extend into the substrate along the direction vertical to the interface. However, it is found that the strain along $[10\bar{1}0]$ (ε_{yy}) is always higher than that along $[\bar{1}2\bar{1}0]$ (ε_{xx}) in the Figs. 2.6(a) and 2.6(b), implying that the strain value of ε_{xx} and ε_{yy} may depends on the orientation. Moreover, it is interesting to find that at the irradiated region about 2 μm to the interface where the ε_{zz} reaches a peak value, the distributions of ε_{xx} and ε_{yy} show a peak and a valley simultaneously as displayed in Fig. 2.6(a) (valley and peak for ε_{xx} and ε_{yy} in Fig. 2.6(b)), suggesting an inverse change of decrease and increase for ε_{xx} and ε_{yy} at

this region. It is reported that irradiation-induced strain is driven the the defects introduced during irradiation, and that defects perform different roles to the strain accumulation. For instance, interstitial atoms usually resulting in the volume expansion while vacancies would lead to the compressive strain [27]. Hence, the value of ε_{xx}, ε_{yy} and ε_{zz} and their simultaneous variation near the interface should be ascribed to the arrangement of irradiation-induced defects in different crystallographic orientations.

As shown in Figs. 2.6(c) and 2.6(d), the results measured by Raman scattering provide a relatively homogeneous tensile strain in the irradiated area. In the substrate (unirradiated area), a concentrated compressive strain appears at the interface, which gradually decreased with distance from the interface. The strain distribution measured by Raman scattering agrees well with some EBSD results. For instance, in the irradiated area, the tensile strain evaluated by Raman scattering is in good agreement with the ε_{zz} strain measured by EBSD. Besides, the strain distribution tendency in the substrate evaluated by Raman scattering is also consistent with that of the EBSD results. Both EBSD and CRM are powerful techniques with high spatial resolution that can be used to measure the strain distribution in selected-area ion-irradiated SiC. However, with respect to the residual strain, the EBSD results obviously provide more information than that of CRM. For example, the EBSD results directly provide a correlation between the strain and the orientation as shown in Fig. 2.3 and Fig. 2.6. The CRM technique could also be used to determine the strain components in different orientations, however, it is necessary to perform off-axis and polarized excitation [28].

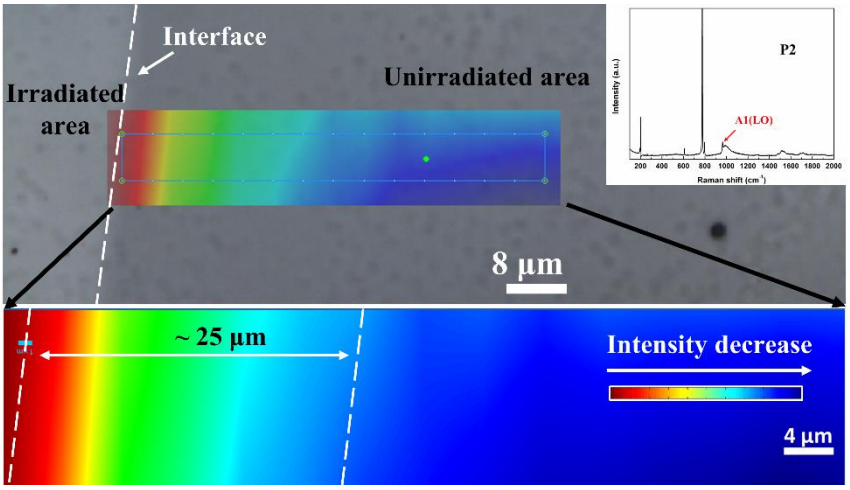

Fig. 2.9 Raman mapping scanning results of A_1(LO) mode around the interface.

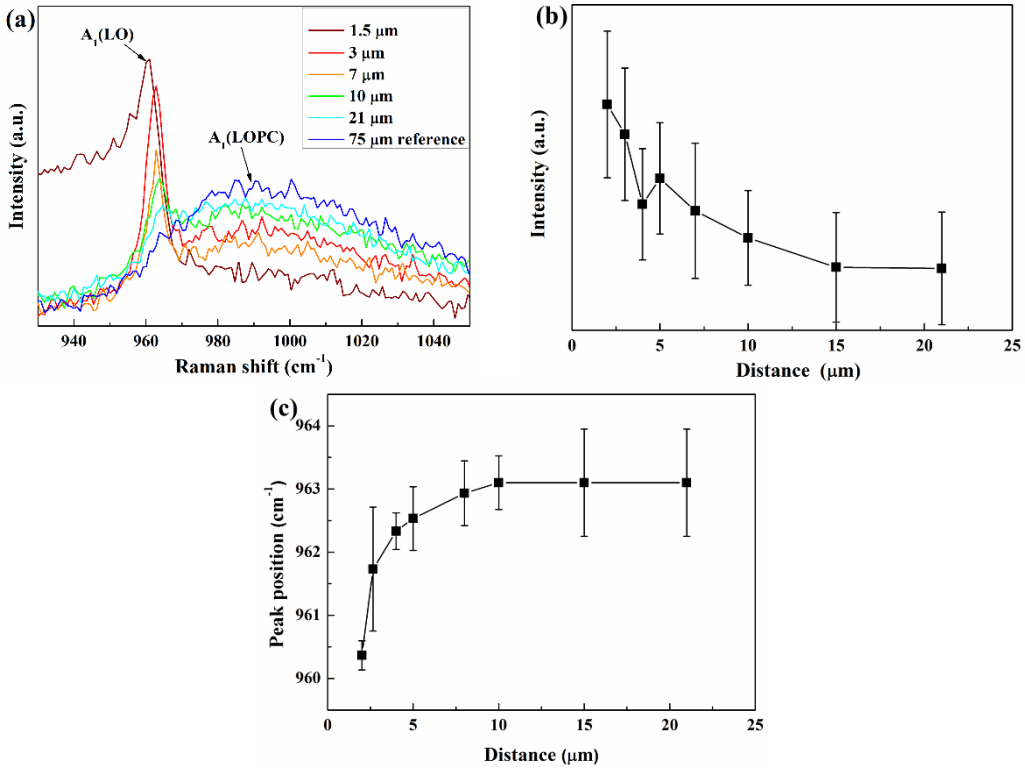

Fig. 2.10. Variation of the A_1(LO) mode in the substrate close to the irradiated/unirradiated interface. (a) Variation of the A_1(LO) mode (b) intensity and (c) peak position of A_1(LO) as a function of the distance from the interface [21].

As discussed above that the EBSD technique is more convenient to investigate the correlation between the strain and the orientation, while

Raman scattering is useful to explore the variations in microstructure and electronic properties. For instance, appearance of the A_1(LO) peak and its variation in the unirradiated area close to the interface were observed by CRM. In Fig. 2.9, the mapping scanning results of A_1(LO) peak around the interface provides a direct and clear evidence that the intensity of A_1(LO) peak gradually decreases as moving away from the interface into the unirradiated area. Detailed variation of the A_1(LO) peak was shown in Fig. 2.10. It is clear that the A_1(LO) peak decreases in intensity (Fig. 2.10(b)) and shifts to higher frequencies (Fig. 2.10(c)), implying a gradual increasing of carrier density in this region and a coupling of the A_1(LO) phonon to the plasmon mode (i.e., A_1(LOPC) mode) [20, 24]. Moreover, both the A_1 (LO) peak position and intensity display a dependence on the distance to the interface, and both show a similar tendency to the strain distribution measured by CRM and EBSD in this region. This suggests that the emergence and change of the A_1(LO) mode could be ascribed to the effect that strain and defects have on the carrier density. The uniformity of carrier density is important for the performance of SiC-based electronic devices. Thus, it should also be taken into consideration for the strain/stress effect on the carrier density of SiC during fabrication and application.

2.4 Summary

A detailed strain distribution in the selected-area He^+ ion-irradiated 4H-SiC was provided by EBSD and CRM, whose results agree well. It is validated that both EBSD and CRM techniques are suitable to evaluate the strain in

selected-area ion-irradiated SiC. The results show that strain is not only introduced into the irradiated area, but also into the unirradiated substrate because of irradiation-induced swelling. Furthermore, the concentration of a higher compressive strain is found around the interface between the unirradiated and irradiated areas. The strain distribution around the interface may depend on the correlation between the strain and interface direction, and the relative strain degree may correlate with the crystallographic orientation. Using CRM, the changes in the A_1(LO) mode were also found in the strain-introduced substrate, which might be ascribed to the effect of defects and strain on the carrier density in this region.

Chapter 3 Anisotropic defect distribution in the He^+ ion irradiated 4H-SiC and stress effect on defect distribution

3.1. Introduction

In chapter 2, the detailed strain distribution in the selected-area He^+ ion irradiated 4H-SiC was evaluated using EBSD and CRM. At the same time, an anisotropic swelling or strain was also founded in the irradiated area. Different from conventional homogeneous swelling of cubic materials [1-8], irradiation might induce anisotropic swelling in hexagonal close packed crystal, such as α-SiC [9]. The anisotropic swelling recently has gain great interest, because such anisotropy would result in degradation in properties of ceramic materials such as aluminum nitride [10], silicon nitride [11]. Moreover, fractures or microcracks has been reported to preferentially occurs at the grain boundaries in these materials with anisotropic swelling [12, 13]. It is therefore reasonable that α-SiC and other ceramics with a hexagonal crystal structure may display irradiation-induced different expansion on different direction (including <a> and <c> axes) leading to loss of original crystal integrity and degradation of mechanical property. However, the mechanism underlying the anisotropic swelling is still far from well understood in terms of physical mechanism and microstructural process.

According to the correlation of defects with swelling that volume swelling is dominated by various defects, especially for point defects or tiny defect clusters at room temperature [14-20], it is reasonable to consider that the anisotropic swelling/strain should be correlated with the defect distribution

in different crystal direction. In order to obtain insights of anisotropic swelling/strain mechanism, the fundamental understanding of the detailed defects distribution of different direction in the SiC with anisotropic swelling should be gain. However, the detailed defects distribution for different direction in the irradiated 4H-SiC is quite few reported.

In this chapter, the defects distribution of different direction in these samples with anisotropic swelling was explored using various transmission electron microscopy (TEM) techniques. An anisotropic defects distribution was detected in the selected-area He^+ ion irradiated 4H-SiC. The stress effect on the defect distribution was also discussed.

3.2. Experimental procedures

Single-crystalline n-type 4H-SiC (0001) substrates with size 10 × 10 × 0.33 mm^3 were irradiated with 100 keV He^+ ions at room temperature to fluences of 1×10^{15} and 5×10^{16} cm^{-2}. During irradiation part of the sample was covered by a mask to perform selected-area ion irradiation. More details of the selected-area ion irradiation are given in chapter 2. For a comparison, a non-selected-area He^+ ion irradiated 4H-SiC was also made at room temperature with a fluence of 5×10^{16} cm^{-2}. The damage and injected helium profile for He^+ ion into SiC was calculated by SRIM 2013 using full-cascade mode. The sample density and threshold displacement energy for C and Si sub-lattices used in calculation were 3.21 $g\cdot cm^{-3}$, 21 and 35 eV [21], respectively. The total penetration depth predicted by simulation is about 600 nm, and the highest damage is located at about 450 nm.

After irradiation, cross-sectional thin foils for TEM were made from

irradiated areas using gallium ions in a focused ion-beam system (JEOL, JEM-90320FIB). The ion accelerating voltage is 30 kV. The microstructure features of the irradiated 4H-SiC were observed by TEM (JEOL, JEM-2000FX) at the operation voltage of 200 kV. The average size and number density of defects were counted and calculated using weak-beam dark field TEM images, and 5 images were used for each calculation. The thicknesses of observation regions were measured by electronic energy loss spectrum (EELS) using Cs-corrected STEM (FEI, Titan G2 60-300). High-resolution TEM (HR-TEM) analysis, high-angle annular dark field (HAADF) and annular bright field (ABF) scanning transmission electron microscopy (STEM) and core-loss EELS studies were also carried out using Cs-corrected STEM. The operation voltage was 300 kV. The HAADF and ABF STEM images were simultaneously acquired with a 17.8 mrad semi-convergence angle and 50–200 and 10.36–24.48 mrad collection angles for the HAADF and ABF, respectively.

Using electron backscattered diffraction (EBSD) and Crosscourt3 software, the stress in irradiated area was measured. A field emission scanning electron microscope (SEM; JEOL JSM–7001FA) equipped with an EBSD detector was used to obtain EBSD patterns, operating at an acceleration voltage of 20 kV, a sample tilt of 70° and a scan size and scan step of 20×20 μm^2 and 0.1 μm, respectively. The stress was obtained by analyzing the EBSD patterns using the CrossCourt 3 software. Details of this strain/stress measurement method using EBSD and the strain results were shown in chapter 2.

Defect distribution after annealing was also explored by annealing thin foil TEM samples at 600 °C for 30 min using multi-beam ultra-high voltage electron microscope (multi-beam HVEM) (JEOL, JEM-ARM1300). The defects characterization still used 200kV TEM (JEOL, JEM-2000FX). Besides, thin foil 4H-SiC samples were irradiated by electron using multi-beam HVEM. These TEM samples for electron irradiation were made from unirradiated areas of selected-area He^+ ion irradiated 4H-SiC samples using FIB, and before electron irradiation, these TEM samples were annealed at 600 °C for 30 min to remove the potential internal stress. The electron irradiation was performed at room temperature at an accelerating voltage of 1.25 MV with irradiation area diameter of about 2 μm. The electron flux was about 1.2×10^{24} $e\cdot m^{-2}\cdot s^{-1}$, and the total irradiation time was 1 hour. During irradiation, the electron beam was controlled to parallel to the $[11\bar{2}0]$ orientation. After electron irradiation, the defect distribution in electron irradiated thin foil 4H-SiC samples was also characterized using 200kV TEM (JEOL, JEM-2000FX).

3.3 Results

3.3.1 Microstructure in He^+ ion irradiated 4H-SiC

After irradiation, the internal microstructures of He^+ ion implanted 4H-SiC with a fluence of 5×10^{16} cm^{-2} were shown in Fig.3.1(a), combined with the simulated damage and He^+ distribution profiles by SRIM 2013. Due to the different irradiation damage level, three kinds of region with distinct bright-field image contrast (gray, black and white) are discernible in Fig.3.1(a), and are denoted by A-, B- and C-layer, and B layer is further

separated into B_1 and B_2 layers. Derived from the TEM image contrast and the selected-area diffraction, the near surface layer (A-layer) with the gray contrast contains only minimal damage and still maintains good crystallinity (as shown in Fig.3.1(b)). However, at the highest damage region where the contrast shows white (C-layer), an amorphous state was confirmed by diffraction observation as shown in Fig.3.1(c). Besides, the two black layers (B_1- and B_2-layers) adjacent to amorphous layer might contain significant defects.

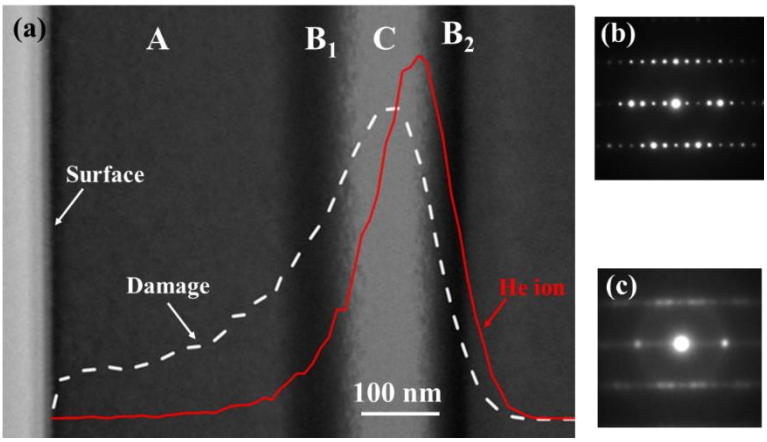

Fig. 3.1. Internal microstructure distribution of He^+ ion irradiated 4H-SiC up to a fluence of 5 x 10^{16} cm^{-2}. (a) Cross-sectional micrograph of He^+ implanted 4H-SiC and depth distribution of displacement damage (white dash line) and He concentration (red solid line). The image was taken along $[11\bar{2}0]$ zone. (b) and (c) Diffraction patterns corresponding to A- and C-layer.

To resolve the defects in each region, HR-TEM images are acquired along $[11\bar{2}0]$ orientation, which are displayed in Fig.3.2, with Fig.3.2(a), 2(b) and 2(c) acquired from the A layer, B_1 layer and the interface between B_1 and C

layer (amorphous/crystal interface), respectively. In the A layer, the basal plane structure is maintained, which agrees well with the diffraction analysis shown in Fig.3.1(b). Also, few defects contrast can be observed (Fig.3.2(a)), The main defects in the surface region might be point defects, or tiny defect clusters that hard to distinguish clearly by HR-TEM [22]. However, in the relatively high damage region (B_1 layers), the crystal shows an obvious disorder as shown in Fig.3.2(b). Black spots are clearly observed in this image, which are so-called black spots defects (BSDs) [7], types of point defect clusters composed by vacancies and interstitials in irradiated SiC. It should be pointed out that a small fraction of small dislocation loops may also be present according to previous reported results [8], but here we consider all of them as BSDs. The Fig.3.2(c) shows microstructure near the amorphous/crystal interface. BSDs are also visible in the region near the amorphous/crystal interface, some even locate in the amorphous region like an island.

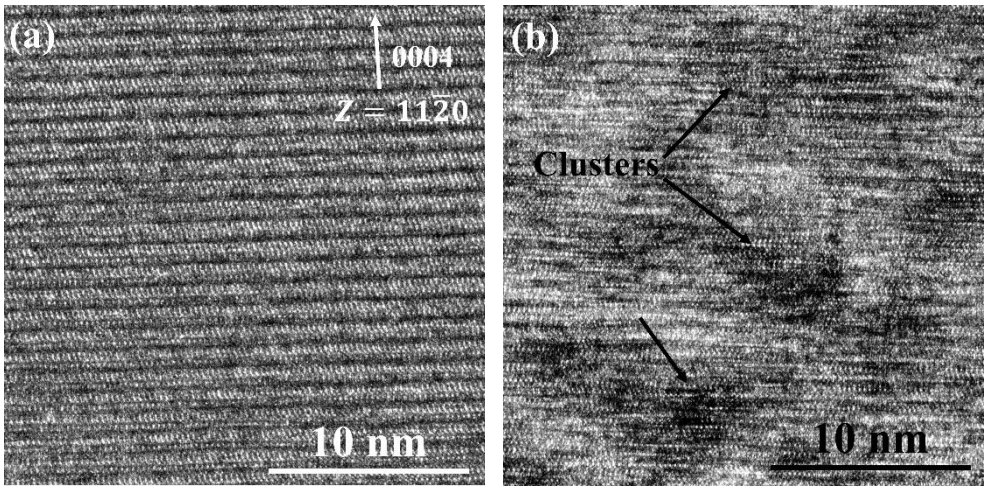

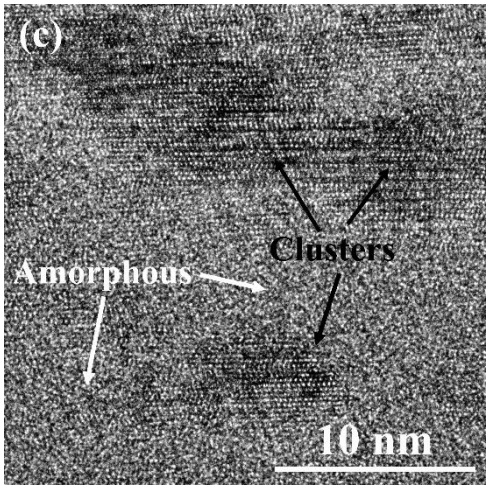

Fig. 3.2. High resolution images taken from different regions. (a) In A layer. (b) In B_1 layer. (c) Around the interface between B_1 and C layer. The images were taken near the $[11\bar{2}0]$ zone axis.

3.3.2 Defects distribution

The presence of a lattice defect in the crystal materials would lead the planes close to the defect to bend. Bending of the lattice planes results in a change of diffraction and therefore a change in the contrast of the image, and the defects can be learned about by studying the contrast in the TEM image [23]. To identify characteristics of these defects cluster (BSDs), different reflections corresponding to different sets of lattice plane were used to explore the defect distribution in selected-area He^+ ion irradiated 4H-SiC. The distribution of BSDs under different TEM two-beam observation conditions are shown in Fig.3.3, with Fig.3.3(a, b) at diffraction vector g = [0004] and Fig.3.3(c, d) at g = $[11\bar{2}0]$. These images are taken from the same area, and for orientation, a mark was made by focus electron beam irradiation using JEM-2000FX (200 kV). Under two beam observation

condition, the distribution of BSDs is distinct in both the bright-field and dark-field image with of black spots (Fig.3.3(a) and 3(c)) and white spots (Fig.3.3(b) and 3(d)), respectively. More BSDs obviously appear in [0004] direction (Fig.3.3(a) and (b)) than that in $[11\bar{2}0]$ (Fig.3.3(c) and (d)). Moreover, the defects seen in the reflection vector of [0004] become invisible with reflection vector of $[11\bar{2}0]$, which was marked by white square, and vice versa (mark by red circle). Since the details of the lattice plane bending generally depending on the characteristics of the defect [23]. According to the $\boldsymbol{g} \cdot \boldsymbol{b} = 0$ invisible criterion for planar defects [24-26], the defects observed in Fig.3.3 should be a kind of planar defect that formed in corresponding orientation or plane. Similar results were also observed for direction g = [0004] and g = $[10\bar{1}0]$ that defects seen in one direction become invisible in the other direction. Hence, these BSDs observed at different diffraction conditions seem to be the plane defects formed in each reflecting plane.

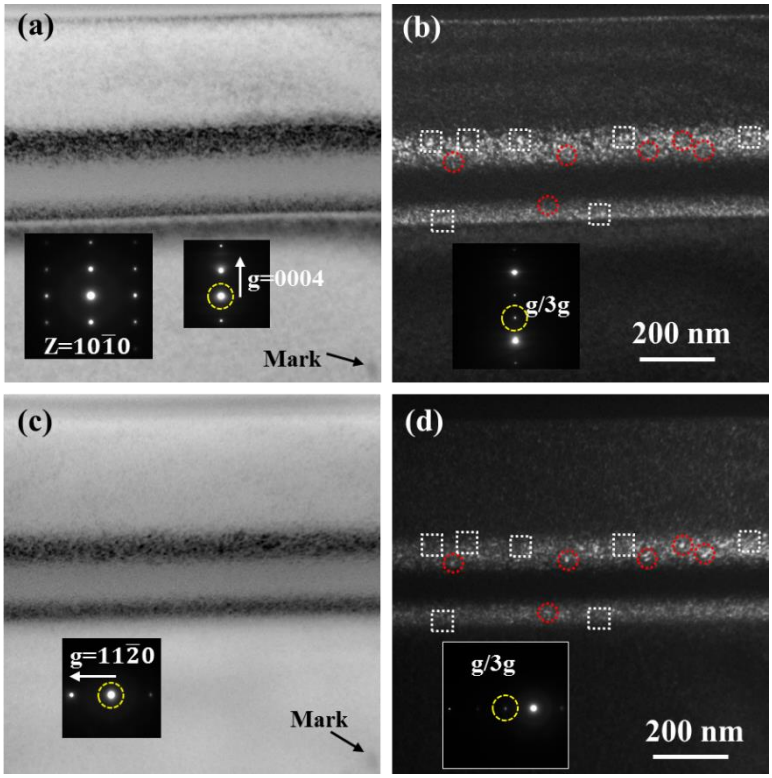

Fig. 3.3 TEM image of BSDs at different two-beam observation conditions. (a, b) and (c, d) at diffraction vector g=0004 and g=11$\bar{2}$0, respectively, with (a, c) bright field image and (b, d) weak beam dark field image, g/3g. These images are taken from same area with a mark for orientation.

More detailed comparison for defects formed in different directions or planes was performed in Fig. 3.4. The images of Fig. 3.4(a) to (c) are acquired from the same area with Fig. 3.4(a) in two-beam bright field condition (diffraction condition g=0004) and Fig. 3.4(b) and 4(c) in different weak-beam dark field conditions (g/3g, with g=0004 for (b) and g=10$\bar{1}$0 for (c)). The images of Fig. 3.4(d) and 4(e) are also taken from the same area in different weak-beam dark field conditions with g/3g, g=0004 for Fig. 3.4(d) and g=11$\bar{2}$0 for Fig.3.4(e).

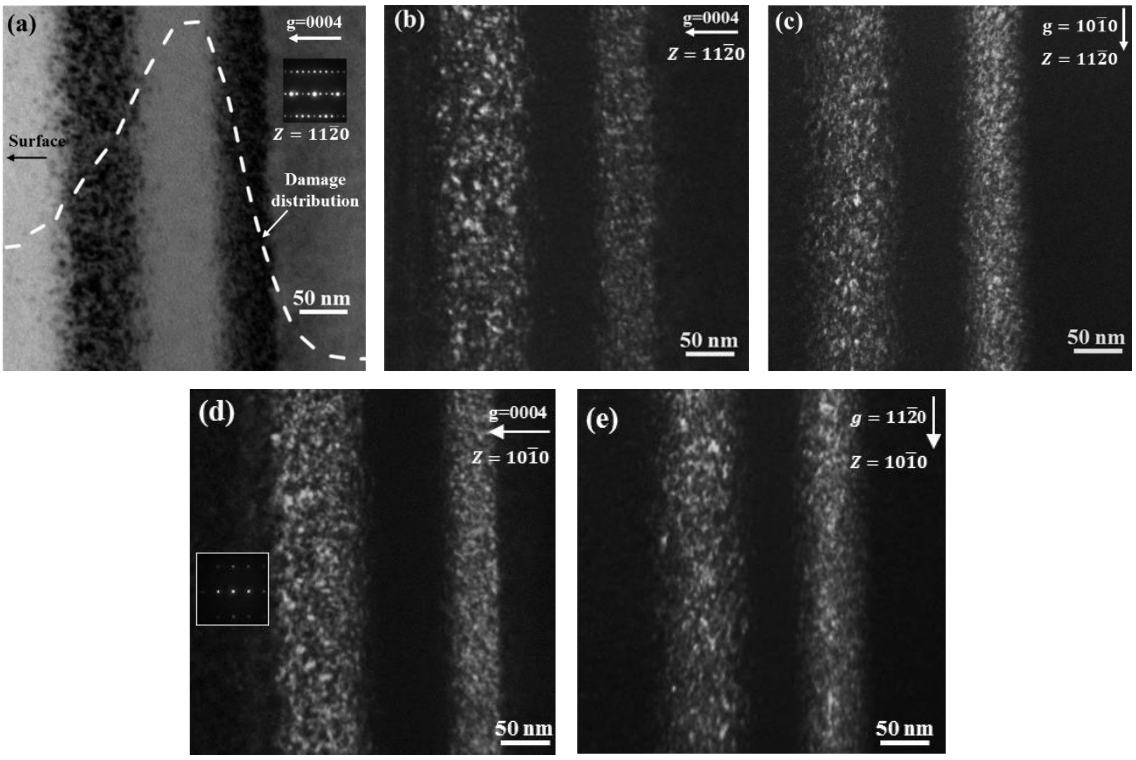

Fig. 3.4. TEM images of irradiated 4H-SiC taken with different observation condition. (a-c) are taken from same position under (a) two-beam bright field image and (b, c) g/3g weak-beam dark field image with g=0004 for (b) and g=$10\bar{1}0$ for (c). (d, e) are taken from same position using g/3g weak-beam dark field with g=0004 for (d) and g=$11\bar{2}0$ for (e).

Apparently, these images show the different distribution of BSDs in different diffraction conditions (g=0004, g= $10\bar{1}0$ and g= $11\bar{2}0$), suggesting an anisotropic defects distribution in selected-area ion irradiated 4H-SiC. The average size and number density of BSDs in B_1 region with different diffraction conditions were counted using weak-beam dark field image and summarized in Table 3.1. The BSDs appeared in [0004] have the highest number density following by [$11\bar{2}0$] and [$10\bar{1}0$], and the average size of

BSDs formed in [0004] is also quite larger than that in $[11\bar{2}0]$ and $[10\bar{1}0]$. In Fig. 3.5(a), the BSDs size distribution profiles for $[10\bar{1}0]$, $[11\bar{2}0]$ and [0004] show great difference. Although the peak of the profile of $[10\bar{1}0]$, $[11\bar{2}0]$ and [0004] are located around 4 nm, the number density is highest in [0004] direction for almost all of the sizes. In particular for the profile of the $[10\bar{1}0]$, a lack of relatively large BSDs (≥ 8 nm) are clearly observed compared with that in [0004] and $[11\bar{2}0]$. Therefore, the anisotropy of BSDs distribution in our samples can be summarized as that more and larger BSDs preferentially form in [0004] direction compared with that in $[10\bar{1}0]$ and $[11\bar{2}0]$ direction.

Table 3.1 Average size and number density of BSDs in different orientation

Conditions		$11\bar{2}0$	$10\bar{1}0$	0004
Selected-area ion irradiation	Average size (nm)	4.5	3.9	5.5
	Number density (10^{22} m^{-3})	1.6	1.1	2.9
Non-selected-area ion irradiation	Average size	4.7	5.0	4.7
	Number density (10^{22} m^{-3})	3.1	2.7	3.5
Annealing of the selected-area ion irradiation	Average size (nm)	6.0		6.3
	Number density (10^{22} m^{-3})	2.5		3.6
Electron irradiation	Average size (nm)		6.2	7.1
	Number density (10^{22} m^{-3})		0.72	1.1

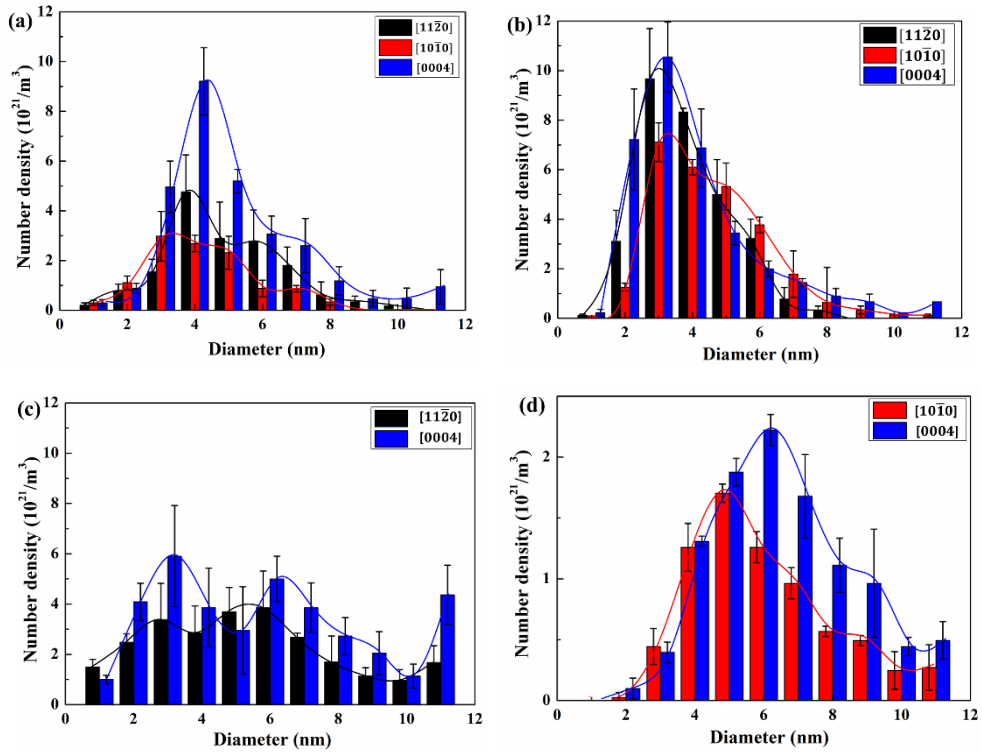

Fig. 3.5. Size distribution of BSDs in different orientation. (a) In selected-area ion irradiated sample. (b) In ion irradiated sample. (c) In selected-area ion irradiated sample after annealing. (d) In electron irradiated thin film TEM sample.

3.3.3 The nature of defects type

The nature of irradiated-induced defect clusters was explore using STEM techniques, including ABF-STEM and HAADF-STEM. The HAADF-STEM is a robust technique for identifying the position of atoms and atomic columns. When applied in a restricted zone-axis orientation, and the contrast in a HAADF image is strongly dependent on the atomic number (Z^n, where $n \approx 1.7$) and the sample thickness [27], which provides an approximate method for identifying atomic species. The ABF-STEM imaging technique is also able to directly detect the position of atoms [28], which provides a

complementary contrast to that of HAADF, as shown in Fig. 3.6. For instance, the Si atom columns correspond to the black spots and bright spots in ABF- and HAADF-STEM images, respectively.

Compared with the STEM-ABF image taken form unirradiated area (Fig. 3.6(a)), the defect-induced contrast variation in the STEM image can be clear observed even in the A layer both for the ABF and HAADF image, with some area becoming relatively blacker and brighter in ABF (Fig. 3.6(b)) and HAADF image (Fig. 3.6(c)), respectively. This should be attributed to the lattice disorder induced by defects [29]. The ABF- and HAADF-STEM images of Fig. 3.6(b) and (c) were taken from same region in A layer. The areas with contrast variation are circumscribed using dash line, and the location of these areas from ABF and HAADF image agree well. To clearly display the contrast variation, part of area from Fig. 3.6(b) and (c) was enlarged and shown in Fig. 3.6(e) and (f), respectively, and the image of Fig. 3.6(d) (enlarging from Fig. 3.6(a)) is given as a comparison standard.

Using Gatan Digital Micrograph, the measured average spacing between lattice plane of [0004] in the unirradiated area (without contrast variation) is about 2.47 Å as shown in Fig. 3.6 (d), almost same as the previous reported result of 2.51 Å using XRD [30]. However, in the area with contrast change, disorder of lattice can be observed in Fig. 3.6 (e), and the lattice plane spacing was enlarged to about 2.72 Å in average. The expansion of lattice plane in this contrast changed area suggests that the lattice disorder in this area should be attributed to the tiny interstitial type cluster formed in these areas [31]. Besides, an area with contrast variation in the HAADF image that

marked using solid line in (Fig. 3.6(c)) was enlarged and displayed in Fig. 3.6(f). The difference in image contrast was corroborated in the image of intensity profile and was displayed beneath each corresponding column, which is obtained using Gatan DigitalMicrograph software across the column along the arrow direction. Intensity of the center columns of this selected area increased. Considering there is no heavier atom doped into the materials, therefore, the increased contrast should arise from the interstitial type clusters [32-33], with size about smaller than 1 nm. Based on the results of ABF and HAADF, most tiny defect clusters formed in A layer should be interstitial type.

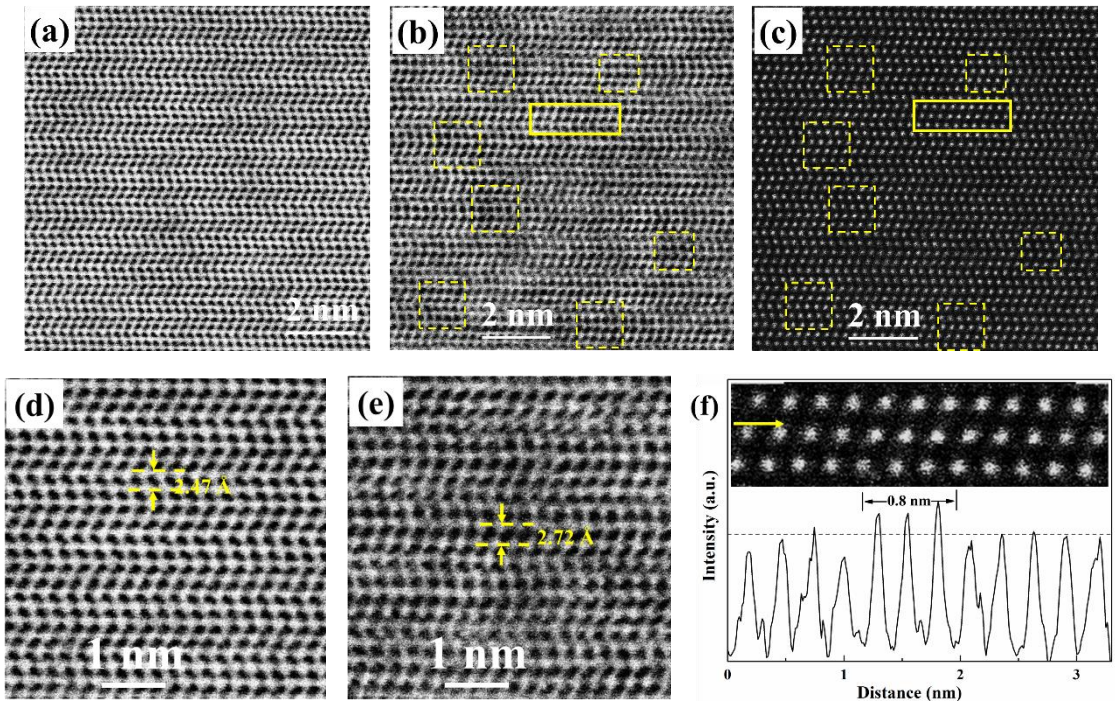

Fig. 3.6. STEM image of taken from unirradiated area and A layer along $[11\bar{2}0]$ zone axis. (a) the ABF image from unirradiated area. (b, c) are taken from same region in A layer with (a) ABF image and (b) HAADF image. (d) enlarged image of the area in Fig.3.6(a). (e) enlarged image of the area in Fig.3.6(b). (f) enlarge image of the area

marked by solid line in Fig.3.6(c), and the intensity of each atom columns along the arrow direction. The contrast changed areas are marked by dash line and solid line.

Some larger contrast-changed areas were observed in the B_1 layer and around the amorphous/crystal interface as shown in Fig. 3.7 circumscribed by dash line, indicating some larger defect clusters. The average size of these clusters shown in Fig. 3.7 is about 5 nm, agreeing well with the size of BSDs summarized in Table 3.1. Hence, these defect clusters should correspond to the BSDs as shown in Fig. 3.2(b) and (c). The lattice plane spacing expansion were confirmed in these contrast-changed areas. Besides, in some contrast-changed areas, such as Fig. 3.7(c) which is enlarged from the area of Fig. 3.7(b) circumscribed by red solid line, some extra planes of atom columns were observed, which is confirmed by the image of inverse fast Fourier transform of this area (Fig. 3.7(d)). These extra planes also provide some insight that most defects formed in the contrast-changed areas should be interstitial type. These above results suggest that the BSDs formed in our samples should mainly be interstitial type clusters, which is agreed well with the mobility of interstitials and vacancies in SiC. M. Bockstedte et al. have reported that the migration energies of vacancies are 3.2-3.6 eV and 3.5-5.2 eV in Si and C [34], respectively, while the migration energies of interstitials are found to be 1.53 eV in Si and 0.74 eV in C [35], respectively. The Si vacancies in SiC becomes sufficiently mobile at 800-900 °C [36], and C vacancy may need a higher temperature. As our samples were irradiated at room temperature, interstitials are relatively easier to move and combine into

clusters. Besides, BSDs were also reported as interstitial type clusters in some other studies [7, 8].

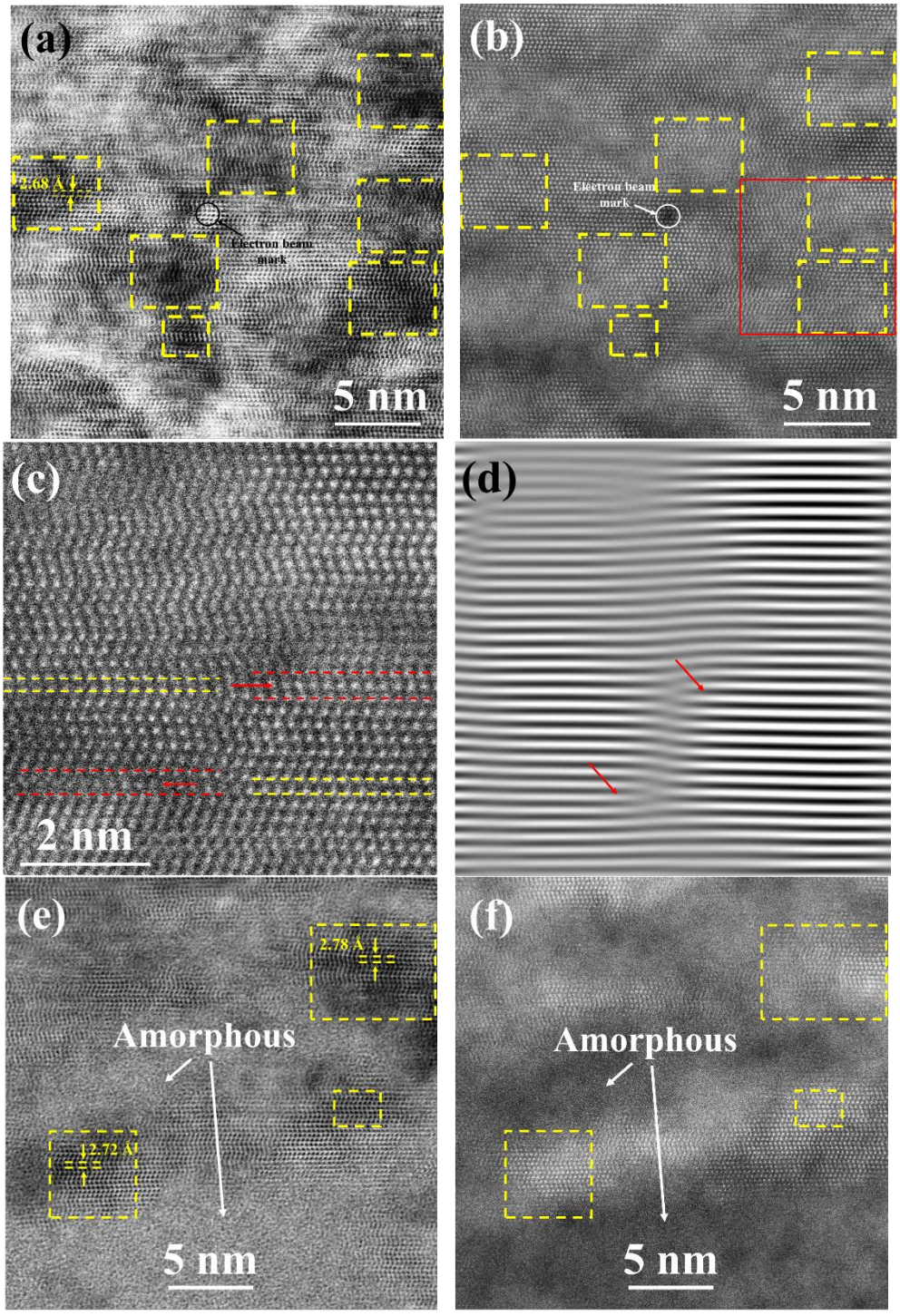

Fig. 3.7. STEM image taken from B_1 layer and around the amorphous/crystal interface along $[11\bar{2}0]$ zone axis. (a, b) are taken from same region in B_1 layer with (a) ABF

image and (b) HAADF image. (c) is enlarged from the area in Fig. 3.7(b) circumscribed by red solid line. (d) is the image of inverse fast Fourier transform of Fig. (c). (e, f) are taken from same region around the amorphous/crystal interface with (e) ABF image and (f) HAADF image. In (a) and (b), a mark is made by electron beam to confirm the position of each image.

3.4 Discussion

3.4.1 Anisotropic defect distribution

The anisotropic BSDs distribution was detected by conventional TEM technique, and these defect clusters should be interstitial type in view of the STEM results and defect mobility in SiC. As BSDs are the accumulation result of point defects, more and larger BSDs formed in [0004] direction implies that more interstitial type defects should preferentially redistribute into [0004] direction in our samples compared with other two directions. The defect distribution is correlated with the strain/swelling in the sample. In general, interstitial type defects cause the expansion of lattice around them. The detected defects distribution implies a higher tensile strain in [0004] direction than that in other two directions. This deduction agrees well with the anisotropic strain condition of our samples with tensile strain in [0004] direction and compressive strain in $[10\bar{1}0]$ and $[11\bar{2}0]$ direction [20]. Even though with relative lower number density, the BSDs in $[10\bar{1}0]$ and $[11\bar{2}0]$ direction are still expected to expand the lattice of each direction. However, the compressive strain is introduced into these two directions. This implies that more defects with negative volume effect, such as vacancy and/or carbon antisite defects (carbon atom occupying the Si-vacancy site,

C_{Si}) [1, 14], than interstitial type defects should be introduced in these two directions. Fig. 3.8(a) and (b) display the STEM-EELS core-loss spectra of the silicon $L_{2,3}$-edge and carbon K-edge, respectively, acquired from different damage layers. For identifying, the reference spectra of single crystal silicon and amorphous carbon were also shown in Fig. 3.8. It is shown that the peaks excited from the bonding structure of SiC, in term of Si $L_{2,3}$-edge peak at ~103 eV and 1s→σ* transition peak of carbon K edge at ~290 eV, gradually broaden with increasing damage. The 1s→ π* peak at about 283 eV and 1s→σ* peak at about 290 eV correspond to the presence of sp^2 and sp^3 bonding, respectively. In the spectra acquired from B_1 and C layer, the 1s→ π* shoulder peak at about 283 eV was observed. These results are the evidence of the irradiation-induced bonding configuration shifting from sp^3 to sp^2 [1,37], suggesting the presence of C_{Si} especially in the relatively high damage area (B_1 and C layer). The detected C-C bond in our previous Raman results also implies the occurrence of this shifting of the bonding configuration [20]. Considering the negative volume effect of C_{Si} [1, 14], the occurrence of C_{Si} may contribute to the compressive strain in $[10\bar{1}0]$ and $[11\bar{2}0]$ direction.

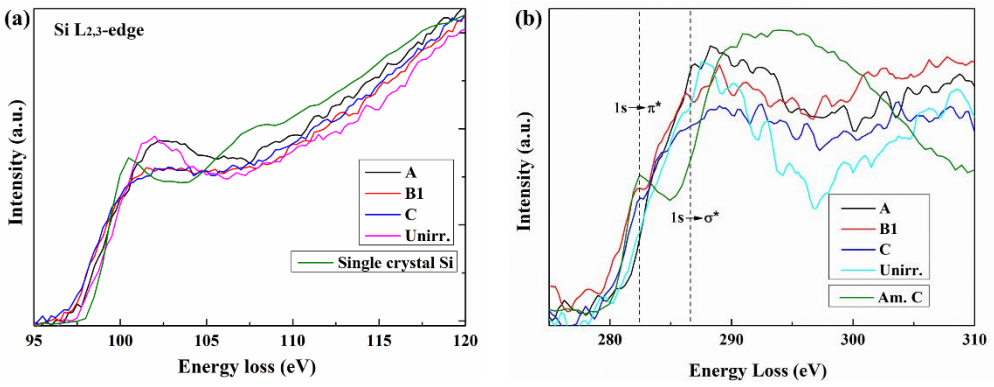

Fig. 3.8 The irradiation-induced change of EELS core-loss spectra. (a) Si $L_{2,3}$-edge

spectra. (b) carbon K-edge spectra. The inset letters correspond to the layers marked in Fig.3.1(a). The reference spectra of single crystal silicon and amorphous carbon acquired from Gatan EELS website (https://eels.info/atlas/carbon).

3.4.2 The potential mechanism for the anisotropic defect distribution

The different number density and size distribution of BSDs (shown in Table 3.1 and Fig.3.5(a)) indicate the various nucleation and growth condition among different directions. Obviously, BSDs in [0004] direction have more nucleation sites and higher growth rate. Defects formation and grow in SiC during ion irradiation are mainly arisen from the irradiation-induced point defects and then their diffusion and combination. Ion irradiation usually introduce the nearly same number of interstitials and vacancies (Frenkel pairs) in SiC. The anisotropic defects distribution in our sample might be mainly attributed to the different mobility of interstitials and vacancies, which usually control the defect type and their distribution. As the sample was irradiated at room temperature, where interstitial points defects are mobile while vacancies are not. It is likely that some of interstitials might redistribute from $[10\bar{1}0]$ and $[11\bar{2}0]$ into [0001] to reduce the internal energy due to the habit plane for (0001), resulting in the larger and more interstitial type BSDs in the interplane of [0004].

It has been reported that anisotropic swelling leads to significant stresses [10,12]. Using EBSD, the stress distributions in irradiated and unirradiated area were measured and shown in Fig. 3.9 with (b), (c) and (d) corresponding to stress in X ($[11\bar{2}0]$), Y ($[10\bar{1}0]$) and Z ([0001]), respectively. It is clear

that due to the restriction of swelling, great compressive stress was introduced into both X and Y direction with average about -0.94 GPa and -1.15 GPa, respectively, but little stress in Z direction because of the relaxation of swelling. Moreover, the stress distribution in the other sample with quite lower fluence of 1×10^{15} cm^{-2} was also measured by EBSD as shown in Fig. 3.10. Anisotropic stress distribution was also distinct in this sample with relatively large compressive stress in X (-0.23 GPa) and Y (-0.36 GPa) but little in Z. This indicates that the great compressive stress in the lateral direction begins to accumulate even at the beginning of irradiation. S. Kondo reported that compressive stress likely inhibits the interstitials type loop nucleation in planes perpendicular to the stress axis [38]. It also has been reported that external stress would cause an anisotropic Frank loop development in ion irradiated SiC [39]. In Table 3.1 and Fig.3.5(a), the BSDs in lateral direction show a lower number density and smaller size. It is likely that the lateral compressive stress introduced during irradiation inhibits the interstitial type defects nucleation and growth. This anisotropy of defects distribution in selected-area He^{+} ion irradiated 4H-SiC might be mainly attributed to the different stress condition among different directions.

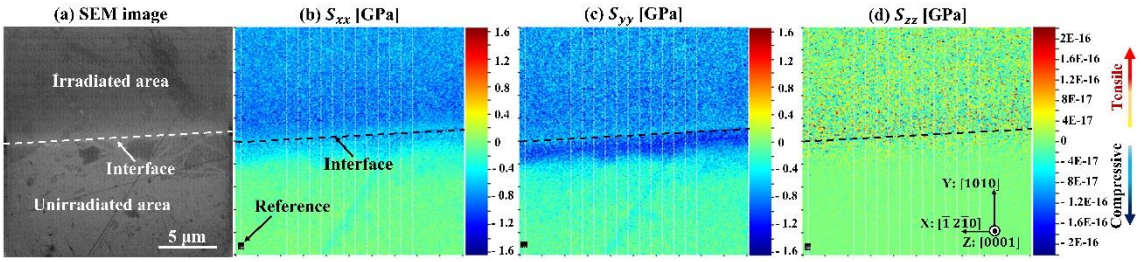

Fig. 3.9. Stress distribution in the selected-area He^{+} ion irradiated 4H-SiC with fluence of 5×10^{16} cm^{-2}. (a) SEM image. (b)-(d) corresponding to stress composition in X, Y and Z

direction.

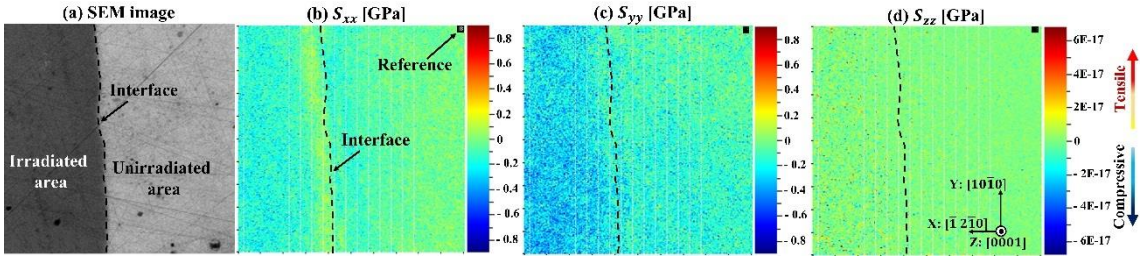

Fig. 3.10. Stress distribution in the selected-area He^+ ion irradiated 4H-SiC with fluence of 1×10^{15} cm^{-2}. (a) SEM image. (b)-(d) corresponding to stress composition in X, Y and Z direction.

3.4.3 Defects distribution in non-selected-area He^+ ion irradiated 4H-SiC

For comparison, a non-selected-area He^+ ion irradiated 4H-SiC was made with the same fluence of 5×10^{16} cm^{-2}. The defects distribution in this sample was observed as shown in Fig. 3.11. The observed difference among different directions in this sample seems not as large as that in the selected-area irradiated 4H-SiC. The calculated average size and number density of BSDs were summarized in Table 3.1. The BSDs in different directions are quite similar in the average size with a higher number density in [0004] direction. The defect distribution is still anisotropic in this sample. However, its anisotropy is quite smaller than that in the selected-area irradiated samples in term of the average size and number density of BSDs. This is confirmed by the quite similar defect size distribution among different direction in Fig. 3.5(b) as compared with that in Fig. 3.5(a). The great lower anisotropy of defect distribution in the non-selected-area He+ ion irradiated 4H-SiC indicates the restraining effects of the compressive stress on the formation of

interstitial type defects, which is introduced in the selected-area irradiated samples (Fig. 3.9).

In this non-selected-area irradiated sample, the anisotropic defect distribution is still observed. A previous study has reported that compressive stress would also introduce into the lateral direction in ion irradiated SiC, which is attributed to the constraint against lateral expansion due to the shallow thickness of the irradiated layer as compared to the sample thickness, in contrast to the free expansion allowed along the surface normal [38]. Hence, the compressive stress in the lateral direction may also be introduced in the non-selected-area ion irradiated sample, resulting in the anisotropic defect distribution.

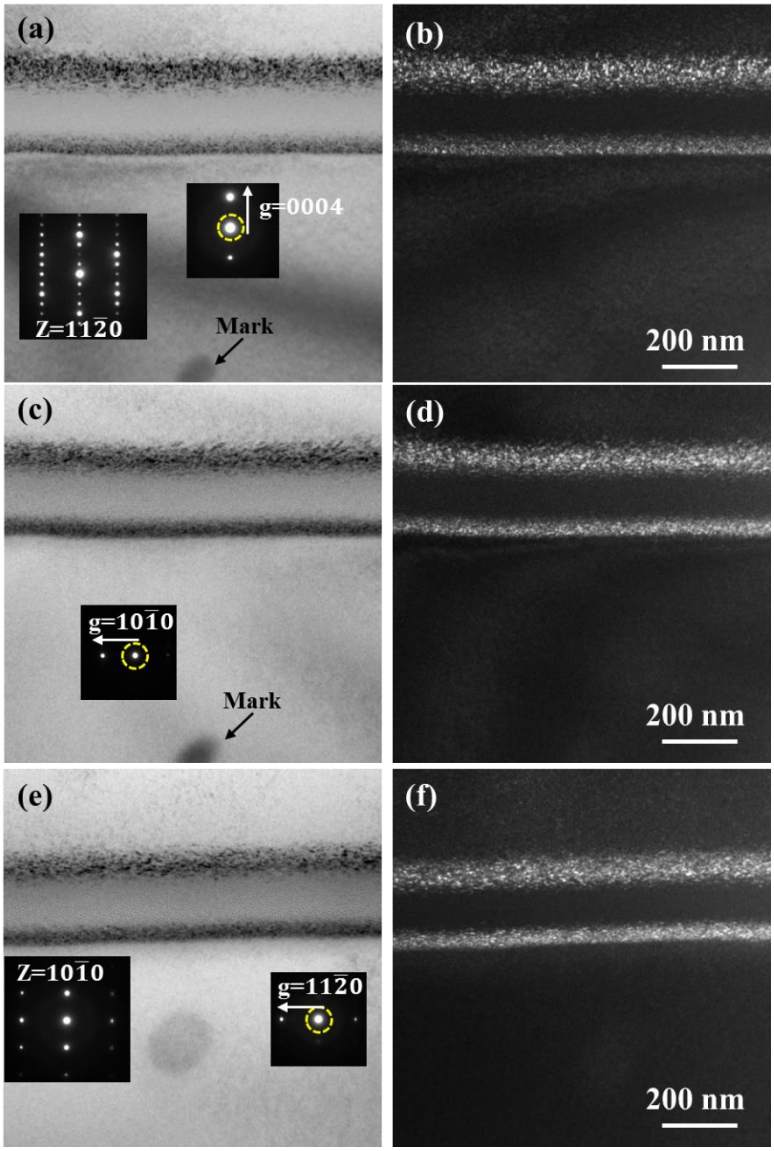

Fig. 3.11 TEM images of BSDs in non-selected-area He^+ ion irradiated 4H-SiC with fluence of 5×10^{16} cm^{-2}. (a), (c) and (e) are two beam bright field images with g=0004, $10\bar{1}0$ and $11\bar{2}0$, respectively, and (b), (d) and (f) are their corresponding weak beam dark field images with g/3g. (a-d) are taken from the same area, and (e, f) are from another area.

3.4.4 Annealing effects on the anisotropy of defect distribution

To relax the stress introduced in the selected-area He^+ ion irradiated

sample, TEM foil samples made by FIB were annealed at 600 °C for 30 mins in HVEM. After annealing, the defect distribution was shown in Fig. 3.12, which shows a little extension of BSDs layer, suggesting more BSDs might be appeared. The observed BSDs in [0004] diffraction condition is still more than that in $[11\bar{2}0]$. The summarized results of average size and number density of BSDs after annealing were shown in Table 3.1. The results show an increase both in the average size and number density in both directions after annealing, which agrees well with the increased amounts of relatively large BSDs (such as >7 nm) in the size distribution of BSDs (Fig. 3.5(c)). This should be attributed to the increasing mobility of defects upon annealing, which enhances the growth and coalescence of defects.

It is obvious that after annealing the defect distribution is still anisotropic. However, comparing the average size and number density in [0004] and $[11\bar{2}0]$ before and after annealing, it is found that the difference between these two directions decreased upon annealing, with the ratio of average size decreasing from 1.2 (5.5/4.5 in Table 3.1) to 1.05 (6.3/6.0) and the ratio of number density decreasing from 1.8 (2.9/1.6) to 1.4 (3.6/2.5). The anisotropy of defect distribution decreased after annealing at 600 °C. Upon annealing, the strain/swelling would relax as well as the internal stress, and a new stable configuration of defects might be formed in order to decrease the free energy of system. Therefore, this decreasing anisotropy upon annealing may be attributed to the reconfiguration of defects due to the relaxation of stress, which suggests that the compressive stress introduced during irradiation enhances the anisotropy of defect distribution in the selected-area ion

irradiated sample.

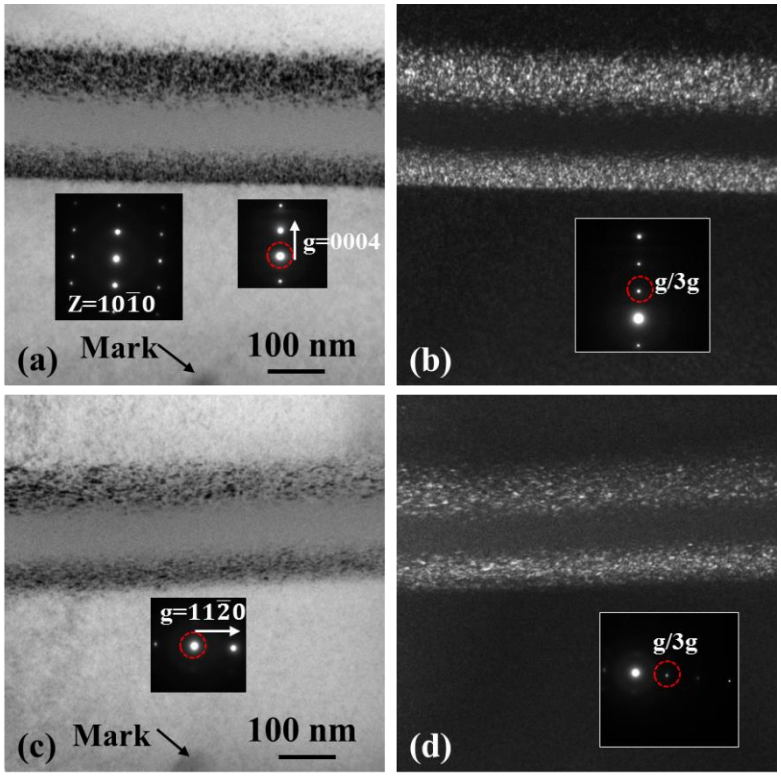

Fig. 3.12. TEM image of BSDs distribution after annealing at 600 °C. (a, b) and (c, d) at g=0004 and g=11$\bar{2}$0, respectively, with (a, c) bright field image and (b, d) weak beam dark field image, g/3g. These images are taken from same area with a mark for orientation.

3.4.5 Defect distribution in electron irradiated thin film 4H-SiC sample

It was reported that compressive stress might also be possible to be introduced into the lateral direction even in the non-selected-area ion irradiated bulk samples due to the constraint against lateral expansion [38]. For a comparison, the electron irradiation was performed on a TEM foil sample of 4H-SiC (made by FIB) at room temperature. Before irradiation, the samples were annealed at 600 °C for 30 min to remove the potential internal stress. During irradiation, the electron beam parallels to the [11$\bar{2}$0]

zone axis. Hence, compared with the He^+ ion irradiated bulk sample, there are two main differences in term of the stress condition that should be point out in electron irradiated sample. One is that the lateral stress in electron irradiated area should be relative lower due to the thinner thickness of electron irradiated sample, though electron irradiation is also a kind of selected-area irradiation. The other is that the [0004] and $[10\bar{1}0]$ should have a similar stress, because both of them belong to the lateral direction as electron beam along $[11\bar{2}0]$ direction. Therefore, the great different stress state between [0004] and $[10\bar{1}0]$ in ion irradiated sample could be neglected in this electron irradiated sample.

The defects distribution in the center of electron irradiation area were shown in Fig. 3.13, and the counted average size and number density of BSDs are summarized in Table 3.1. The BSDs formed under electron irradiation is larger in average size and lower in number density than that under ion irradiation. Deducing from the different average size and number density between $[10\bar{1}0]$ and [0004] direction, or from the BSDs size distribution shown in Fig.3.5(d), the defect distribution in electron irradiated 4H-SiC is anisotropic. The ratio of between $[10\bar{1}0]$ and [0004] direction in the average size and number density is 1.15 (7.1/6.2) and 1.52 (1.1/0.72) in electron irradiated sample. These ratios are quite smaller than that of 1.41 (5.5/3.9) and 2.64 (2.9/1.1) in selected-area He^+ ion irradiated sample, but similar to the 0.94 (4.7/5.0) and 1.30 (3.5/2.7) in the non-selected-area He+ ion irradiated sample. Therefore, it seems clearly that the anisotropy of defects distribution in the selected-area He^+ ion irradiated sample was

enhanced, which should be attributed to the great compressive stress introduced in lateral direction during irradiation. Anisotropic defect distribution was also observed in the electron irradiated foil sample and non-selected-area ion irradiated bulk sample. However, , the condition in these two samples should be different. Hence, the anisotropic defect distribution in the non-selected-area ion irradiated sample and electron irradiated sample might not only be attributed to the stress, and some other potential mechanism might exist.

It should be pointed out that the different irradiation conditions between ion irradiation and electron irradiation, including different dose rate, different irradiation particle energy and cascade effect, might contribute to the different defect evolution. In particle, for the thin sample used in electron irradiation, interstitial and vacancy atoms might annihilate in the surface, which would also great change the defect distribution in the sample. However, the above cases should perform a similar effect on the defect distribution for [0004] and $[10\bar{1}0]$, and they might not greatly change the anisotropy of defects distribution between [0004] and $[10\bar{1}0]$. Hence, the great difference in anisotropy of defect distribution between selected-area ion irradiation and electron irradiation might be mainly attributed to the compressive stress introducing during ion irradiation.

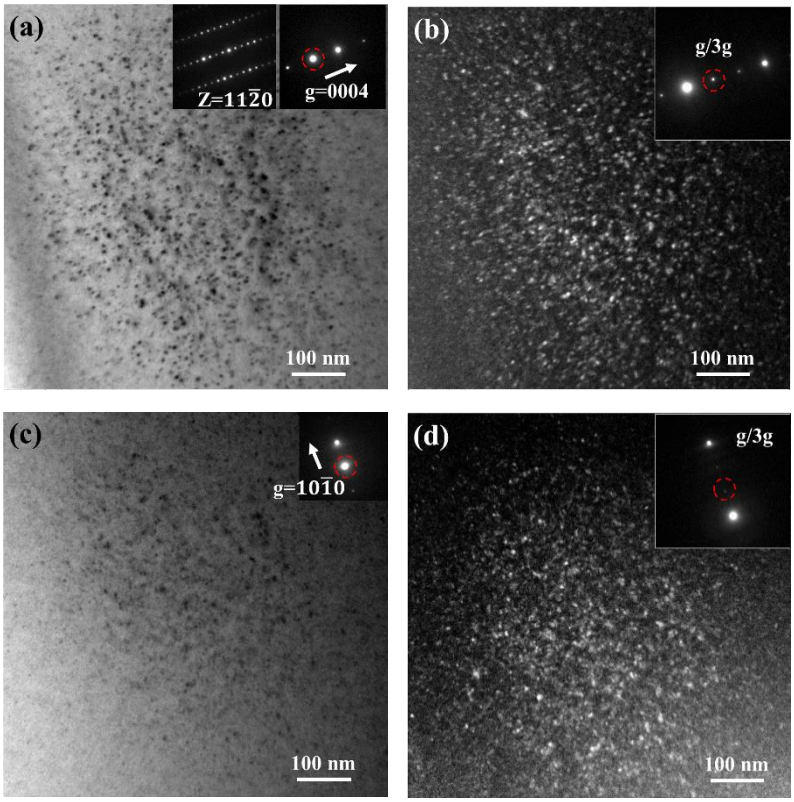

Fig. 3.13. TEM images of BSDs distribution in the center of electron irradiation area at room temperature. (a, b) and (c, d) at g=0004 and g=$10\bar{1}0$, respectively, with (a, c) bright field image and (b, d) weak beam dark field image, g/3g. These images are taken from same area.

3.5 Summary

Using TEM techniques, the defects distribution in 4H-SiC with irradiation-induced anisotropic swelling was explored, and an anisotropy of defects distribution was found that interstitials type defects preferentially redistribute into the free expanding direction ([0004] direction) with more negative volume defects locating in the constraint swelling direction ($[10\bar{1}0]$ and $[11\bar{2}0]$ direction). This anisotropy of defect distribution is quite larger than that in non-selected-area He^+ ion irradiated 4H-SiC, and it decreased

upon annealing at 600 °C. It was found that great compressive stress was introduced in the lateral direction ($[10\bar{1}0]$ and $[11\bar{2}0]$) but little in the surface normal direction ([0004]) in the selected-area He^+ ion irradiated 4H-SiC due to the constraint against lateral expansion, and these compressive stresses were introduced at the beginning of ion irradiation. The compressive stress introduced during irradiation is supposed to inhibit the interstitials types defects formation, enhancing the anisotropic defect distribution in the selected-are ion irradiated 4H-SiC.

Chapter 4 Electron energy-loss spectroscopic evaluation of depth-dependent swelling of He^+ ion-irradiated 4H-SiC correlated with defect type

4.1 Introduction

The irradiation-induced swelling in He^+ ion irradiated 4H-SiC was evaluated in chapter 2, and irradiation-induced defects were also investigated in chapter 3. It is reported that irradiation-induced defects play an important role in the swelling and strain the accumulation. Up to now, amounts of researches have been performed to investigate the irradiation-induced swelling in SiC [1-8], including neutron irradiation [7-9] and ion implantation [10-12]. However, knowledge of specific defect contribution to swelling is still limited. Furthermore, when low-mass particles, such as H^+ or He^+, are implanted or produced into the materials, the swelling mechanism would become more complex because of the formed low-mass particle bubbles [11, 13]. Therefore, it is necessary to clarify the effect of each defect type on swelling.

Generally, the swelling is typically evaluated via a dimensional change using X-ray diffraction [8] or atomic force microscopy [1], where the swelling is usually ascribed to the summation result of various defect types, including point defects, defect clusters, and various bubbles. However, it is found to be difficult for clarifying the contribution of each defect type to the swelling [14-16]. A local swelling detection method may be helpful to clarify the contribution of each type defect to swelling.

In this chapter, the defect distribution in the He^+ ion irradiated 4H-SiC was determined using various transmission electron microscopy (TEM) techniques, and STEM-EELS technique was used to separately evaluate the local swelling in different regions. The contribution of different type defect to the swelling was clarified, which would be helpful for the prediction of SiC swelling in application.

4.2 Experimental procedure

4.2.1 Irradiation experiment and microstructural characterization

In chapter 2 and 3, two kind samples, the He^+ ion irradiated 4H-SiC (0001) substrates with a fluence of 1×10^{15}, 5×10^{16} cm^{-2}, have been made. Herein, another He^+ ion irradiated sample with fluence of 1×10^{17} cm^{-2} was made at room temperature. Here, the fluence of 1×10^{15}, 5×10^{16} and 1×10^{17} cm^{-2} are termed as low fluence, medium fluence and high fluence, respectively. The penetration profile of He^+ ions into SiC was calculated as described in chapter 3.

After irradiation, TEM foils were made by FIB system (JEOL, JEM-90320FIB) as describe in chapter 3. The internal microstructure was characterized by TEM (JEOL, JEM-2000FX and JEM-2010F), which was operated at 200 kV. The EELS studies were performed by Cs-corrected STEM (FEI, Titan G2 60-300) at 300 kV. The EELS spectra were obtained via HAADF-STEM mode using the point-to-point detection method from different damaged regions with a beam size ~0.2 nm. Considering the curvature effect of surface and the possible damage introduced into the

surface during the FIB processing, the acquisition of EELS spectra began from a position about 50 nm beneath the surface. Three different positions at the same depth were detected to acquire statistical results. After calibrating the zero-loss peak of each EELS spectrum, the peak shifts of the plasmon-loss peak were obtained. The energy resolution, measured as the full width at half maximum of the zero-loss peak, was 0.9 eV.

In addition, Raman backscattering was also carried out at room temperature using a Raman microscope. The parameters of Raman scattering were same as that describe in Chapter 2.

4.2.1 Estimation of swelling using EELS

The plasmon-loss peak depends upon the density of the free electrons in the material. Specifically, when an electron beam generates a plasmon with frequency ω_p, the plasmon energy, E_p, is given by [17]

$$E_p = \frac{h}{2\pi}\omega_p = \frac{h}{2\pi}\left(\frac{ne^2}{\epsilon_0 m}\right)^{\frac{1}{2}}, \tag{4-1}$$

where E_p is the energy lost by the electron beam; h is Planck's constant; n is the free electron density; e and m are the electron charge and effective mass, respectively; and ϵ_0 is the permittivity of free space.

According to the Jellium Model, n is proportional to the bulk density of the material [17]. Assuming that the observed decrease of the volume plasmon energy is solely attributed to the specimen volume swelling, the relation between volume swelling and plasmon-loss peak shift can be given as [18]

$$\Delta V/V_0 = [V - V_0]/V_0 = [E_{p0}/E_p]^2 - 1 \tag{4-2}$$

where V_0 and V are the material volumes before and after irradiation,

respectively; and E_{p0} and E_p are the plasmon-loss peak positions of unirradiated and irradiated regions, respectively.

4.3 Results

4.3.1 Defect distribution in irradiated 4H-SiC

After irradiation, the microstructure in the ion-irradiated samples with varying ion fluence were characterized by TEM as shown in Fig. 4.1. As described in Chapter 3, three types of regions with distinct bright-field image contrast (i.e., gray, black and white) are discernible in the sample irradiated with a fluence of 5×10^{16} cm^{-2} (medium fluence). Here, they are also denoted as A-, B- and C-layers, and the B-layer region is further divided into two layers designated as the B_1- and B_2-layers. As identified in chapter 3, the B-layer contains lot of BSDs, and C-layer has become amorphous, where the amorphous layer encompasses a depth range of 380 to 470 nm beneath the surface, with an amorphous layer thickness of 90 nm.

For the sample with high fluence (1×10^{17} cm^{-2}), an enlarger amorphous layer was observed from 250 nm beneath the surface to a depth of 700 nm with a thickness of about 450 nm (Fig. 4.1(c) and (d)), which should be attributed to the greater damage introduced into the material by higher irradiation fluence. Moreover, the damaged layer thickness is greater than that given by the SRIM calculation as shown in Fig. 4.1(c). This discrepancy between simulation and experiment results might be ascribed to the the concurrent volume expansion and decreasing density during ion irradiation, which is not considered in the SRIM simulation [20]. In addition, the near-

surface region exhibiting a gray contrast and the bottom BSD region become very narrow in this sample. These different damage regions in this sample are also denoted as A-, B- and C-layers based on their TEM image contrast. It should be pointed out that the C-layer region is further separated into the C_1- and C_2-layers depending upon whether or not the layer contains helium bubbles, which will be shown and discussed later in the later discussion part.

At the low fluence (1×10^{15} cm^{-2}) as shown in Fig. 4.1(e) and (f)), the TEM images also displays varying contrast depended on the depth due to the different level of damage. However, the contrast variation among different damage layers is relatively weaker compared with those observed in the above two samples (Fig. 4.1(a) and (c)) owing to its lower irradiation fluence. Besides, no amorphous region or BSDs formed under this fluence. However, a black contrast appears at the maximum damage region in the two-beam bright-field TEM image (Fig. 4.1(e)), indicating some microstructure variation in this region. For convenient comparison of the above results, we also denote the damage regions in this sample as A-, B_1-, B_2- and C-layers based on the TEM bright image contrast, despite the different damage state between this and the other two irradiation fluence samples.

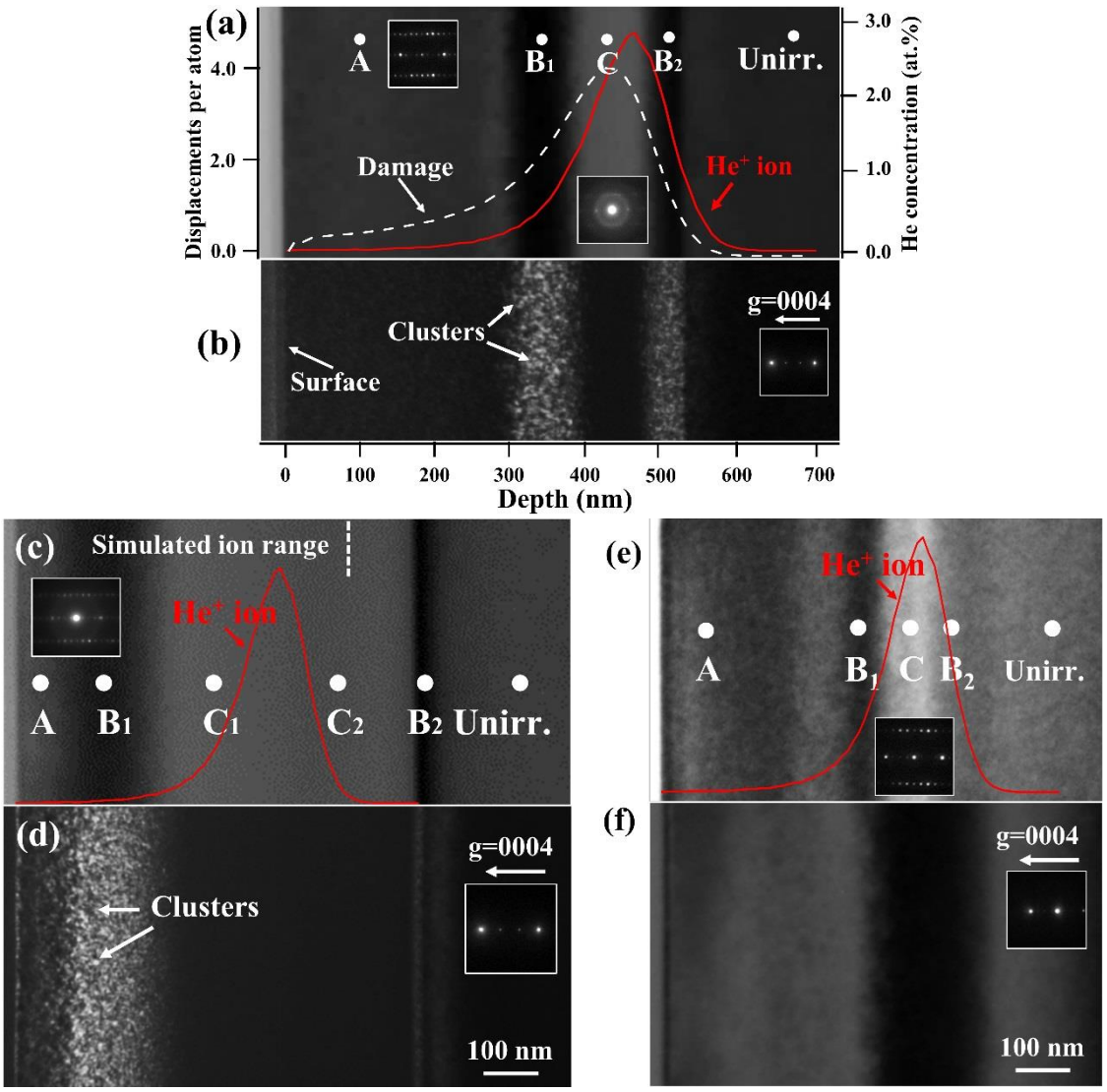

Fig. 4.1. Cross-section image of He^+ ion irradiated 4H-SiC with different fluences. (a, b) At medium fluence. (a) along the $[11\bar{2}0]$ zone combined with the displacement damage (white dashed line) and the He^+ ion concentration (red solid line) profile. (b) Weak-beam dark-field TEM image under the $g/3g$, g=0004 condition. (c, d) At high fluence. (c) along the $[11\bar{2}0]$ zone and (d) weak-beam dark-field TEM image under the $g/3g$, g=0004 condition. (e, f) At low fluence. (e) near the $[11\bar{2}0]$ zone and (f) two-beam bright-field TEM image under the g=0004 condition. The inset images in (a), (c) and (e) are the selected-area diffraction pattern of the constituent areas, and the inset images in (b), (d) and (f) correspond to the diffraction condition when taking each image [21].

4.3.2 Evaluation of local swelling

The low-loss EELS spectra acquired from different damage areas, as marked the A-, B_1-, B_2-, C-, C_1-, and C_2-layers in Fig. 4.1, are shown in Fig. 4.2. The acquired peak position of the plasmon-loss peak in the unirradiated region located at 22.2 eV, which agrees well with previous reported results [18, 22]. It is found that this plasmon-loss peak would shift lower energy in the damaged regions (A-, B-, and C-levels) for samples irradiated with medium and high fluences, moreover, the shift increases with increasing damage level. The red shift of the plasmon-loss peak is also observed in the sample with the lowest fluence, as shown in Fig. 4.2(c), however, with a smaller magnitude in shift than the other two samples. In addition, the plasmon-loss peak shift of the C-level spectrum is smaller than that of the B_1-level spectrum in the low-fluence sample (Fig. 4.2(c)), where the former showed the largest peak shift in the samples with higher fluences, as shown in Figs. 2(a) and 2(b). This implies that some different microstructure may be introduced into the maximum damage region in the low-fluence sample.

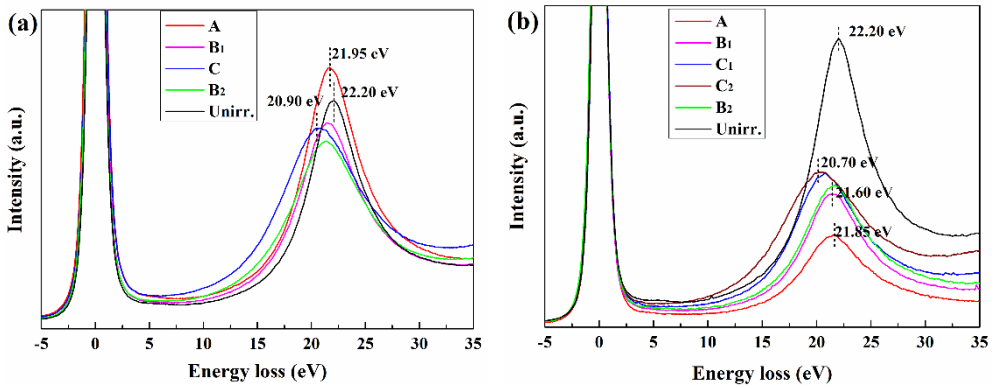

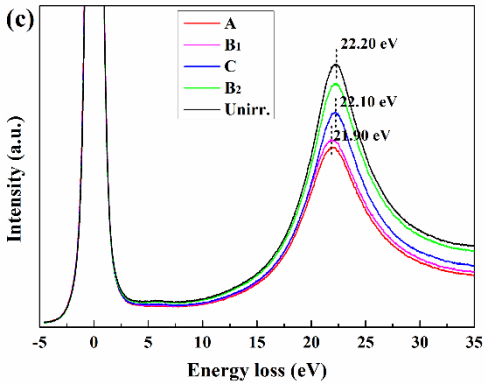

Fig. 4.2. Plasmon-loss EELS spectra at different damage regions in samples irradiated with fluences of (a) 5×10^{16}, (b) 1×10^{17}, and (c) 1×10^{15} cm^{-2}. The spectra in (a–c) correspond to the regions marked in Fig. 4.1(a), (c), (e), respectively [21].

According to the peak shift of the volume plasmon-loss peak, the local volume swelling at the different damage regions is evaluated as shown in Fig. 4.3. For better understanding, the calculated dose (dpa) profiles were also provided into these figures. For the sample with highest fluence, the calculated dose using SRIM is deviated from experimental one because of the expansion of amorphous region (Fig. 4.1(c)). However, the simulated results at the first half damage region (about prior to 350 nm) should be in good agreement with the experimental result, because this region still maintains some extent crystallinity. Therefore, only the first half of dose (dpa) profile was added into the Fig. 4.3(b). Because of varying damage in depth, the defects in the ion-irradiated SiC change depending on the depth, which further results in varying swelling as a function of depth. These results show a gradual increase of swelling from 1.9% to 13.3% with increasing depth from the A- to C-layer, respectively, followed by a sharp decrease in the B_2-layer, which matches well with the shape of dose profile (Fig. 4.3(a)). The

swelling profile in depth changes significantly for the sample with different irradiation fluences, both for the swelling value and trend, as displayed in Fig. 4.3(b) and (c). The swelling in the highest-fluence sample exhibits a sharp increase in depth (i.e., from 3.2% to 15.3%), which should be ascribed to the sharp increase of irradiation dose (Fig. 4.3(b)). The sample irradiated with lowest fluence, however, showed a swelling that remained almost constant in the near-surface region, then gradually decreasing in the C- and B_2-layers of the sample. The depth dependence of swelling under varying irradiation fluence will be discussed in terms of irradiation dose and microstructural variation in later sections.

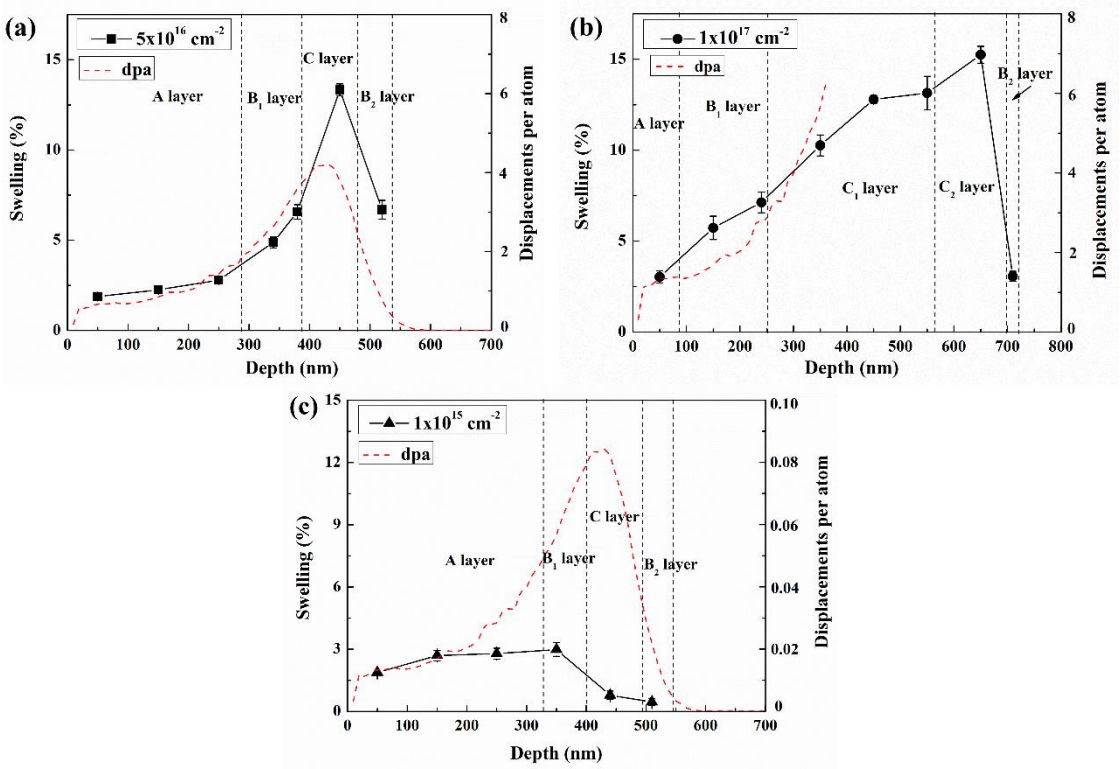

Fig. 4.3. Swelling Profile as a function of depth combined with the estimated dose profile in selected-area He^+ ion-irradiated 4H-SiC irradiated with medium fluence (a) high fluence (b) and low fluence (c). Due to the expansion of amorphous region at this fluence,

only the first half of dose (dpa) profile was added into the Fig. 4.3(b) [21].

4.4 Discussion

4.4.1 Swelling saturation in the near-surface region

As shown in Fig. 4.1(a) and (b), no obvious defects are observed in the near-surface layer (i.e., A-layer) using TEM, however, the volume of this layer expands by 1.9%–2.8% (Fig. 4.3(a)). In the high-resolution TEM image, the microstructure in the A-layer is observed to maintain a good crystallinity without obvious defects (Fig. 4.4(a)), while the defect contrast indicative of BSDs and amorphization is distinct around the B_1/C-layer interface. Using HR-STEM, some small contrast varying areas were observed both in ABF- and HAADF-STEM images shown in Fig. 4.5. As discussed in last chapter (Fig. 3.6), these contrast varying areas should be attributed to the presence of tiny clusters. Hence, the volume swelling in the near-surface layer should be ascribed to the formation of tiny or invisible defects to conventional TEM, such as point defects or tiny defect clusters. In the lowest-fluence sample, there is also no visible defect in TEM as shown in Fig. 4.1(f). However, a slight Si-Si vibration was observed in the Raman spectra of this sample as displayed in Fig. 4.6, suggesting the existence of Si interstitials. As the fluence increases to 1×10^{17} cm^{-2} (highest fluence), the estimated swelling at the center of the A-layer is about 3.2%, which is similar to the maximum swelling of the A-layer in Fig. 4.3(a). In addition, both critical doses of these two samples between A and B_1 layer are about 1.5 dpa. In the weak-beam dark-field TEM image (Fig. 4.1(d)), a few small defect

clusters seemly be observed in this A-layer, suggesting that excess point defects may begin to form visible clusters in the A-layer at this irradiation dose. This swelling value, therefore, may correspond to the maximum volume swelling induced by point defects or tiny clusters.

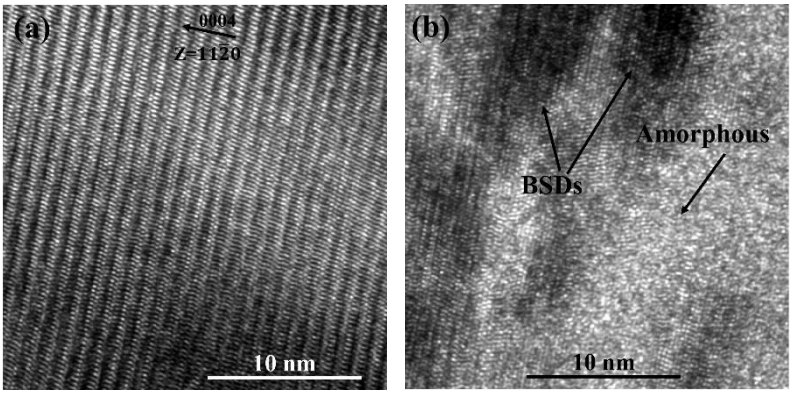

Fig. 4.4. High-resolution TEM images at different regions in the sample with medium fluence. (a) A-layer region. (b) Interface between B_1- and C-layer regions. The images were taken near the $[11\bar{2}0]$ zone axis [21].

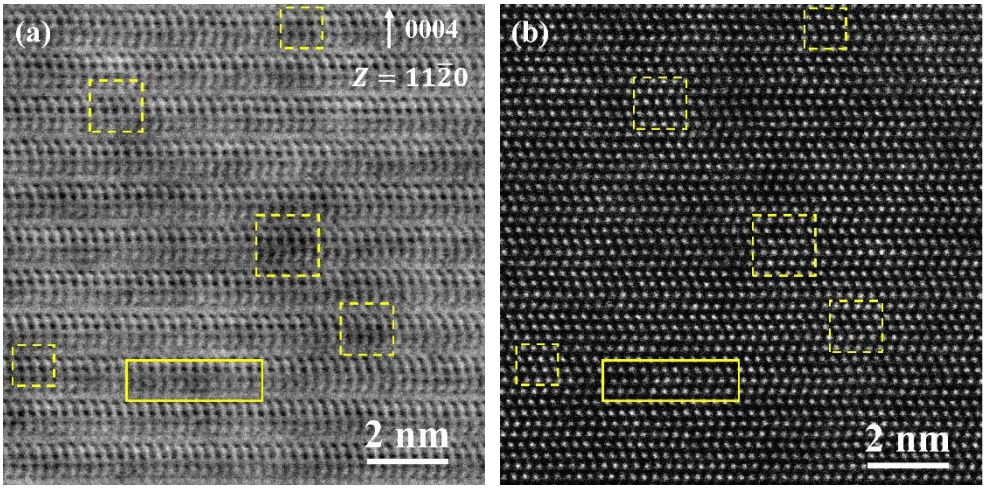

Fig. 4.5. STEM image of in A layer along $[11\bar{2}0]$ zone axis. (a, b) are taken from same region with (a) ABF image and (b) HAADF image. The contrast changed areas are marked by dash line and solid line.

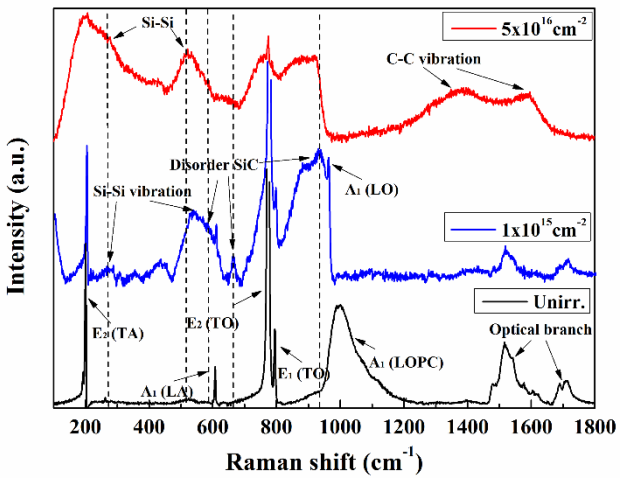

Fig. 4.6. Raman spectra of the He^+ ion-irradiated 4H-SiC with varying fluence [21].

The fluence of 1×10^{15} cm^{-2} is quite lower than the other two fluences. However, the swelling in the near-surface (i.e., A- and B_1-layers) of the lowest-fluence sample is almost the same as that of the near-surface (i.e., A-layer) of samples irradiated with the other two fluences, which is around 2-3%. Further, no obvious defects are observed in the A- and B_1-layers of this low-fluence sample in the bright-field TEM images (Fig. 4.1(e) and (f)). The appearance of Si-Si vibration in the Raman spectrum of this sample confirms the presence of Si interstitials as shown in Fig. 4.6. Therefore, the similar swelling in these near-surface regions suggest a saturation of swelling, which is ascribed to the point defects or tiny clusters in this region. Furthermore, as shown in Fig. 4.3(c) this saturation of swelling has already reached at the beginning of irradiation with a dose ~ 0.02 dpa. Moreover, due to the expansion of the BSDs and/or amorphous layer, the width of this saturation swelling region gradually reduces with increasing irradiation fluence.

4.4.2 Swelling in the BSD-containing region

As shown in Fig. 4.1(b) and (d), the BSDs are formed in the B_1-layer. For the samples irradiated with mid- and highest fluence, the average BSD size is 5.8 and 7.7 nm, respectively, with a number density of 2.6×10^{22} and 3.7×10^{22} m^{-3}, respectively. These average size and number density were counted at g=0004 two-beam TEM observation condition as described in chapter 3. In the center of the B_1-layer, the swelling is 4.9% and 5.7% for the sample with medium and highest fluence, respectively. The slight increase of swelling in the latter sample may be ascribed to its relatively larger BSD size and number density. Besides, the swelling of the B_1-layer in both of these samples range from about 3%–7% with a dose range of about 1.5-3.4 dpa (Fig. 4.3(a) and (b)). Using Ni^{3+} irradiation at 333 K, Katoh et al [10] also reported a maximum swelling of ~ 7% in 3C-SiC prior to amorphization, which agrees well with our results. However, their research was failed to detect the microstructure or defect state in that swelling condition. Therefore, it seems that a region containing BSDs would cause a volume swelling of 3%–7% in 4H-SiC at room temperature.

For the sample with medium fluence, the average BSD size in the B_2-layer is about 4.3 nm, smaller than that of the B_1-layer (i.e., 5.8 nm) in this sample. However, the estimated swelling value in the center part of the B_2-layer is higher than that of the B_1-layer, with a value of 6.7% (Fig. 4.3(a)). Using TEM, in the bottom amorphous region and the B_2-layer (Fig. 4.7(a)), helium bubbles are observed, which is consistent with the He^+ ion distribution profile as shown in Fig. 4.1(a). Therefore, the formation of helium bubbles increases the volume swelling of this BSD-containing region.

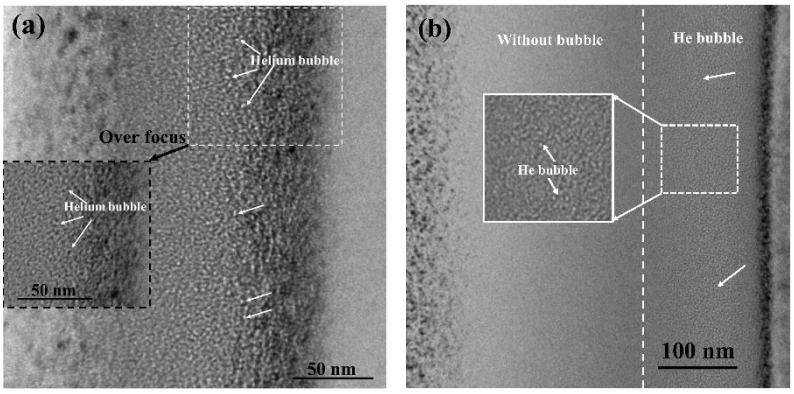

Fig. 4.7. TEM images He bubbles in the He^+ ion-irradiated samples with medium fluence (a) and high fluence (b) [21].

In addition, the B_2-layer in the sample with highest fluence showed a swelling value of ~ 3.0% (Fig. 4.3(b)), which is quite smaller than that of other BSD-containing regions discussed above. As shown in Fig. 4.1(d), the B_2-layer is very narrow (~20 nm in width) and only a few small BSDs are observed in this region (Fig. 4.1(d)). The defect condition of the B_2-layer is similar to the A-layer of this sample, which agrees well with their similar swelling value. The swelling of the B_2-layer in this sample confirms the transition swelling value for the point defect layer and BSD layer.

4.4.3 Swelling via amorphous transition

The irradiation-induced amorphous transition of 4H-SiC leads to a volume swelling of ~ 13.3% in the sample with medium fluence (Fig. 4.3(a)), which is in good agreement with the value of 12.6% reported previously in the Ni^{3+} ion-irradiated 3C-SiC [10]. Some investigations have also reported a scattered swelling of 8%–15% for the amorphous transition in SiC [10, 11, 23], which may be attributed to the different amount of Si-Si and C-C bonds depending on the irradiation temperature [23]. As shown in Fig. 4.7(a),

helium bubbles also formed in this amorphous area, which may also affect the swelling. It is hard to determine whether this swelling is only caused by the amorphous transition or it contains a contribution from helium bubbles. However, at the top part of amorphous region in the sample irradiated with high fluence, where no visible helium bubbles were observed (Fig. 4.7(b)), the volume swelling is about 12.9% (Fig. 4.3(b)). This is almost the same as the swelling value of the amorphous transition discussed above, suggesting that the amorphous transition would lead to a volume swelling of about 13% in 4H-SiC at room temperature. Because of the added formation of helium bubbles in the bottom amorphous layer (Fig. 4.6(b)), the swelling of this region increases from 13% to 15.3%. Therefore, it is found that helium bubbles could enlarge the volume swelling, even for amorphous SiC.

4.4.4 Relaxation of volume swelling at the maximum damage region

Different from the two samples irradiated with higher fluences, the volume swelling at the maximum damage region (i.e., C-layer) of the sample irradiated with the lowest fluence is less than that of the A- and B_1-layers of this sample. The swelling decreases to ~0.9% at this region while the dose increases to 0.80 dpa (Fig. 4.3(c)). The Fig. 4.1(e) shows a high TEM contrast at this region, suggesting a microstructure variation at this area. It is generally considered that only vacancies or carbon anti-site defects (C_{Si}), wherein C atoms occupy Si-vacancy sites, could result in a shrinkage of the crystal lattice [1, 24]. Under ion irradiation, interstitials and vacancies are simultaneously introduced. Some studies have reported that only interstitials, and even restricted further to only carbon interstitials, are assumed to be

mobile at temperatures below 100 °C [8, 10, 24]. Barradas et al. even found that excess carbon atoms were expelled from both sides of the buried oxide layer in oxygen ion-irradiated SiC at 600 °C [25]. However, considering the mobility of Si and C interstitials in SiC, long-range diffusion of Si or C atoms at room temperature is difficult [25]. Therefore, the redistribution of excess Si or C interstitials should not be the dominant reason for the decreased volume swelling at the region of maximum damage.

Using SETM-EELS, the anti-site defects in SiC was explored as shown in in Fig. 4.8. There is no obvious evidence of the presence C_{Si} defects (1s→ π*) in Fig. 4.8(b). Using the Raman spectroscopy, both the Si–Si and C–C vibrations was observed in the medium-fluence sample (Fig. 4.6), indicating the presence of Si and C interstitials and anti-site defects. However, in the sample with lowest fluence, a weak Si–Si vibration was observed. The C_{Si} defects, indicated by the presence of C–C vibrations, was not detected. This lack of C_{Si} defects might originate from the greater ability of C to recover than that of Si, because of the relatively higher mobility of C [10, 26, 27]. Hence, the contribution of C_{Si} also may be not the dominant reason for the decreased volume swelling at the region of maximum damage.

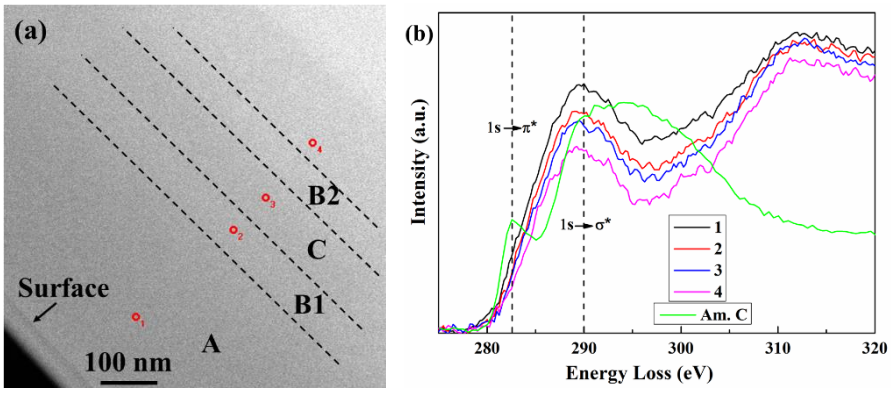

Fig. 4.8 The irradiation-induced change of EELS core-loss spectra. (a) STEM image for

the detected position (b) carbon K-edge spectra. The inset number correspond to the layers marked in (a). The reference spectra of amorphous carbon acquired from Gatan EELS website (https://eels.info/atlas/carbon).

The decreased volume swelling may be correlated with the ionization-induced annealing of He^+ ion irradiation. It has been reported that using relative high-energy (MeV) C^+, O^+, Si^+ or Ni^+ ion irradiation at room temperature, the ionization-induced annealing could recover the pre-existing defects in 4H-SiC [28]. Moreover, it is also reported that the ionization-induced annealing could relax the strain [5]. Considering the increasing effect of helium bubble upon the swelling in the two samples with higher He^+ ion fluences, it is likely that the He^+ ion irradiation might also be used to decrease the volume swelling of SiC at room temperature. However, the mechanism for the reduction effect of He^+ ion irradiation on volume swelling still requires further investigation.

4.5 Summary

Using TEM techniques, the defects formed in He+ ion irradiated 4H-SiC varied as a function of depth due to the different irradiation does in depth. Various defects were introduced in 4H-SiC over the fluence of 1×10^{15} to 1×10^{17} cm^{-2} at room temperature, including point defects or tiny clusters, BSDs, amorphous transition and helium atoms, and their contribution to the swelling was separately analyzed using STEM-EELS, which provides the volume swelling range for the different defect regions.

A saturation of the volume swelling induced by point defects and/or tiny clusters was about 2-3% at room temperature, and this saturation has already reached at about 0.02 dpa. The swelling of region containing BSDs ranges from about 3%–7% at room temperature, and amorphous transition would result in a swelling as high as 13%. Helium bubble formed at relatively high irradiation fluences would increase the volume swelling. However, decreasing effect of He^+ ion irradiation on volume swelling also seems to be possible as below a certain irradiation fluence, which requires further investigation.

Chapter 5 Conclusions and Future Work

5.1 Conclusions

Irradiation-induced strain or swelling in SiC great degrades its mechanical properties and changes electronic properties. Hence, non-destructive evaluation of the strain in SiC is important for the application of advanced micro/nano SiC-based devices. Besides, the strain or swelling is driven by irradiation-induced various defects. In this study, various microscopy techniques were used to explore strain/swelling distribution and the irradiation-induced defects in the He^+ ion irradiated 4H-SiC.

A detailed normal strain distribution in the ion-irradiated 4H-SiC was first provided using the non-destructive techniques of electron backscattering diffraction (EBSD) and confocal Raman microscopy (CRM), whose results showed good agreement. In the selected-area He^+ ion-irradiated 4H-SiC, strain is shown to not only be introduced into the irradiated area, but also to extend into the unirradiated substrate with a higher compressive strain concentrated around the interface between the irradiated and unirradiated areas owing to irradiation-induced swelling. Besides, an anisotropic strain distribution in selected-area He+ ion irradiated 4H-SiC were detected by EBSD, which indicate a correlation of strain degree and crystallographic orientation. Furthermore, this result validated the application of EBSD and CRM to evaluate the detailed strain distribution in selected-area ion-implanted SiC, which would help to measure the strain in advanced SiC-based devices and accelerate the development of SiC application.

Using various TEM techniques, the defects distribution in 4H-SiC with irradiation-induced anisotropic swelling was explored. An anisotropy of

defects distribution was found that interstitials type defects preferentially redistribute into the free expanding direction ([0004] direction) with more negative volume defects locating in the constraint swelling direction ($[10\bar{1}0]$ and $[11\bar{2}0]$ direction), which might account for the anisotropic strain or swelling. This anisotropy of defect distribution should be mainly attributed to the compressive stress introduced in the lateral direction ($[10\bar{1}0]$ and $[11\bar{2}0]$) due to the constraint against lateral expansion, which inhibits the interstitials types defects formation. This result provides an insight of the relation among defect distribution, strain and stress in the selected-area ion implanted SiC, which would be helpful to adjust the irradiation-induced strain accumulation in SiC by controlling the stress.

Irradiation-induced swelling in SiC changes with the irradiation fluence or irradiation temperature, which should be attributed to the varied defects induced during irradiation. Using TEM and STEM-EELS techniques, the dependence of the swelling on various defects in the He+ ion irradiated 4H-SiC at room temperature was separately analyzed. This result provides the volume swelling range for the different defect regions. A saturation of the volume swelling induced by point defects and/or tiny clusters was about 2-3% at room temperature, and this saturation has already reached at about 0.02 dpa. The swelling of region containing BSDs ranges from about 3%–7% at room temperature, and amorphous transition could lead to a swelling as high as 13%. Helium bubbles increases the volume swelling at relatively high irradiation fluences. However, decreasing effect of He^+ ion irradiation on volume swelling may also be possible as below a certain irradiation

fluence. This result is important to predict the swelling or strain of SiC in actual application. Besides, it would also be useful to design the implantation fluence for doping the carrier into SiC in view of the irradiation-induced strain/swelling.

5.2 Future work

As a semiconductor, carrier density uniformity in SiC is important for its performance. In chapter 2, we observed that the A_1 (LO) peak position and intensity varied with the strain estimated by CRM and EBSD in this region. This suggests that the appearance and variation of the A_1(LO) mode might be ascribed to the effect that strain and defects have on the carrier density, which need be further studied by TEM equipped with an EELS.

In Chapter 4, a decreasing effect of He^+ ion irradiation on the volume swelling was detected at a relative low irradiation fluence, which may be associated with the ionization-induced annealing of He+ ion irradiation. But, the mechanism for the reduction effect of He^+ ion irradiation on volume swelling is still not clear. In previous reported results, ionization-induced annealing is usually reported for the relatively heavy ion irradiation (such as Ge+, Ni+, and some studies also reported the irradiation of O+) with a energy of at least number MeV, however, ionization-induced annealing of a relatively lighter ion (such as H, He) with a low energy (keV) has not been reported up to now. The mechanism for the reduction effect of He^+ ion irradiation on volume swelling still requires further investigation.

Acknowledgement

Embarking on a Ph.D program is an exciting personal journey that I would like to thank everyone who has supported me.

My deepest gratitude goes first and foremost to my Ph.D supervisor Prof. Tamaki SHIBAYAMA. Without his constant instruction and guidance, this work would have taken far longer, been less scientifically sound and been much less enjoyable. I would also like to express my gratitude to assistant professor Yuki NAKAGAWA, who gave constant support and advices on my experiments. I am very grateful to my co-superior Prof. Seiichi WATANABE and Masato OHNUMA. Thanks for their help and instruction for my experiment proceeding and results analyzing. I am also very grateful to all of committee members of my doctor degree evaluation, i.e. Professor Takashi KAMIYAMA, Professor Satoshi TOMIOKA, Professor Koichi SASAKI, Professor Kiyotaka ASAKURA, Professor Yuji YAMAUCHI, Professor Tamotsu KOZAKI, Professor Kazuhiro SAWA, Professor Takashi NAKAMURA and Professor Hiroshi NAKASHIMA. Thanks for their help in my doctor degree evaluation.

I would like to say thank you to the rest of our research group: Miss Sakiko TOKUNAGA and Miss Minako KONDO. Thanks for your help in my experiments. I am also grateful to Mr. K. Ohkubo, Mr. T. Tanioka, and Mr. R. Ota for their help in experiments.

I would also like to extend my gratitude to my tutor in China, Zhanbing YANG, associated professor at USTB, who always encourages me as I meet frustration. I am also grateful to Dr. Ruixuan YU and Dr. Xuan MENG. for their help in livelihood and experiment. I would like to thank Chinese Scholarship Council's stipend support to carry out this work in Hokkaido University.

Finally, I owe my sincere gratitude to my family. Thanks to my dad and mum for backing me up all the way.

References

Chapter 1

[1] X. She, A. Q. Huang, O. Lucıa, B. Ozpineci, IEEE Trans. indus. elec. 64 (2017) 8139.

[2] N. G. Wright, A. B. Horsfall, K. Vassilevski, Mater. Today 11 (2008) 16.

[3] C. Blanc, D. Tournier, P. Godignon, D. J. Bring, V. Souliere, J. Camassel, Mater. Sci. Forum 527-529 (2006) 1051.

[4] K. Ushida et al., Proceedings of the IEEE 27th International Symp, Proceedings of the IEEE 27th International Symp. Power Semicond. Devices&IC's, Hong-Kong, (2015) 85.

[5] B.W. Brook, Conservation Biology 1 (2014) 1–11.

[6] S.J. Zinkle, J.T. Busby, Mater. Today 12 (2009) 12–19.

[7] F.C. P. Yvon, J. Nucl. Mater. 385 (2009) 217–222.

[8] L. L. Snead, T. Nozawa, M. Ferraris, Y. Katoh, R. Shinavski, M. Sawan, J. Nucl. Mater. 417 (2011) 330–339.

[9] L. L. Snead, T. Nozawa, Y. Katoh, T. Byun, S. Kondo, D. A. Petti, J. Nucl. Mater. 371 (2007) 329.

[10] K. Yueh, K. A. Terrani, J. Nucl. Mater. 448 (2014) 380.

[11] R. Cheung, Introduction to Silicon Carbide Microelectromechanical Systems, UK: Imperi. London, 2006.

[12] F. Bechstedt, P. Kachell, A. Zywietz, K. Karch, B. Adolph, K. Tenelsen, J. Furthm, Phys. Stat. Sol. 202 (1997) 35.

[13] M. Iwami, Nucl. Instr. Meth. Phys. Res. A 466 (2001) 406.

[14] P. Krishna, R.C. Marshall, C.E. Ryan, J. Cryst. Growth 8 (1971) 129.

[15] T. Liu, Z. Xu, M. Rommel, H. Wang, Y. Song, Y. Wang, crystals 9 (2019) 428.

[16] R. J. Trew, Phys. Stat. Sol. (a) 162 (1997) 409.

[17] M. H. Tadashi Maruyama, J. Nucl. Mater. 329 (2004) 1022.

[18] J. Li, L. Porter, S. Yip, J. Nucl. Mater. 255 (1998) 139.

[19] A. K. Collins, M. A. Pickering, R. L. Taylor, J. Appl. Phys. 68 (1990) 6510.

[20] L.S. Sigl, J. Europ. Ceram. Soc. 23 (2003) 1115.

[21] Z. Li, R. C. Bradt, J. Amer. Ceram. Soc. 69 (1986) 863.

[22] R.G. Munro, J. Phys. Chem. Ref. Data 26 (1997) 1195.

[23] Koichi Niihara, Journal of the Less Common Metals 65 (1979) 155.

[24] B. V. Cockeram, J. Amer. Ceram. Soc. 85 (2002) 603.

[25] M. C. Osborne, J. C. Hay, L. L. Snead, J. Amer. Ceram. Soc. 82 (1999) 2490.

[26] G. D. Quinn, J. A. Salem, J. Amer. Ceram. Soc. 85 (2002) 873.

[27] A. G. Evans, E. A. Charles, J. Amer. Ceram. Soc. (1976) 371.

[28] X. Xie, X. Hu, X. Chen, F. Liu, X. Yang, X. Xu, H. Wang, J. Li, P. Yubd, R. Wang, CrystEngComm 19 (2017) 6527.

[29] J. A. Brinkman, Am. J. Phys. 24 (1956) 246.

[30] D. Huang, F. Gao, D. A. Cardimona, C. P. Morath, V. M. Cowan, Proc. of SPIE 96160S-1 (2015).

[31] Y. Katoh, N. Hashimoto, S. Kondo, L.L. Snead, J. Nucl. Mater. 351 (2006) 228.

[32] C. Liu, L. He, Y. Zhai, B. Tyburska-Püschel, P. M. Voyles, K. Sridharan, D. Morgan, I. Szlufarska, Acta Mater. 125 (2017) 377.

[33] D. J. Senor, G. E. Youngblood, L. R. Greenwood, D. V. Archer, D. L. Alexander, M. C. Chen, G. A. Newsome, J. Nucl. Mater. 317 (2003) 145.

[34] S. Kondo, K. H. Park, Y. Katoh, A. Kohyama, Fus. Sci. Technol. 44 (2003) 181.

[35] Y. Katoh, L.L. Snead, C.H. Henager Jr., A. Hasegawa, A. Kohyama, B. Riccardi, H.

Hegeman, J. Nucl. Mater. 367 (2007) 659.

[36] A. Kawasuso, H. Itoh, N. Morishita, M. Yoshikawa, T. Ohshima, I. Nashiyama, S. Okada, H. Okumura, S. Yoshida, Appl. Phys. A 67 (1998) 209.

[37] M. Ishimaru, I. Bae, A. Hirata, Y. Hirotsu, J. A. Valdez, K. E. Sickafus, Phys. Rev. B 72 (2005) 24116.

[38] M. Ishimaru, I. Bae, Y. Hirotsu, S. Matsumura, K. E. Sickafus, Phys. Rev. Let. 89 (2002) 55502.

[39] L.W. W.J. Weber, , Nucl. instr. Meth. Phys. Res. B 106 (1995) 298.

[40] L.L. Snead, Nucl. instr. Meth. Phys. Res. B 191 (2002) 497.

[41] L. L. Snead, Y. Katoh, T. Koyanagi, K. Terrani, E. D. Specht, J. Nucl. Mater. 471 (2016) 92.

[42] S. Leclerc, A. Declémy, M. F. Beaufort, C. Tromas, J. Appl. Phys. 98 (2005).

[43] B. Tyburska-Püschel, Y. Zhai, L. He, C. Liu, A. Boulle, P. M. Voyles, I. Szlufarska, K. Sridharan, J. Nucl. Mater. 476 (2016) 132.

[44] T. Yano, H. Miyazaki, M. Akiyoshi, T. Iseki, J. Nucl. Mater. 253 (1998) 78.

[45] F. X. Zhang, Y. Tong, Haizhou Xue, J. K. Keum, Yanwen Zhang, A. Boulle, A. Debelle, Appl. Phys. Let. 114 (2019) 221904.

[46] X. Chen, W. Zhou, Q. Feng, J. Zheng, X. Liu, B. Tang, J. Li, J. Xue, S. Peng, J. Nucl. Mater. 478 (2016) 215.

[47] N. Daghbouj, B. S. Li, M. Callisti, H. S. Sen, M. Karlik, T. Polcar, Acta Mater. 181 (2019) 160.

[48] Y. Yang, J. Guo, B. Raghothamachar, X. Chan, T. Kim, M. Dudley, J. Electr. Mater. 47 (2018) 938.

[49] S. A. Stepanov, see http://sergey.gmca.aps.anl.gov/gid _ sl.html.

[50] M. D. Vaudin, Y. B. Gerbig, S. J. Stranick, R. F. Cook, Appl. Phys. Let. 93 (2008) 193116.

[51] Diego Olego, M. Cardona, P. Vogl, Phys. Rev. B 25 (1982) 3878.

[52] S. Rohmfeld, M. Hundhausen, L. Ley, C.A. Zorman, M. Mehregany, J. Appl. Phys. 91 (2002) 1113.

[53] W. Osborn, L. H. Friedman, M. Vaudin, Ultramicroscopy, 184 (2018) 88.

[54] S. I. Wright, M. M. Nowell, and D. P. Field, A review of strain analysis using electron backscatter diffraction, Microsc. Microanal. 17 (2011) 316.

[55] A. J. Wilkinson, T. B. Britton, J. Jiang and P. S. Karamched, A review of advances and challenges in EBSD strain mapping, IOP Conf. Ser.: Mater. Sci. Eng 55 (2014) 12020.

[56] A. J. Wilkinson, G. Meaden, D. J. Dingley, Ultramicroscopy, 106 (2006) 307.

[57] J. Jiang, T.B. Britton, A.J. Wilkinson, Ultramicroscopy, 125 (2013) 1.

[58] E. Oliviero, C. Tromas, F. Pailloux, A. Declemy, M.F. Beaufort, C. Blanchard, J.F. Barbot, Mater. Sci. Eng. B 102 (2003) 289.

[59] I. Bae, W. J. Weber, Y. Zhang, J. Appl. Phys. 106 (2009) 1235525.

[60] Bing Yang, Hao Zhuang, Junhao Li, Nan Huang, Lusheng Liu, Kaiping Tai, Xin Jiang, CrystEngComm 18 (2016) 6817.

[61] Y. A. Zeng , M. H. White, M. K. Das, Solid-state electronics 49 (2005) 1017.

[62] W. Jiang, P. Nachimuthu, W. J. Weber, L. Ginzbursky, Appl. Phys. Let. 91 (2007) 91918.

Chapter 2

[1] X. She, A. Q. Huang, O. Lucıa, B. Ozpineci, IEEE Trans. Industr. Electron. 64 (2017) 8193.

[2] N. G. Wright, A. B. Horsfall, K. Vassilevski, Mater. Today 11 (2008) 16.

[3] S. Castelletto, B. C. Johnson, V. Ivády, N.Stavrias, T. Umeda, A. Gali, T. Ohshima, Nature Mater. 13 (2014) 151.

[4] X. Chen, W. Zhou, Q. Feng, J. Zheng, X. Liu, B. Tang, J. Li, J. Xue, S. Peng, J. Nucl. Mater. 478 (2016) 215.

[5] S. Sasaki, J. Suda, T. Kimoto, J. Appl. Phys. 111 (2012) 103715.

[6] A. Ashraf Ali, J. Kumar, V. Ramakrishnan, K. Asokan, Mater. Lett. 213 (2018) 208.

[7] A. Qamar, D. V. Dao, P. Tanner, H. Phan, T. Dinh, S. Dimitrijev, Appl. Phys. Expr. 8 (2015) 061302.

[8] K. Lee, Isnaeni, Y. Yoo, J. Lee, Y. Kim, Y. Cho, J. Appl. Phys. 113 (2013) 173512.

[9] S. Tsukimoto, T. Ise, G. Maruyama, S. Hashimoto, T. Sakurada, J. Senzaki, T. Kato, K. Kojima, H. Okumura, J. electron. Mater. 47 (2018) 6722.

[10] X. Xie, X. Hu, X. Chen, F. Liu, X. Yang, X. Xu, H. Wang, J. Li, P. Yu, R. Wang, CrystEngComm, 19 (2017) 6527.

[11] Y. Yang, J. Guo, B. Raghothamachar, X. Chan, T. Kim, M. Dudley, J. Electronic Mater. 47 (2018) 938.

[12] A. Debelle, L. Thome, D. Dompoint, A. Boulle, F. Garrido, J. Jagielski, D. Chaussende, J. Phys. D: Appl. Phys. 43 (2010) 455408.

[13] S. Leclerc, A. Declémy, M. F. Beaufort, C. Tromas, J. F. Barbot, J. Appl. Phys. 98 (2005) 113506.

[14] D.J. Sprouster, T. Koyanagib, E. Dooryheec, S. K. Ghose c, Y. Katohb, L. E. Ecke, Scr. Mater. 143 (2018) 176.

[15] X. Li, Z. Lia, X. F. Tao, L. L. Ren, S. T. Gao, G. F. Xu, Mater. Lett. 132 (2014) 285.

[16] S. I. Wright, M. M. Nowell, and D. P. Field. Microsc. Microanal. 17 (2011) 316.

[17] A. J. Wilkinson, T. B. Britton, J. Jiang and P. S. Karamched, IOP Conf. Ser.: Mater.

Sci. Eng. 55 (2014) 012020.

[18] W. Osborn, L. H. Friedman, M. Vaudin, Ultramicroscopy 184 (2018) 88.

[19] M. D. Vaudin, Y. B. Gerbig, S. J. Stranick, R. F. Cook, Appl. Phys. Lett. 93 (2008) 193116.

[20] S. Nakashima, H. Harima, Phys. stat. sol. (a) 162 (1997) 39.

[21] **S. Yang**, S. Tokunaga, M. Kondo, Y. Nakagawa, T. Shibayama, Appl. Surf. Sci. 500 (2020).

[22] S. Sorieul, J. M. Costantini, L. Gosmain, L. Thome, J. J. Grob, J. Phys.: Condens. Matter. 18 (2006) 5235.

[23] T. Koyanagi, M. J. Lance, Y. Katoh, Scr. Mater. 125 (2016) 58.

[24] S. Nakashima, T. Mitani, J. Senzaki, H. Okumura, T. Yamamoto, J. Appl. Phys. 97 (2005) 123507.

[25] S. Nakashima, T. Kato, S. Nishizawa, T. Mitani, H. Okumura, T. YamamotobJ. Electrochem. Soc. 153 (2006) 319.

[26] S. Rohmfeld, M. Hundhausen, L. Ley, C.A. Zorman, M. Mehregany, J. Appl. Phys. 91 (2002) 1113.

[27] Y. Zhang, F. Gao, W. Jiang, D. E. McCready, and W. J. Weber, Phys. Rev. B 70(2004), 125203.

[28] G. H. Loechelt, N. G. Cave, J. Menendez, J. Appl. Phys. 86 (1999) 6164.

Chapter 3

[1] S. Kondo, T. Hinoki, M. Nonaka, K. Ozawa, Acta Mater. 83 (2019) 1-9.

[2] L. L. Snead, T. Nozawa, Y. Katoh, T. S. Byun, S. Kondo, D. A. Petti, J. Nucl. Materl. 371 (2007) 329.

[3] X. She, A. Q. Huang, O. Lucıa, B. Ozpineci, IEEE Trans. Industr. Electron 64 (2017)

8193.

[4] S. Castelletto, B. C. Johnson, V. Ivády, N. Stavrias, T. Umeda, A. Gali, Nature Mater. 13 (2014) 151.

[5] N. G. Wright, A. B. Horsfall, K. Vassilevski, Mater. Today 11 (2008) 16.

[6] M. Li, X. Zhou, H. Yang, S. Du, Q. Huang, Scr. Mater. 143 (2018) 149.

[7] C. Liu, L. He, Y. Zhai, P. M. Voyles, K. Sridharan, D. Morgan, I. Szlufarska, Acta Mater. 125 (2019) 377.

[8] Y. Katoh, N. Hashimoto, S. Kondo, L. L. Snead, A. Kohyama, J. Nucl. Materl. 351 (2006) 228.

[9] F.W. Clinard, Jr., W. Dienst, E.H. Farnum, J. Nucl. Materl. 212-215 (1984) 1075.

[10] I.T. Yano T J. Nucl. Materl. 203 (1993) 249.

[11] T. Yano, M. Akiyoshi, K. Ichikawa, Y. Tachi, T. Iseki, J. Nucl. Materl. 289 (2001) 102.

[12] C. A. C. Silva, C. Shih, T. Koyanagi, Y. Katoh, S. J. Zinkle, Scr. Mater. 114 (2016) 74.

[13] J.C. Nappé, C. Maurice, Ph. Grosseau, F. Audubert, L. Thomé, B. Guilhot, M. Beauvy, M. Benabdesselam, J. European Ceram. Soc. 31 (2011) 1503.

[14] W. Jiang, P. Nachimuthu, W. J. Weber, L. Ginzbursky, Appl. Phys. Lett. 91 (2007).

[15] L. L. Snead, Y. Katoh, T. Koyanagi, K. Terrani, E. D. Specht, J. Nucl. Materl. 471 (2016) 92.

[16] J. Costantini, X. Kerbiriou, M. Sauzay, J. Phys. D: Appl. Phys. 45 (2012) 465301.

[17] Y. Lin, C. Ho, W. Chuang, C. Ku, J. Kai, J. Nucl. Materl. 455 (2014) 292.

[18] B. Tyburska-Püschel, Y. Zhai, L. He, C. Liu, A. Boulle, P. M. Voyles, I. Szlufarska, J. Nucl. Materl. 476 (2016) 132.

[19] S. Kondo, Chad M. Parish, T. Koyanagi, Y. Katoh, Appl. Phys. Lett. 110 (2017) 142106.

[20] S. Yang, S. Tokunaga, M. Kondo, Y. Nakagawa, T. Shibayama, Appl. Surf. Sci. 500 (2020).

[21] R. Devanathan, T. D. Rubia, W.J. Weber, J. Nucl. Materl. 253 (1998) 47.

[22] Y. Zhang, W. J. Weber, W. Jiang, C. M. Wang, V. Shutthanandan, A. Hallen, J. Appl. Phys. 95 (2004) 4012.

[23] D. B. Williams, C. B. Carter, Transmission electron microscopy: Diffraction, imaging, and spectrometry, New York, 1996.

[24] S. Sandlobes, M. Friak, S. Zaefferer, A. Dick, S. Yic, D. Letzig, Z. Pei, L. F. Zhu, J. Neugebauer, D. Raabe, Acta Mater. 60 (2012) 3011.

[25] H. Zhang, Zhongwen Yao, G. Morin, M. Griffiths, J. Nucl. Materl. 451 (2014) 88.

[26] S. Sandlöbes, M. Friák, J. Neugebauer, D. Raabe, Mater. Sci. Eng. A 576 (2013) 61.

[27] Y. Lin, L. Chen, C. Hsieh, A. Hu, S. Lo, F. Chen, J. Kai, J. Nucl. Materl. 498 (2018) 71.

[28] E. Okunishi, H. Sawada, Y. Kondo, Micron 43 (2012) 538.

[29] J. Q. Liu, M. Skowronski, C. Hallin, R. Soderholm, H. Lendenmann, Appl. Phys. Lett. 80 (2002) 749.

[30] A. L. Hannam, P. T. B. Shaffer, J. AppL Cryst. 2 (1969) 45.

[31] J. Li, Z. Wang, C. Chen, S. Huang, Sci. Rep. 4:5521 (2014).

[32] K. Watanabe, E. Asano, T. Yamazaki, Y. Kikuchi, I. Hashimoto, Ultramicroscopy 102 (2004) 13.

[33] S. J. Pennycook, D. E. Jesson, Ultramicroscopy 37 (1991) 14.

[34] M. Bockstedte, A. Mattausch, O. Pankratov, Phys. Rev. B 70 (2004) 115203.

[35] F. Gao, W. J. Weber, J. Appl. Phys. 94 (2003) 4348.

[36] E. Oliviero, M. F. Beaufort, J. F. Barbot, A. van Veen, A. V. Fedorov, J. Appl. Phys. 93 (2003) 231.

[37] P. G. Baranov, I. V. Ilyin, A. A. Soltamova, E. N. Mokhov, Phys. Rev. B 77 (2008) 85120.

[38] S. Kondo, A. Kohyama, T. Hinoki, J. Nucl. Materl. 367-370 (2007) 764.

[39] Y. Katoh, S. Kondo, L. L. Snead, J. Nucl. Materl. 382 (2008) 170.

Chapter 4

[1] S. Kondo, T. Hinoki, M. Nonaka, K. Ozawa, Acta Mater. 83, 1–9 (2015).

[2] A. Iveković, S. Novak, G. Dražić, D. Blagoeva, S.G. Vicente, J. Eur. Ceram. Soc. 33, 1577–1589, (2013).

[3] M. Li, X. Zhou, H. Yang, S. Du, Q. Huang, Scr. Mater. 143, 149–153 (2018).

[4] S. Castelletto, B. C. Johnson, V. Ivády, N. Stavrias, T. Umeda, A. Gali, T. Ohshima, Nature Mater. 13, 151–156 (2014).

[5] F. X. Zhang, Y. Tong, Haizhou Xue, J. K. Keum, Yanwen Zhang, A. Boulle, A. Debelle, W. J. Weber, Appl. Phys. Lett. 114, (2019).

[6] S. Yang, S. Tokunaga, M. Kondo, Y. Nakagawa, T. Shibayama, Appl. Surf. Sci. 500, (2020).

[7] Y. Katoh, S. Kondo, L. L. Snead, J. Nucl. Mater. 382, 170–175 (2008).

[8] L. L. Snead, Y. Katoh, T. Koyanagi, K. Terrani, E. D. Specht, J. Nucl. Mater. 471, 92–96 (2016).

[9] T. Sawabe, M. Akiyoshi, K. Ichikawa, K. Yoshida, T. Yano, J. Nucl. Mater. 386-388, 333–337 (2009).

[10] Y. Katoh, H. Kishimoto, A. Kohyama, J. Nucl. Mater. 307-311, 1221–1226 (2002).

[11] S. Leclerc, A. Declémy, M. F. Beaufort, C. Tromas, J. F. Barbot, J. Appl. Phys. 98, (2005).

[12] Y. Katoh, L.L. Snead, I. Szlufarska, W.J. Weber, Curr. Opin. Solid State Mater. Sci., 16,143-152 (2012).

[13] S. Leclerc, M. F. Beaufort, A. Declémy, J. F. Barbot, Appl. Phys. Lett. 93, (2008).

[14] In-Tae Bae, W. J. Weber, Y. Zhang, J. Appl. Phys. 106, 123525, 2009.

[15] A. Heft, E. Wendler, T. Bachmann, E. Glaser, W. Wesch, Mater Sci Eng B, 29, 142 (1995).

[16] W.J. Weber, L. WangM. Nucl. Instrum. Methods in Phys. Res. B, 106, 298 (1995).

[17] D. B. Williams, C. B. Carter, Transmission electron microscopy (Plenum, New York, 1996), p657.

[18] W. Jiang, C. M. Wang, W. J. Weber, M. H. Engelhard, L. V. Saraf, J. Appl. Phys. 95, 4687–4690 (2004).

[19] C. Liu, L. He, Y. Zhai, P. M. Voyles, K. Sridharan, D. Morgan, I. Szlufarska, Acta Mater. 125, 377–389 (2017).

[20] M. Ishimaru, R. M. Dickerson, K. E. Sickafus, Appl. Phys. Lett. 75, 352–354 (1999).

[21] S. Yang, Y. Nakagawa, M. Kondo, T. Shibayama, J. Appl. Phys. 127, 175106 (2020).

[22] T. Taguchi, S. Yamamoto, H. Ohba, Acta Mater. 154, 90–99 (2018).

[23] M. Ishimaru, In-Tae Bae, A. Hirata, Y. Hirotsu, J. A. Valdez, K. E. Sickafus, Phys. Rev. B 72, (2005).

[24] W. Jiang, P. Nachimuthu, W. J. Weber, L. Ginzbursky, Appl. Phys. Lett. 91, (2007).

[25] N.P. Barradas, C. Jeynes, S.M. Jackson, Nucl. Instr. Meth. Phys. Res. B 136-138, 1168–1171 (1998).

[26] F. Gao, W. J. Weber, J. Appl. Phys. 94, 4348 (2003).

[27] E. Oliviero, M. F. Beaufort, J. F. Barbot, A. van Veen, A. V. Fedorov, J. Appl. Phys. 93, 231 (2003).

[28] Y. Zhang, R. Sachan, O. H. Pakarinen, M. F. Chisholm, P. Liu, H. Xue, W. J. Weber, Nat. Commun. 6, 8049 (2015).